



## Synchronization of clocks

Marcin Kapitaniak<sup>a,b</sup>, Krzysztof Czołczynski<sup>a</sup>, Przemysław Perlikowski<sup>a</sup>, Andrzej Stefanski<sup>a</sup>, Tomasz Kapitaniak<sup>a,\*</sup>

<sup>a</sup> Division of Dynamics, Technical University of Lodz, Stefanowskiego 1/15, 90-924 Lodz, Poland

<sup>b</sup> Centre for Applied Dynamics Research, School of Engineering, University of Aberdeen, AB24 3UE, Aberdeen, Scotland, United Kingdom

### ARTICLE INFO

#### Article history:

Accepted 2 March 2012

Available online 8 March 2012

editor: D.K. Campbell

#### Keywords:

Synchronization

Clocks

Discontinuous systems

### ABSTRACT

In this report we recall the famous Huygens' experiment which gave the first evidence of the synchronization phenomenon. We consider the synchronization of two clocks which are accurate (show the same time) but have pendula with different masses. It has been shown that such clocks hanging on the same beam can show the almost complete (in-phase) and almost antiphase synchronizations. By almost complete and almost antiphase synchronization we defined the periodic motion of the pendula in which the phase shift between the displacements of the pendula is respectively close (but not equal) to 0 or  $\pi$ . We give evidence that almost antiphase synchronization was the phenomenon observed by Huygens in XVII century. We support our numerical studies by considering the energy balance in the system and showing how the energy is transferred between the pendula via oscillating beam allowing the pendula's synchronization. Additionally we discuss the synchronization of a number of different pendulum clocks hanging from a horizontal beam which can roll on the parallel surface. It has been shown that after a transient, different types of synchronization between pendula can be observed; (i) the complete synchronization in which all pendula behave identically, (ii) pendula create three or five clusters of synchronized pendula. We derive the equations for the estimation of the phase differences between phase synchronized clusters. The evidence, why other configurations with a different number of clusters are not observed, is given.

© 2012 Elsevier B.V. All rights reserved.

### Contents

1.	Introduction.....	2
2.	Pendulum clocks .....	5
2.1.	Brief history of mechanical clocks .....	5
2.2.	Escapement mechanisms .....	6
2.2.1.	Verge-and-foliot escapement .....	8
2.2.2.	Anchor escapement .....	10
2.3.	Dynamics of clocks .....	11
3.	Modeling Huygens' experiment: coupling through elastic structure.....	16
3.1.	Coupling in Huygens' experiment .....	16
3.2.	Senators' five degrees of freedom model .....	16
3.3.	Model of two double spherical pendula.....	18
3.4.	Three degrees of freedom discontinuous model .....	21
3.4.1.	Energy balance of the clocks' pendula.....	23

\* Corresponding author.

E-mail address: [tomaszka@p.lodz.pl](mailto:tomaszka@p.lodz.pl) (T. Kapitaniak).

3.4.2.	Energy balance of the beam and whole system (26) and (27).....	23
3.5.	Three degrees of freedom model with van der Pol's friction.....	26
3.6.	Model with the transversal oscillations of the beam.....	27
4.	Synchronization of two pendulum clocks.....	28
4.1.	Experimental observations.....	28
4.2.	Numerical results.....	29
4.2.1.	Synchronization of two identical pendula.....	30
4.2.2.	Synchronization of two pendula with different masses.....	31
4.2.3.	Synchronization of two pendula with different lengths.....	42
4.2.4.	Chaos in the coupled clocks.....	46
4.3.	Discussion.....	48
5.	Synchronization of $n$ clocks.....	52
5.1.	Experimental synchronization of metronomes.....	52
5.2.	The model.....	54
5.3.	Numerical simulations.....	55
5.3.1.	Identical clocks.....	55
5.3.2.	Nonidentical clocks.....	59
5.4.	Discussion.....	65
6.	Conclusions.....	66
	Acknowledgments.....	67
	References.....	67

## 1. Introduction

A pendulum clock is a clock that uses a pendulum, a swinging weight as its timekeeping element. The advantage of a pendulum for timekeeping is 'that it is a resonant device; it swings back and forth in a precise time interval dependent on its length and resists swinging at other rates. From its invention in 1656 by Christiaan Huygens (1629–95) until the 1930s, the pendulum clock was the world's most precise timekeeper, accounting for its widespread use [1–3]. Pendulum clocks must be stationary to operate; any motion or accelerations will affect the motion of the pendulum, causing inaccuracies.

In the 60s of XVII century the longitude problem, i.e., finding a robust, accurate method of the longitude determination for marine navigation was the outstanding challenge. Huygens believed that pendulum clocks, suitably modified to withstand the rigors of the sea, could be sufficiently accurate to reliably determine the longitude<sup>1</sup> [4]. In a letter to the Royal Society of London of 27 February 1665 Huygens described his famous experiment which showed the tendency of two pendula (of the clocks) to synchronize, or anti-synchronize when mounted together on the same beam [5]. Originally, he used the phrase "an odd kind of sympathy" to describe the observed behavior in two maritime clocks. The original drawing showing this experiment is shown in Fig. 1. Two pendula, mounted together, will always end up swinging in exactly opposite directions, regardless of their respective individual motion. This was one of the first observations of the phenomenon of the coupled harmonic oscillators, which have many applications in physics [6–14], biology and chemistry [12,15–19]. In engineering very spectacular was synchronization of pedestrians on Millennium bridge [20,9,21–26]. Huygens originally believed the synchronization occurs due to air currents shared between two pendula, but later after performing several simple tests he dismissed this and attributed the sympathetic motion of pendula to imperceptible movement in the beam from which both pendula were suspended.

Huygens' study of two clocks operating simultaneously arose from the very practical requirement of the redundancy: if one clock stopped, had to be cleaned or wound up, then the other one provided the proper timekeeping [27,28]. Ultimately, the innovation of the pendulum did not solve the longitude problem, since slight and almost insensible motion was able to cause an alteration in their work [29–32].

Recently, this idea has been validated by a few groups of researchers who tested Huygens' idea [33–46]. These studies do not give the definite answer to the question: what Huygens was able to observe.

To explain Huygens' observations Bennett et al. [33] built an experimental device consisting of two interacting pendulum clocks hung on a heavy support which was mounted on a low-friction wheeled cart. The device moves by the action of the reaction forces generated by the swing of two pendula and the interaction of the clocks occurs due to the motion of the clocks' base. It has been shown that to repeat Huygens' results high precision (the precision that Huygens certainly could not achieve) is necessary.

Kanunnikov & Lamper [35] showed that the precise antiphase motion of different pendula noted by Huygens cannot occur. Different pendula (possibly with different masses) were definitely used by Huygens as can be seen in his drawing shown in Fig. 2.

Pogromsky et al. [34] designed a controller for synchronization problem of two pendula suspended on an elastically supported rigid beam. A controller solves the synchronization problem in such a way that the pendula reach the desired

<sup>1</sup> The discrepancy in the clock rate equal to one oscillation of the second pendulum (pendulum with a period of oscillations equal to 1 (s) in a day corresponds to the error in the longitude determination, approximately equal to 500 m in a day (at the equator).

## Nomenclature

$\alpha$  (rad/s) angular frequency of the beam–pendula system oscillations;  
 $\alpha_{i0}$  (rad/s) angular frequency of  $i$ -th pendulum oscillations when the beam is at rest;  
 $\beta_i$  (rad), (deg) phase shift between pendula;  
 $\beta_{i0}$  (rad), (deg) initial value of  $\beta_i$ ;  
 $\beta_{II} = \beta_2, \beta_{III} = 360^\circ - \beta_3, \beta_{IV} = \beta_4, \beta_V = 360^\circ - \beta_5$  (deg) phase shift between pendula;  
 $\beta_{10}, \beta_{110}, \beta_{1110}, \beta_{1110}, \beta_{1110}, \beta_{1110}$  (deg) initial values of phase shifts;  
 $\delta_i, \sigma$  perturbation added to the variables  $\varphi_i$  and  $x$ ;  
 $\gamma_N$  (rad), (deg) working angle of the escapement mechanism;  
 $\Phi_i, \Phi$  (rad) amplitudes of oscillations of the pendulum;  
 $\varphi_i, \dot{\varphi}_i, \ddot{\varphi}_i$  displacement (rad), velocity (rad/s) and acceleration (rad/s<sup>2</sup>) of the  $i$ -th pendulum;  
 $\varphi_{i0}, \dot{\varphi}_{i0}$  initial conditions of the  $i$ -th pendulum motion;  
 $\mu_i$  mass ratio  $m_i/m_1$ ;  
 $\nu$  (rad) phase shift between the beam and pendulum 1;  
 $\xi$  scale factor of the second pendulum (related to the first one);  
 $A_{11}, A_{31}$  (m/s<sup>2</sup>) amplitudes of first and third harmonical component of the beam acceleration;  
 $c_{\varphi_i}$  (N s m) damping coefficient of the  $i$ -th pendulum damper;  
 $c_x$  (N s/m) damping coefficient of the damper between the beam and the basis;  
 $F_{11}, F_{31}$  (m/s<sup>2</sup>) amplitudes of first and third harmonical component of the force between pendula and beam;  
 $g$  (m/s<sup>2</sup>) gravity;  
 $H_{13}$  (N<sup>2</sup>) square of the amplitude of the first harmonical component of the force acting on the beam with three pendula;  
 $H_{15}, H_{35}$  (N<sup>2</sup>) square of the amplitude of the first and third harmonical component of the force acting on the beam with five pendula;  
 $k_x$  (N/m) stiffness coefficient of the spring between the beam and the basis;  
 $l, l_i$  (m) length of the pendulum;  
 $M$  (kg) mass of the beam;  
 $M_{Di}$  (N m) driven moment equal to 0 or  $M_{Ni}$ , depending on  $\varphi_i$  and  $\dot{\varphi}_i$ ;  
 $M_{Ni}$  (N m) moment of force generated by escapement mechanism;  
 $m, m_i$  (kg) mass of the pendulum;  
 $N$  number of periods  $T$  of pendula oscillations ( $NT$  – unit of time);  
 $T$  (s) period of the beam–pendula system oscillations;  
 $T_{i0}$  (s) period of  $i$ -th pendulum oscillations when the beam is at rest;  
 $T_i$  (s) period of the oscillations of  $i$ -th pendulum hanging solo on the moving beam;  
 $T_m$  (s) period of long-period synchronization;  
 $t$  (s) time;  
 $U$  (kg) global mass of the system (beam plus pendula);  
 $W_{beam}^{DAMP}$  (N m) energy dissipated by the beam during one period of motion;  
 $W_i^{DAMP}$  (N m) energy dissipated by the  $i$ -th pendulum during one period of motion;  
 $W_{beam}^{DRIVE}$  (N m) energy delivered to the beam during one period of motion;  
 $W_i^{DRIVE}$  (N m) energy delivered to the  $i$ -th pendulum during one period of motion;  
 $W_i^{VDP}$  (N m) energy delivered to the  $i$ -th pendulum by van der Pol positive damping during one period of motion;  
 $W_i^{SYN}$  (N m) energy delivered from the  $i$ -th pendulum to the beam during one period of motion;  
 $X$  (m) amplitude of the beam oscillations;  
 $X_{11}, X_{31}$  (m) amplitudes of first and third harmonical component of the beam oscillations;  
 $x, \dot{x}, \ddot{x}$  displacement (m), velocity (m/s) and acceleration (m/s<sup>2</sup>) of the beam;  
 $x_0, \dot{x}_0$  initial values of displacement and velocity of the beam;

level of energy and they move synchronously in opposite directions. The original Huygens' problem has been also related to a practical application of avoiding resonance during the start up procedure of speeding two unbalanced rotors.

The system very close to the one considered by Huygens (i.e., two pendulum clocks with cases hanging from the same beam) has been investigated by *Senator* [36] who developed a qualitative approximate theory of clocks' synchronization. This theory explicitly includes the essential nonlinear elements of Huygens' system, i.e., the escapement mechanisms but also includes many simplifications.

A device mimicking Huygens' clock experiment, the so-called “coupled pendula of the Kumamoto University” [38], consists of two pendula which suspension rods are connected by a weak spring, and one of the pendula is excited by an external rotor. The numerical results of Fradkov & Andrievsky [39] show simultaneous approximate in-phase and antiphase

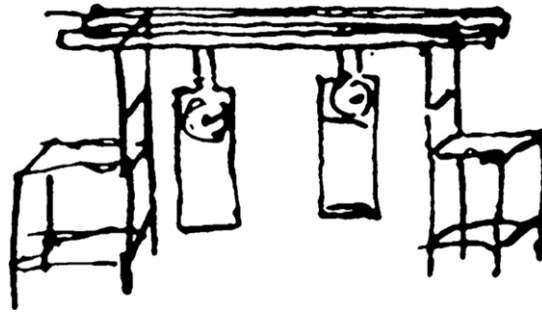


**Fig. 1.** An original drawing of Huygens illustrating his experiments with pendulum clocks.

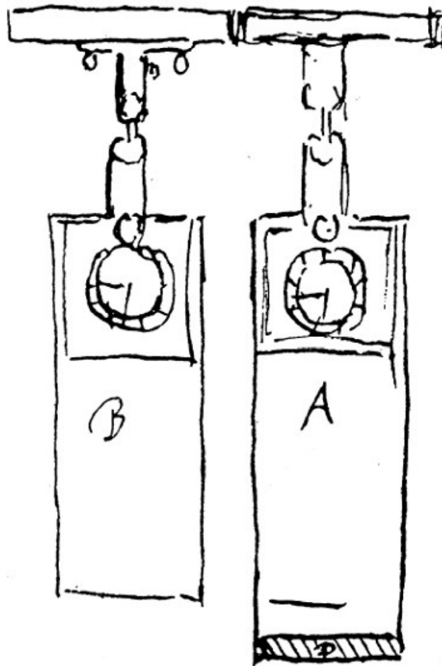


**Fig. 2.** Details of the Huygens' experiment; it is clearly visible that the clocks used in the experiment have not been identical, D denotes the weight used to stabilize the clock case.

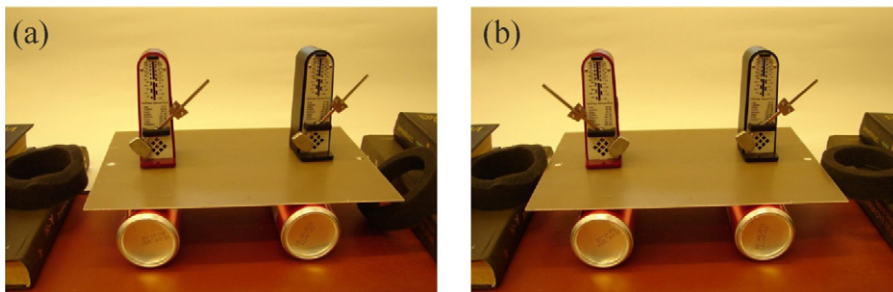


**Fig. 3.** Synchronization of two metronomes; (a) in-phase synchronization, (b) antiphase synchronization.

synchronization. Both types of synchronization can be obtained for different initial conditions. Additionally, it has been shown that for small difference in the pendula frequencies they may not synchronize.

A very simple demonstration device was built by Pantaleone [40]. It consists of two metronomes located on a freely moving light wooden base as shown in Fig. 3(a, b). The base lies on two empty soda cans which smoothly rolls on the table. Both in-phase (Fig. 3(b)) and antiphase (Fig. 3(a)) synchronization of the metronomes have been observed. The synchronization problem for larger number of metronomes has been studied in [41–43].

The problem of clocks synchronization is also studied by Blekhman [7] where the clocks have been modeled as van-der Pol's type self-excited oscillators (as in [40,41]). Blekhman also discusses Huygens' observations, and recounts the results of a laboratory reproduction of the coupled clocks as well as presenting a theoretical analysis of oscillators coupled through a common supporting frame. He predicted that both in-phase and anti-phase motions are stable under the same circumstances.

A synchronous regime in the Huygens' problem is studied by Kanunnikov & Lamper [35] with allowance for nonlinear interaction between the transversal oscillations of a beam and clock's pendula. The case where the motion of the pendula is synchronous and close to the out-of-phase motion is studied.

In this report we repeat Huygens' experiment using real pendulum clocks. We have been trying to perform this experiments in the same way as Huygens did them. We hang two clocks on the same beam and observe the behavior of the pendula. The clocks in the experiment have been selected in such a way as to be as identical as possible. It has been observed that when the beam is allowed to move horizontally the clocks can synchronize both in-phase and anti-phase. As we notice some small differences in the pendulum lengths and periods (so small to be identified in the Huygens' time) we perform computer simulations to answer the question: how the nonidentity of the clocks influences the synchronization process. We show that even the clocks with significantly different periods of oscillations can synchronize, but their periods are modified by the beam motion so they are obviously no more accurate.

This review paper is organized as follows. Section 2 briefly describes the history of mechanical clocks. The clock mechanisms necessary for the compensation of the energy dissipation due to friction [47–50] are described. In Section 3 we describe the coupling through elastic structure and explain why this type of coupling is different from other types used in the network synchronization schemes. The main Section 4 recalls original Huygens experiment and discusses the synchronization of two clocks. We give explanation why and under which conditions two clocks can synchronize. We discuss the possibility of the chaotic behavior in pendulum clocks [51]. Section 5 describes the behavior of more than two coupled clocks. We present the results of the numerical studies and the experimental visualization of different types of synchronization. We give theoretical explanation of the existence of only three or five clusters of the synchronized pendula [42,43]. Later, we discuss the influence of the parameter mismatch on the behavior of the system [46]. Finally, we summarize our results in Section 6.

## 2. Pendulum clocks

### 2.1. Brief history of mechanical clocks

In the early-to-mid-14th century, large mechanical clocks began to appear in the towers of several large Italian cities. These clocks were weight-driven and regulated by a verge-and-foliot escapement [48]. This mechanism pre-dates the pendulum and was originally controlled by a foliot, a horizontal bar with a weight at each end [52] (the details of this mechanism design are given in Section 2.2).

A significant advance was the invention of spring-powered clocks between 1500 and 1510 by a German locksmith Peter Henlein [2]. Replacing the heavy drive weights permitted the smaller clocks. Although they slowed down as the mainspring unwound, they were popular among wealthy individuals due to their size and the fact that they could be put on a shelf or table instead of hanging from the wall.

The pendulum clock was invented in 1656 by Ch. Huygens, and patented the following year [53]. The sketches of the first two designs of the pendulum clocks are shown in Fig. 4(a, b). Huygens was inspired by investigations of pendula by Galileo Galilei beginning around 1602. Galileo discovered the key property that makes the pendula the useful timekeepers, i.e., isochronism, which means that the period of swing of a pendulum is approximately the same for different sized swings [54]. He designed the pendulum clock shown in Fig. 5, but there are no evidences that it has ever been built. The introduction of the pendulum, the first harmonic oscillator used in timekeeping, increased the accuracy of the clocks enormously, from about 15 min per day to 15 s per day [55–59,51,60,48] leading to their rapid spread as the existing 'verge and foliot' clocks were retrofitted with pendula.

These early clocks, due to their verge escapements, had wide pendulum swings of up to 100°. Huygens discovered that wide swings made the pendulum inaccurate, causing its period, and thus the rate of the clock to vary with unavoidable variations in the driving force provided by the movement [27,28]. The observation that only the pendula with small swings of a few degrees are isochronous motivated the invention of the anchor escapement around 1670, which reduced the pendulum's swing to 4°–6° [48]. In addition to the increased accuracy, this allowed the clock's case to accommodate longer, slower pendula, which needed less power and caused less wear on the movement.

To summarize the description, all mechanical pendulum clocks have five basis parts as shown in Fig. 6, i.e.:

(i) a power source; either a weight on a cord that turns a pulley, or a spring, (ii) a gear train that steps up the speed of the power so that the pendulum can use it, (iii) an escapement that controls the speed and regularity of the pendulum. It transfers the energy stored in the spring to the motion of the pendulum by means of wheels, gears, and ratchets, i.e., it gives the pendulum precisely timed impulses to keep it swinging, and which releases the gear train wheels to move forward a fixed amount at each swing, (iv) the pendulum, a weight on a rod, (v) an indicator or a dial that records how often the escapement has rotated and therefore how much time has passed, usually a traditional clock face with rotating hands.

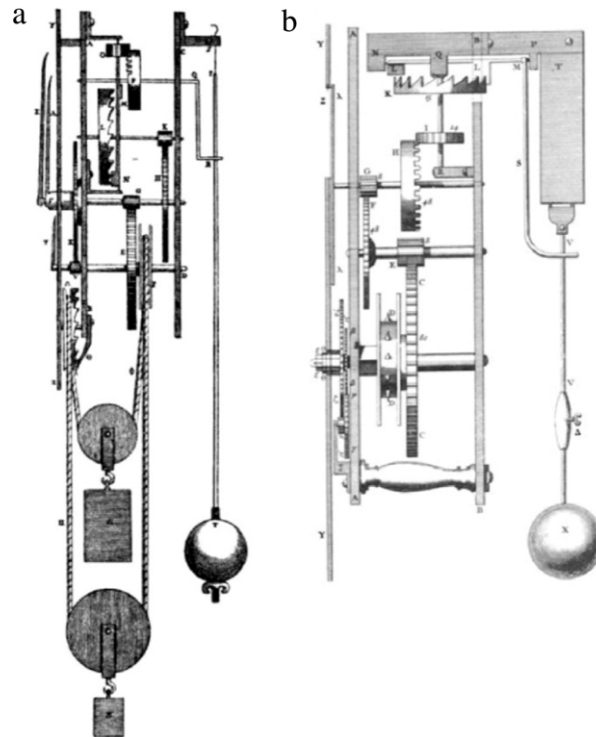


**Fig. 4.** (a) The first pendulum clock, invented by Christiaan Huygens in 1656. (b) The second verge pendulum clock built in 1673.



**Fig. 5.** Pendulum clock conceived by Galileo Galilei around 1637. The earliest known pendulum clock design, it was never completed.

## 2.2. Escapement mechanisms

An escapement transfers energy to the clock's timekeeping element (usually a pendulum or foliot) to compensate the energy dissipation during a cycle as without the energy transfer, the oscillation of the pendulum (foliot) will decay [62]. The

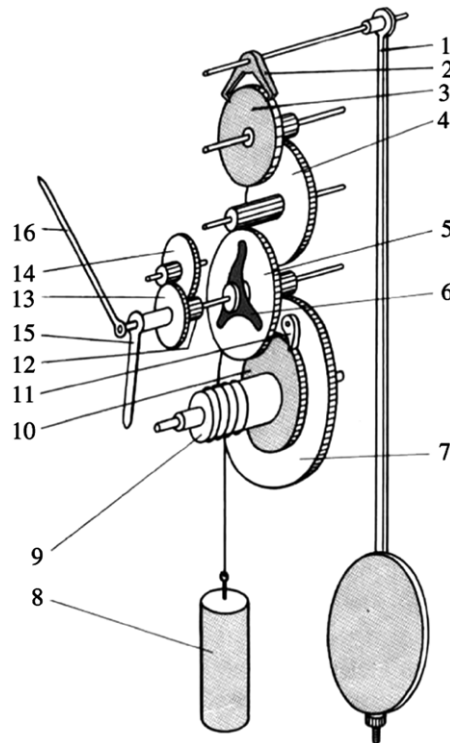


**Fig. 6.** The sketch of the basic components of a pendulum clock with anchor escapement. (after [61]: (1) pendulum; (2) anchor escapement arms; (3) escape wheel; (4–7) gear train; (8) gravity-driven weight; (9–11) energy supply mechanism, (12–14) transition mechanism, (15,16) clock's hands.

escapement may take the energy from a coiled spring or suspended weight [63]. The escapement also permits each cycle of the timekeeping element to be counted. During each cycle, the escapement permits a gear train to advance or “escape” slightly. The periodic advancement results in moving the timepiece’s hands forward at a steady rate.

With each swing of the pendulum, one of its arms releases one tooth of a gear, making it change from a “locked” state to a “drive” state for a short period that ends when another tooth on the gear strikes the opposite arm of the pendulum, which locks the gear again. It is this periodic release of energy and rapid stopping that makes a clock “tick;” it is the sound of the gear train suddenly stopping when the escapement locks again.

The invention of the escapement mechanism has a significant influence on the history of technology as it made the all-mechanical clock possible [2,58]. This development in 13th century Europe initiated a change in timekeeping methods from continuous processes, such as the flow of water in water clocks, to repetitive oscillatory processes, such as the swing of pendula, which could yield more accuracy [64–66].

Greek washstand automaton of the 3rd century BC is the earliest known example of an escapement mechanism [16]. The earliest liquid-driven escapement was described by the Greek engineer Philo of Byzantium (3rd century BC) in his technical treatise *Pneumatics* (chapter 31) as part of a washstand. A counterweighted spoon, supplied by a water tank, tips over in a basin when full, releasing a spherical piece of pumice in the process. Once the spoon has emptied, it is pulled up again by the counterweight, closing the door on the pumice by the tightening string. Philo’s comment that “Its construction is similar to that of clocks” indicates that such escapement mechanisms were already used in ancient water clocks [16].

In China around 723 AD, during the period of the Tang Dynasty Buddhist monk Yi Xing along with government official Liang Lingzan applied the escapement in the water-powered armillary sphere and clock drive [67]. The Song Dynasty (960–1279) era horologists Zhang Sixun and Su Song (1020–1101) duly applied escapement devices in their astronomical clock towers [67,68].

A mercury escapement mechanism has been described in the work of the king of Castile Alfonso X. The knowledge of these mercury escapements may have spread through Europe with translations of Arabic and Spanish texts [69].

None of these were true mechanical escapements, since they still depended on the flow of liquid through an orifice to measure time. For example, in Su Song’s clock water flowed into a container on a pivot. The escapement role was to tip the container over each time it filled up, thus advancing the clock’s wheels each time an equal quantity of water was measured out.

The first mechanical escapement is the verge-and-foliot mechanism invented by Villard de Honnecourt in XIV century Europe. It was a primitive apparatus that was apparently a timekeeping device, but without being subject to any minute requirement of accuracy [58]. It was used in a bell ringing apparatus called an *alarum* for several centuries before it was

adapted to clocks [66]. In 14th century Europe it appeared as the timekeeper in the first mechanical clocks, which were large tower clocks. Its origin and first use is unknown because it is difficult to distinguish which of these early tower clocks were mechanical, and which were water clocks. However, indirect evidence, such as a sudden increase in cost and construction of clocks, points to the late 13th century as the most likely date for the development of the modern clock escapement. The astronomer Robertus Anglicus wrote in 1271 that clockmakers were trying to invent an escapement, but had not been successful yet [70].

On the other hand, most sources agree that mechanical escapement clocks existed by 1300. The earliest description of the mechanical escapement can be found in Richard of Wallingford's manuscript *Tractatus Horologii Astronomici* of 1327 AD, on the clock he built at the Abbey of St. Albans. (Jones, 2000, Dohrn-van Rossum, 1996). It consisted of a pair of escape wheels on the same axle, with alternating radial teeth. The verge rod was suspended between them, with a short crosspiece that rotated first in one direction and then the other as the staggered teeth pushed past.

Unlike the continuous flow of water in the Chinese device, the European medieval escapements were characterized by a regular, repeating sequence of discrete actions and the capability of self-reversing action. Both techniques used escapements, but these have only the name in common. The Chinese one worked intermittently; the European, in discrete but continuous beats. Both systems used gravity as the prime mover, but the action was very different. In the mechanical clock, the falling weight exerted a continuous and even force on the train, which the escapement alternately held back and released at a rhythm constrained by the controller. Ingeniously, the very force that turned the scape wheel then slowed it and pushed it part of the way back. In other words, a unidirectional force produced a self-reversing action—about one step back for three steps forward. In the Chinese timekeeper, however, the force exerted varied, the weight in each successive bucket increases until it is sufficient to tip the release and lift the stop that held the wheel in place. This allowed the wheel to turn some ten degrees and bring the next bucket under the stream of water while the stop fell back. In the Chinese clock, then unidirectional force produced unidirectional motion [71].

The verge-and-foliot was the standard escapement used in every other early clock and watch and remained the only escapement for 400 years [72]. Its friction and recoil limited its performance but the accuracy of these 'verge-and-foliot' clocks was more limited by their early foliot type balance wheels, which because they lacked a balance spring had no natural 'beat', so there was not much incentive to improve the escapement [73].

The great leap in accuracy resulting from the invention of the pendulum and balance spring around 1657, which made the timekeeping elements in both watches and clocks harmonic oscillators, focused attention on the errors of the escapement and more accurate escapements soon superseded the verge. The next two centuries, the 'golden age' of mechanical horology, saw the invention of perhaps 300 escapement designs [31,32,74,75], although only about 10 stood the test of time and were widely used [76]. The reliability of an escapement depends on the quality of workmanship and the level of maintenance given [77]. A poorly constructed or poorly maintained escapement will cause problems. The escapement must accurately convert the oscillations of the pendulum or balance wheel into rotation of the clock or watch gear train, and it must deliver enough energy to the pendulum or balance wheel to maintain its oscillation. The most accurate commercially produced mechanical clock was the Shortt-Synchronome free pendulum clock invented by W.H. Shortt in 1921, which had an error rate of about 1 s per year [76].

Now, let us describe in more details two most commonly used escapement mechanisms.

### 2.2.1. Verge-and-foliot escapement

The earliest escapement in Europe (from about 1275) was the verge escapement, also known as the crown-wheel escapement. It was used in the first mechanical clocks and was originally controlled by a foliot, a horizontal bar with weights at either end. The sketch of the verge-and-foliot mechanism is shown in Fig. 7. A vertical shaft (verge) is attached to the middle of the foliot and carries two small plates (pallets) sticking out like flags from a flag pole. One pallet is near the top of the verge and one near the bottom and looking end-on down the verge the pallets are a little over ninety degrees apart. The escape wheel is shaped somewhat like a crown and turns about a horizontal axis. The mechanism is driven by a constant torque  $\tau$  applied to the crown gear. This torque is usually provided by a mass hanging from a rope which is wound around the shaft. The verge spins freely at all times except at the instant a collision takes place. Energy is assumed to leave the system only through the collisions. The amount of energy lost during each collision is a function of the system geometry as well as the coefficient of restitution realized in the collision [47]. As the wheel tries to turn, one tooth of the wheel pushes against the upper pallet and starts the foliot moving. As the tooth pushes past the upper pallet, the lower pallet swings into the path of the escape wheel. The momentum of the moving foliot pushes the escape wheel backwards but eventually the system comes to rest. It is now the turn of the lower pallet to push the foliot and so on. The system has no natural frequency of oscillation – it is simply force pushing inertia around. Verge-and-foliot mechanisms reigned for more than 300 years with variations in the shape of the foliot. All had the same basic problem: the period of oscillation of this escapement depended heavily on the amount of driving force and the amount of friction in the drive and was difficult to regulate.

A disadvantage of the escapement was that each time a tooth lands on a pallet, the momentum of the foliot pushes the crown wheel backwards a short distance before the force of the wheel reverses the motion. This is called "recoil" and was a source of wear and inaccuracy.

Let the crown gear and the verge have inertias  $I_c$  and  $I_v$ , contact radii  $r_c$  and  $r_v$ , and angular velocities ( $\dot{\theta}_c(t)$ , and  $\dot{\theta}_v(t)$ ), respectively. The velocities before and after a collision are denoted by the subscripts 0 and 1, respectively. The motion of the

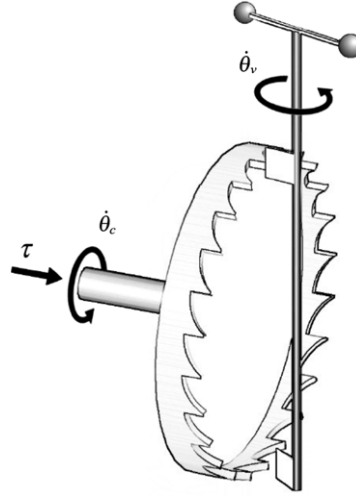


Fig. 7. Verge-and-foliot escapement mechanism (after [47]).

crown gear and verge is governed by the equations

$$\ddot{\theta}_c(t) = \frac{1}{I_c} \tau - \frac{r_c}{I_c} F(\theta_c(t), \theta_v(t), \dot{\theta}_c(t), \dot{\theta}_v(t)) \quad (1)$$

$$\ddot{\theta}_v(t) = \begin{cases} +\frac{r_v}{I_v} F(\theta_c(t), \theta_v(t), \dot{\theta}_c(t), \dot{\theta}_v(t)), & \text{upper} \\ -\frac{r_v}{I_v} F(\theta_c(t), \theta_v(t), \dot{\theta}_c(t), \dot{\theta}_v(t)), & \text{lower} \end{cases} \quad (2)$$

where the first expression in Eq. (2) applies to the collisions between the crown gear and the upper paddle, and the second expression applies to the collisions between the crown gear and the lower paddle. The function  $F(\theta_c(t), \theta_v(t), \dot{\theta}_c(t), \dot{\theta}_v(t))$  is the collision force, which is zero when the crown gear and verge are not in contact and is impulsive at the instant of impact. The collision force  $F$  acts equally and oppositely on the crown gear and verge. Let us define

$$\sigma \triangleq \begin{cases} +1, & \text{upper} \\ -1, & \text{lower} \end{cases} \quad (3)$$

and rewrite Eq. (2) in the following form

$$\ddot{\theta}_v(t) = \sigma \frac{r_v}{I_v} F(\theta_c(t), \theta_v(t), \dot{\theta}_c(t), \dot{\theta}_v(t)). \quad (4)$$

To determine the collision force, one can integrate Eqs. (1) and (4) across a collision, i.e.,

$$\dot{\theta}_{c1} - \dot{\theta}_{c0} = \lim_{\Delta t \rightarrow 0} \left( \frac{1}{I_c} \int_{t-\Delta t}^{t+\Delta t} \tau ds - \frac{r_c}{I_c} \int_{t-\Delta t}^{t+\Delta t} F(s) ds \right) \quad (5)$$

$$\dot{\theta}_{v1} - \dot{\theta}_{v0} = \lim_{\Delta t \rightarrow 0} \left( \sigma \frac{r_v}{I_v} \int_{t-\Delta t}^{t+\Delta t} F(s) ds \right). \quad (6)$$

Eliminating the integrated collision force in Eqs. (5) and (6) yields

$$\frac{\sigma I_v}{r_v} \dot{\theta}_{v0} + \frac{I_c}{r_c} \dot{\theta}_{c0} = \frac{\sigma I_v}{r_v} \dot{\theta}_{v1} + \frac{I_c}{r_c} \dot{\theta}_{c1} \quad (7)$$

which is an expression of conservation of linear momentum at the instant of a collision. Eq. (7) can be rewritten as

$$M_v V_{v0} + M_c V_{c0} = M_v V_{v1} + M_c V_{c1} \quad (8)$$

where  $M_c = I_c/r_c^2$  and  $M_v = I_v/r_v^2$  are the effective crown gear mass and effective verge mass, respectively, and  $V_c$  and  $V_v$  are the tangential velocities of the crown gear and the verge, respectively ( $V_c \doteq r_c \dot{\theta}_c(t)$ , and  $V_v = r_v \dot{\theta}_v(t)$ ).

The coefficient of restitution  $e$  relates the linear velocities of the crown gear and the verge before and after the collision according to

$$V_{c1} - V_{c0} = -e(V_{c0} - V_{v0}) \quad (9)$$

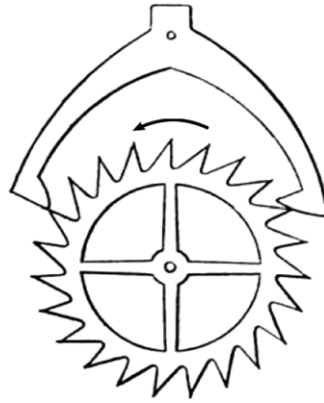


**Fig. 8.** Anchor escapement.

which accounts for the loss of kinetic energy in a collision. Solving Eqs. (7) and (9) yields

$$\Delta\dot{\theta}_c = -\frac{M_v(1+e)}{r_c(M_v+M_c)}V_{c0} + \sigma\frac{M_v(1+e)}{r_c(M_v+M_c)}V_{v0} \quad (10)$$

$$\Delta\dot{\theta}_v = \sigma\frac{M_c(1+e)}{r_v(M_v+M_c)}V_{c0} - \frac{M_c(1+e)}{r_v(M_v+M_c)}V_{v0} \quad (11)$$

where  $\Delta\dot{\theta}_c \triangleq \dot{\theta}_{c1} - \dot{\theta}_{c0}$ ,  $\Delta\dot{\theta}_v \triangleq \dot{\theta}_{v1} - \dot{\theta}_{v0}$  are the impulsive changes in angular velocity when a collision occurs. These quantities depend on the geometry as well as the velocities immediately before the collision. The integral of the impulsive force function over a collision event is

$$\int_{t_0}^{t_1} F(s) ds = \frac{M_c M_v (1+e)}{M_v + M_c} (V_{c0} - V_{v0}) \quad (12)$$

where  $t_0$  is time slightly before the collision and  $t_1$  is time slightly after the collision.

The verge was the only escapement used in clocks and watches for 400 years. It was used in the first pendulum clocks for about 50 years after the pendulum clock was invented in 1656. In a pendulum clock the crown wheel and verge were oriented so they were horizontal, and the pendulum hung from the verge. However the verge is the most inaccurate of the common escapements, and after modern timekeeping oscillators (the pendulum and the sprung balance wheel) were introduced in the 1650s the verge was replaced by other escapements [78].

### 2.2.2. Anchor escapement

The anchor escapement mechanism shown in Fig. 8 was invented by Robert Hooke around 1660, the anchor quickly superseded the verge to become the standard escapement used in pendulum clocks through the 19th century. Its advantage was that it reduced the wide pendulum swing angles of the verge to  $3^\circ$ – $6^\circ$ , making the pendulum isochronous, and allowing the use of longer, slower moving pendula, which used less energy. It is responsible for the long narrow shape of most pendulum clocks.

It consists of an escape wheel with pointed, backward slanted teeth, and an ‘anchor’ shaped piece pivoted above it which rocks from side to side, attached to the pendulum. The anchor has slanted pallets on the arms which alternately catch on the teeth of the escape wheel, receiving impulses. Mechanically its operation has similarities to the verge escapement, and it has two of the verge’s disadvantages: (1) The pendulum is constantly being pushed by an escape wheel tooth throughout its cycle, and is never allowed to swing freely, which disturbs its isochronism, and (2) it is a *recoil* escapement; the anchor pushes the escape wheel backward during part of its cycle. This causes a backlash, an increased wear in the clocks gears, and inaccuracy. These problems were eliminated in the deadbeat escapement, which slowly replaced the anchor in precision clocks.

The deadbeat escapement of Fig. 9 was an improvement of the anchor escapement first made by Thomas Tompion to a design by Richard Towneley in 1675 although it is often credited to Tompion’s successor George Graham who popularized it in 1715 [48,58]. In the anchor escapement the swing of the pendulum pushes the escape wheel backward during part of its cycle. This ‘recoil’ disturbs the motion of the pendulum, causing inaccuracy, and reverses the direction of the gear train, causing backlash and introducing high loads into the system, leading to friction and wear. The main advantage of the deadbeat is that it eliminated a recoil [66].

In the deadbeat, the pallets have a second curved “locking” face on them, concentric about the pivot the anchor turns on. During the extremities of the pendulum’s swing, the escape wheel tooth rests against this locking face, providing no impulse to the pendulum, which prevents the recoil. Near the bottom of the pendulum’s swing the tooth slides off the

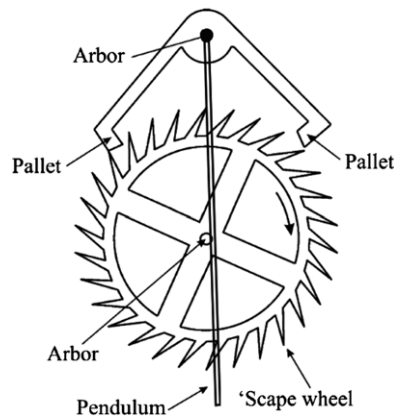


Fig. 9. Deadbeat escapement mechanism.

locking face onto the angled “impulse” face, giving the pendulum a push, before the pallet releases the tooth. This was the first escapement to separate the locking and impulse actions of the escapement. The deadbeat was first used in precision regulator clocks, but due to greater accuracy superseded the anchor in the 19th century. It is used in almost all modern pendulum clocks.

Now let us describe the dynamics of a typical anchor mechanism as shown in Fig. 10(a)–(c).

The escapement mechanism consists of the scape wheel (details are shown in Fig. 10(b)) and two anchor pallets mounted on the pendulum axis (details are shown in Fig. 10(c)). The energy is supplied by a wound spring connected with the scape wheel. The escapement mechanism acts as shown in Fig. 11(a)–(d). In the first stage one of the triangle shaped teeth of the scape wheel impacts the pallet I. For the angle of pendulum displacement  $\varphi < 0$  (Fig. 11(a)) surface A of the pallet I slides on the top edge of the triangle teeth 1 and excitation moment  $M = 0$ . In the case of  $0 < \varphi < \gamma_N$  (Fig. 11(b)) the edge of the pallet I is in contact with the side surface of the teeth 1 and the horizontal component of the reaction generates excitation moment  $M_N$ . When increasing  $\varphi$  passes critical value  $\gamma$ , pallet I slides off the teeth 1 and the second stage of the mechanism acting starts. The teeth 1 impacts on the pallet II. For  $\varphi > 0$  (Fig. 11(c)) surface B of the pallet II slides on the edge of the teeth 1 and no excitation moment is generated. When  $-\gamma_N < \varphi < 0$  (Fig. 11(d)) the edge of the pallet II is in contact with the side surface of the teeth 1 and the horizontal component of the reaction generates excitation moment  $-M_N$ . When  $\varphi$  exceeds the critical value  $-\gamma_N$ , i.e.,  $\varphi < -\gamma_N$  the pallet II slides off the teeth 1. Next, the successive teeth 2 impacts pallet I and the first stage starts again. Notice that when maximum absolute value of  $\varphi$  is smaller than  $\gamma_N$  the escapement mechanism does not work (the transition from step I to step II is impossible) and the pendulum tends to the equilibrium position  $\varphi = 0$ .

### 2.3. Dynamics of clocks

The pendulum clock is an oscillatory mechanism with self-excited oscillations whose amplitude is independent of the initial conditions (dynamical system has a stable limit cycle attractor [79–81]). To start the oscillations a rather strong initial impulse is required; failing this the clock goes back to rest, i.e., dynamical system has an additional fixed point attractor which is obtained for the initial conditions close to zero. For certain positions of the pendulum the control operates and allows the required energy to pass in the form of an impulse [82–84]. The duration of the impulse varies from clock to clock, but in the good clocks it is quite short. The control operates generally twice per period, close to the position of equilibrium, i.e. where the velocity is the greatest. An important feature is that the moment when the control operates depends solely on the position of the pendulum. Furthermore its action, and notably the magnitude of the impulse, depends on the state of the pendulum. Hence the whole operation depends on the position and velocity of the parts and not on time. Thus a clock is an autonomous system [50]. The main properties of the clock’s model are summarized in Fig. 12. The initial conditions starting in the shaded region after a finite number of pendulum’s oscillations lead to the equilibrium (0, 0), while these starting in the rest of the plane tend to the limit cycle (shown in red).

For simplicity, we can assume that the control acts once in each period of the pendulum, producing an instantaneous change in velocity. One can consider two “laws of impulse”, one asserting that the change in velocity is constant, the other that the change in kinetic energy is constant, i.e., if  $v_0$  and  $v_1$  are the velocities of the pendulum just before and after the impulse, the first states that  $mv_1 - mv_0 = \text{constant}$ , the second that  $mv_1^2 - mv_0^2 = \text{constant}$ . The second is very natural since it holds exactly when the unwinding mechanism consists of a weight which is displaced downward the same distance (thus doing the same work) in each period. Of the two assumptions, the second is more plausible since it asserts that each impulse contributes the same amount of energy. The first assumption may imply a larger change of energy for some impulses than for others; the lower the velocity before the impulse the less energy transferred to the system. In addition to the nature of the impulse there are also hypotheses to be made regarding friction. The simplest are: (a) linear friction, or friction proportional to the velocity; (b) constant friction. The friction in an actual clock is partly of a constant type, as in that of control and partly

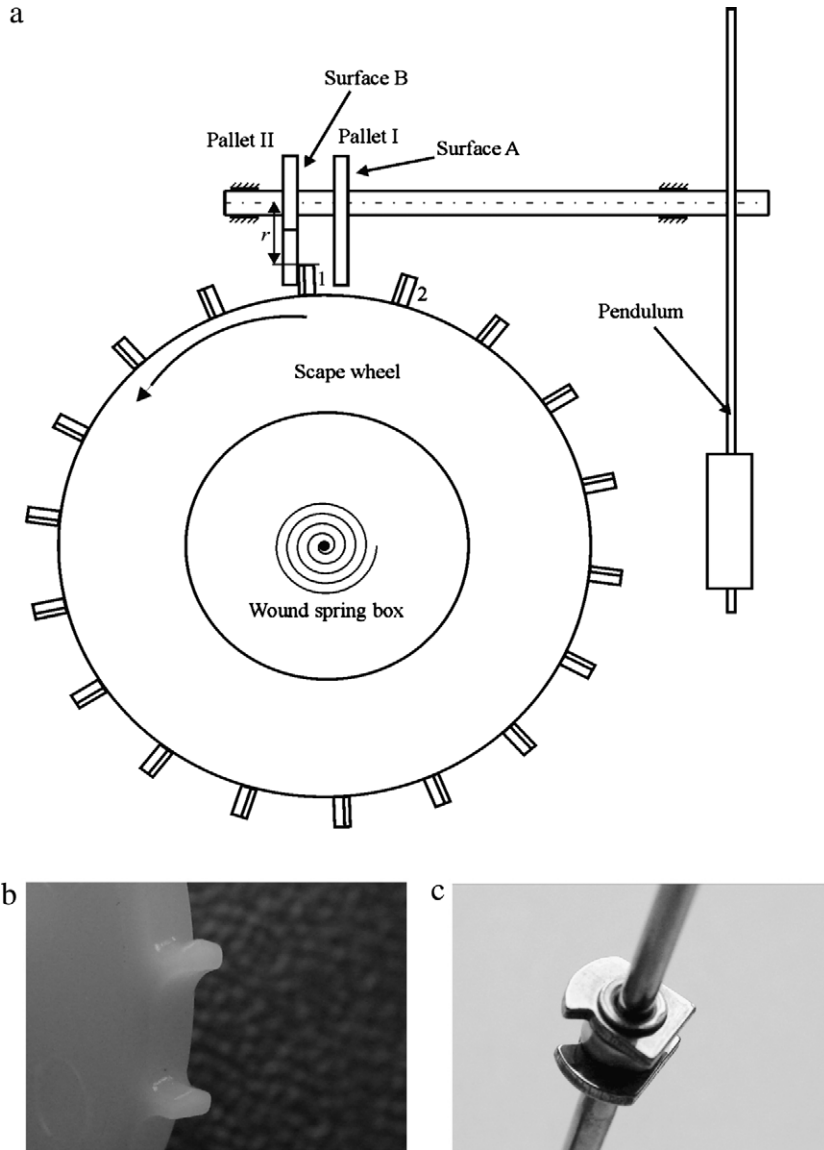


**Fig. 10.** Anchor escapement mechanism; (a) scheme of the mechanism, (b) view of the scape wheel, (c) view of the anchor pallets.

variable, as in that from the air resistance of the pendulum. Constant friction is related to the property of soft self-excitation and the necessity of a strong impulse to start the periodic limit cycle oscillations. In [50] one can find the proof that the model considering the second impulse law and a combination of both types of friction can exhibit a limit cycle behavior and capture the main properties of the clocks.

(i) *Discontinuous model*

The equation of motion of the clock's pendulum is as follows:

$$ml^2\ddot{\varphi} + c_\varphi\dot{\varphi} + mgl \sin \varphi = M_D, \quad (13)$$

where  $M_D$  is the momentum supplied by the escapement mechanism (see Section 3.2), i.e., in the first stage if  $0 < \varphi < \gamma_N$  then  $M_D = M_N$  and when  $\varphi < 0$  then  $M_D = 0$  and for the second stage one has for  $-\gamma_N < \varphi < 0$   $M_D = -M_N$  and for  $\varphi > 0$   $M_D = 0$ . When  $\max \varphi(t) < \gamma_N$  there are switches between two stages and  $M_N = 0$ . Eq. (13) describes the dynamical system which performs the self-excited oscillations [50].

The clocks are designed in such a way that the pendula perform periodic motion with a period  $2\pi/\alpha$  where  $\alpha$  is constant. The escapement mechanism provides the necessary amount of energy to compensate the dissipation and makes the pendulum motion periodic. Under these assumption in the stable motion of the clock's pendula has been approximated by:

$$\varphi = \Phi \sin(\alpha t), \quad (14)$$

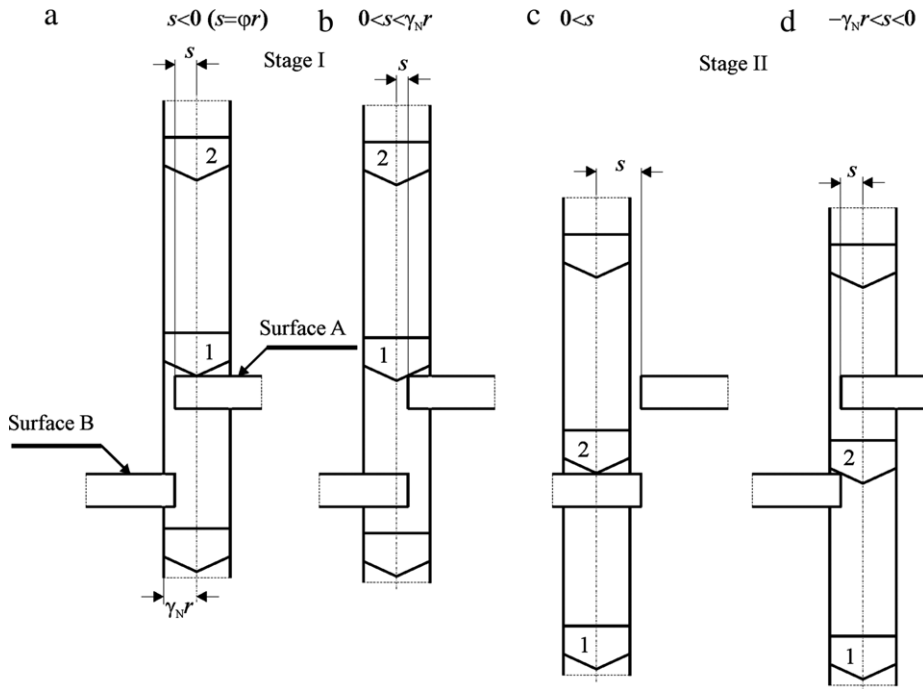


Fig. 11. Acting of the escapement mechanism.

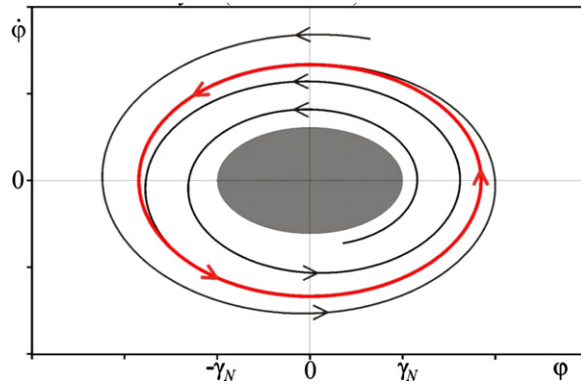


Fig. 12. An autonomous model of the clock. (For interpretation of the references to colour in this figure legend, the reader is referred to the web version of this article.)

where  $\Phi$  is constant. The continuous solution given by Eq. (14) is a good approximation of the pendula' oscillations calculated from discontinuous equation (13) as can be seen in Fig. 13. A stable limit cycle calculated from Eq. (13) is shown in blue while the approximation given by Eq. (14) is shown in red. Notice that for initial conditions  $-\gamma_N < \varphi_0 < \gamma_N$ ,  $-\alpha\gamma_N\dot{\varphi}_0 < \gamma_N$  Eq. (13) has a stable fixed point attractor at  $(0, 0)$ .

Typically pendulum clocks oscillate with amplitude smaller than  $2\pi/36$  and for clocks with long pendula like marine clocks this amplitude is even smaller [48].

(ii) Moon's model

In a series of papers [59,51,60], the following mathematical model has been considered. It involves the impact as a generic model designed to capture the essential features for chaos in clocks.

The model incorporates the following assumptions and features: (i) the pendulum is modeled by a linear harmonic oscillator with light damping, (ii) the impact dynamics in the escapement and the propagation of structural dynamics through bearings with gaps is modeled by a cubic oscillator of the Duffing-type coupled linearly [85–87] to the pendulum equation, (iii) the driving gear train torque and static friction lock-up are modeled by a threshold condition of structural impact velocity as measured by the Duffing oscillator, and (iv) the driving torque from the weight-driven gear train, when released by the Duffing oscillator noise, acts to add energy through the escapement pallet when the pendulum velocity is positive.

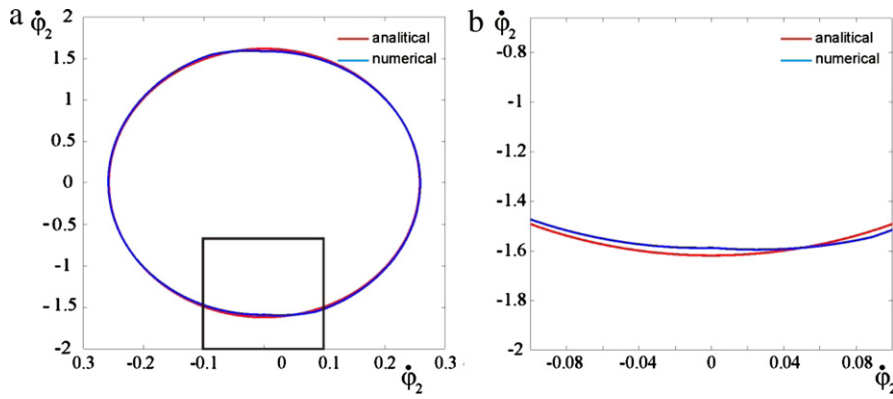


**Fig. 13.** Comparison of the numerical solution of discontinuous equation (13) with the harmonic assumption (14). (For interpretation of the references to colour in this figure legend, the reader is referred to the web version of this article.)

The first assumption (i) is based on the fact that the pendula in clocks rotate through a very small amplitude such that the nonlinear effects are not important [88,8]. The linear oscillator assumption is also good for balance wheel clocks. The second assumption (ii) is motivated by the research on the propagation of stress waves in structures. Both the experimental and the theoretical research show that a single impact or a step input load on a structure leads to complex wave patterns through reflections and dispersions which excite many modes in the structure. Thus, the escapement impact energy redistribution can propagate into the gear train, break the friction and prevent the lock-up. These assumptions lead to the following equations of motion for the coupled pendulum, structural dynamics and driving train. This fourth-order model employs a vibration-sensitive torque to capture the escapement impact:

$$\ddot{x}_1 + \beta_1 \dot{x}_1 + \omega_1^2 x_1 + \alpha_1 x_3 = tq(x_3) \text{sign}(\dot{x}_1) \quad (15)$$

$$\ddot{x}_3 + \beta_2 \dot{x}_3 + \omega_2^2 x_3 + \kappa x_3^3 + \alpha_2 x_1 = 0 \quad (16)$$

where

$$\begin{aligned} tq(\dot{x}_3) &= T_0 \quad \text{if } \dot{x}_3^2 > \delta \text{ and } 0 < x_1 < \Delta \\ tq(\dot{x}_3) &= 0 \quad \text{otherwise.} \end{aligned}$$

Here  $x_1(t)$  represents the motion of the pendulum or balance wheel oscillator;  $x_3(t)$  represents the motion of the structural connection between the escapement and the driving train; the cubic term is a nonlinear surrogate for the gaps between bearings and gear teeth. The torque dependence on structural velocity is an attempt to capture the static friction in the drive train and its dependence on the structural vibration.

The frequency  $\omega_1$  represents the regular motion of the clock oscillator. The damping constants  $\beta_1$  and  $\beta_2$  measure the oscillator and structural damping, respectively. The escapement torque is only applied when the amplitude is in a given sector of the phase space, e.g.  $0 < x_1 < \Delta$ . Thus,  $\Delta$  should be a small fraction of the limit cycle amplitude. In addition, the noise threshold to release the gears and apply the escapement torque is measured by constant  $\delta$ .

To ensure that the model does not generate vibrations when the impact torque  $t_q$  is zero, an energy function can be constructed that places restrictions on the constants in the above model. Multiplying the first equation above by  $\alpha_2(dx_1/dt)$ , the second equation by  $\alpha_1(dx_2/dt)$  and adding, one comes up with the following energy equation:

$$\frac{d}{dt} [T + V] = \alpha_2 tq(\dot{x}_3) \dot{x}_1 - \alpha_2 \beta_1 \dot{x}_1^2 - \alpha_1 \beta_2 \dot{x}_3^2 \quad (17)$$

where

$$\begin{aligned} T &= \frac{1}{2} (\alpha_2 \dot{x}_1^2 + \alpha_1 \dot{x}_3^2) \\ V &= \frac{1}{2} (\alpha_2 \omega_1^2 x_1^2 + \alpha_1 \omega_2^2 x_3^2 + 2\alpha_1 \alpha_2 x_1 x_2) + \frac{1}{4} \alpha_1 \kappa x_3^4. \end{aligned}$$

Here  $T$  acts like a kinetic energy function and  $V$  like the potential energy function. To ensure energy decay when  $tq = 0$ , both  $\alpha_1$  and  $\alpha_2$  must be positive as well as the nonlinear stiffness constant,  $\kappa$ . When the torque is active, the product,  $tq(dx_1/dt)$ , must be also be positive, thus the reason for appearance of the  $\text{sign}(dx_1/dt)$  function in the model.

### (iii) Impulsive differential equations' model

In this section we describe the equations of motion of the escapement mechanism in the form of an impulsive differential equation [89,90,47]. An impulsive differential equation is described by three components; namely, a continuous time differential equation, which governs the system state between the impulses, an impulse equation, which models an

impulsive jump defined by a jump function at the instant an impulse occurs, and a jump criterion, which defines a set of jump events in which the impulse equation is active. These components can be written in the form

$$\dot{x}(t) = f_c(x(t)), \quad x(t) \notin S \tag{18}$$

$$\Delta x(t) = f_d(x(t)), \quad x(t) \in S \tag{19}$$

where  $t \geq 0$ ,  $x \in \mathbf{R}^n$ ,  $f_c : \mathbf{R}^n \rightarrow \mathbf{R}^n$  is locally Lipschitz continuous;  $f_d : \mathbf{R}^n \rightarrow \mathbf{R}^n$  is continuous; and  $S \in \mathbf{R}^n$  is the jump set. Eqs. (18) and (19) describe the impulsive dynamical system  $G$ .

The dynamics of the verge and foliot escapement mechanism as an impulsive differential equation define the state

$$x = [x_1, x_2, x_3, x_4]^T \triangleq [\theta_1, \theta_2, \dot{\theta}_3, \dot{\theta}_4]^T \tag{20}$$

where  $x_1$  is the position of the crown gear, that is, the counterclockwise angle swept by the line connecting the center of the crown gear and the 0-th tooth from the 12 o'clock position;  $x_2$  is the position of the verge, that is, the deviation of the mean line of the angular offset between two paddles from the vertical plane perpendicular to the plane of the crown gear;  $x_3$  is the angular velocity of the crown gear; and  $x_4$  is the angular velocity of the verge. Between collisions the state satisfies

$$\dot{x}(t) = \begin{bmatrix} 0 & 0 & 1 & 0 \\ 0 & 0 & 0 & 1 \\ 0 & 0 & 0 & 0 \\ 0 & 0 & 0 & 0 \end{bmatrix} x(t) + \begin{bmatrix} 0 \\ 0 \\ 1/I_c \\ 0 \end{bmatrix} \tau$$

while the jump function is given by

$$f_d(x) = \begin{bmatrix} 0 & 0 & 0 & 0 \\ 0 & 0 & 0 & 0 \\ 0 & 0 & -r_c G_c & \sigma r_v G_c \\ 0 & 0 & \sigma r_c G_v & -r_v G_v \end{bmatrix} x$$

where

$$G_c \triangleq \frac{(I_v/r_v^2)(1+e)}{r_c((I_v/r_v^2) + (I_c/r_c^2))}, \quad G_v \triangleq \frac{(I_c/r_c^2)(1+e)}{r_v((I_v/r_v^2) + (I_c/r_c^2))}.$$

The jump set is

$$S = \left\{ \bigcup_{m=0}^n S_m^{upper} \right\} \cup \left\{ \bigcup_{m=0}^n S_m^{lower} \right\}$$

where, for  $m = 0, \dots, n$

$$S_m^{upper} = \left\{ \begin{array}{l} x : r_c \sin(x_1 - m\alpha_c) = r_v \tan(x_2 + \alpha_v/2), \\ \quad r_c x_3 - r_v x_4 > 0, \\ (m - 1/2)\alpha_c + 2p\pi \leq x_1 \leq (m + 1/2)\alpha_c + 2p\pi, \\ \quad p \in \{0, 1, 2, \dots\} \end{array} \right\}$$

$$S_m^{lower} = \left\{ \begin{array}{l} x : r_c \sin(m\alpha_c - x_1) = r_v \tan(-x_2 + \alpha_v/2), \\ \quad r_c x_3 + r_v x_4 > 0, \\ (m - 1/2)\alpha_c + (2p - 1)\pi \leq x_1 \leq (m + 1/2)\alpha_c + (2p - 1)\pi, \\ \quad p \in \{0, 1, 2, \dots\} \end{array} \right\}$$

where  $\alpha_c$  is the angle between neighboring teeth on the crown gear,  $\alpha_v$  is the angular offset of the paddles about the vertical axis,  $m$  is the index of the crown gear tooth involved in the collision and  $p$  is the number of full rotations of the crown gear. The crown gear teeth are numbered from 0 to  $n$  clockwise, or opposite the direction of increasing  $\theta_c$ , beginning at  $\theta_c = 0$ . There must be an odd number of crown gear teeth for the mechanism to function correctly, and thus  $n$  is even.

(iv) *Continuous model with van der Pol's damping*

Instead of the models with an impulse supply of energy to the clock pendulum (i–iii), a van der Pol oscillator model with a continuous supply of energy can be considered [91,8,40,41]. In this case the equation of motion of a single pendulum clock is as follows,

$$\frac{d^2\theta}{dt^2} + \frac{mr_{c.m.}}{l} \sin \theta + \epsilon \left[ \left( \frac{\theta}{\theta_0} \right)^2 - 1 \right] \frac{d\theta}{dt} = 0 \tag{21}$$

where  $\theta$  is the angle the pendulum makes with the vertical,  $l$  is the moment of inertia of the pendulum,  $m$  is the mass of the pendulum,  $r_{c.m.}$  is the distance of the pendulum's center of mass from the pivot point,  $g$  is the acceleration of gravity, and  $x$  is the horizontal position of the base. The first two terms in Eq. (21) are the usual ones that describe the motion of a pendulum, that is, the angular acceleration and the gravitational torque. The third term in Eq. (21) crudely models the escapement mechanism and any damping of the bob's motion from air resistance. This term is of van der Pol's type and increases the angular velocity for  $\theta < \theta_0$  and decreases it for  $\theta > \theta_0$ . For small  $\epsilon$ , this term will produce stable oscillations with an amplitude of approximately  $2\theta_0$  in the isolated oscillator.

### 3. Modeling Huygens' experiment: coupling through elastic structure

#### 3.1. Coupling in Huygens' experiment

In his letters Huygens limited himself to explaining the observed phenomenon of synchronization by describing the setup (as shown in Figs. 1 and 2), noting the basic coupling mechanism, and describing how a steady synchronized state is approached. Huygens originally thought the coupling was due to imperceptible air-borne forces transmitted between the pendula of the two clocks (letter to his father [5]), but within a few days he realized (letter to Moray [5]) that the coupling was due to structure-based forces. Huygens' published explanation can be summarized in the following way: the common beam [28] or the two coupled beams [5] from which the extended clock cases are suspended can move (oscillate) horizontally, at least with small amplitudes. The two pendula, oscillating in the same (or parallel planes), transmit through their pivots the oscillating forces on two clock-cases, which, in turn, transmit through their pivots the oscillating forces on the beams which cause them to oscillate. Only in the case of the two pendula which started in ideal opposition, the zero resultant oscillating force on the beams causes the beams to stay in the equilibrium position. As the two nearly identical clocks initially run at slightly different speeds their pendula eventually get in opposition, two oscillating force components almost completely cancel, and the motion of the beams goes to zero. Then two clocks adjust their speeds, and their pendula remain in opposition. Huygens had noted two basic features of his setup—the clocks adjusting their speeds to common speed (Huygens' two clocks, when running independently, differed by daily average times that ranged from  $-0.5$  to  $6$  (s) [28]; and the structure-based origin of the coupling forces.

This type of coupling is different from the one used in the most studies of the coupled oscillatory systems or coupled networks (e.g., [8–10,92,6]) where the signal from one of the oscillators (network nodes) is transmitted directly to few (or all) of other oscillators and influence its behavior. If the particular oscillator is  $n$  dimensional the dimension of the coupled system (network) is equal to  $Nn$ , where  $N$  is a number of oscillators coupled in the considered system. In the Huygens type coupling the oscillators are coupled to the additional  $M$  dimensional dynamical system B. The signals from the oscillators are transferred to system B and influence its dynamical behavior. Simultaneously, the signals from system B are transmitted to the oscillators also changing its dynamics. The transfer of any signal from one oscillator to another occurs always through the system B. In the consideration of the dynamics of the coupled system one has to consider  $Nn + M$  dimensional model. As in the mechanical systems (like Huygens' setup) this additional system B is usually an elastic structure. We call this type of coupling as the coupling through elastic structure [93–95]. Later in this section and Section 4 we describe how the energy is transferred from one clock to another via the beam.

The studies of the dynamics of the systems coupled through the elastic structure have been also stimulated by the events on the Millennium Bridge. On the opening day the Millennium Bridge, a pedestrian footbridge crossing the Thames River in London, was observed to exhibit a pronounced lateral wobbling as more and more people streamed onto the bridge [21,22,24,23,96,97,20]. This phenomenon apparently occurred due to a resonance between a low order bridge oscillation mode and the natural average stepping frequency of human walkers: a small initial oscillation of the bridge induces some of the walkers to synchronize the timing of their steps to that of the bridge oscillations, thus exerting a positive feedback force on the bridge that derives the bridge oscillation to higher amplitude, eventually resulting in a large steady-state oscillation. Subsequent studies by the bridge builder showed that the oscillations did not develop unless the number of the pedestrians on the bridge was greater than a critical value [21,22]. Generally, the phenomenon on the Millennium Bridge can be considered as a particularly dramatic example of the emergence of global collective behavior in the systems of many coupled heterogeneous oscillators [18]. The examples of this general type of emergent behavior are known in biology (e.g. synchronization of pacemaker cells in the heart [98] and of neurons governing day–night rhythms in mammals [19,13], chemistry [15]).

The analysis of the coupled periodic oscillators can be based on Malkin's theorem [7,99,100]. It gives general conditions under which weakly connected periodic oscillators can be reduced to the analysis of the corresponding phase model. Recently, this approach has allowed the derivation of a number of important results, mainly on the Kuramoto model [3]. The discontinuity of the clock model does not allow the application of this method in most of our models. In the case of continuous model (Eqs. (68) and (69) in Section 3.5) the analysis based on Malkin's theorem will be reduced to the analysis of coupled van der Pol's oscillator presented in [3].

#### 3.2. Senators' five degrees of freedom model

Korteweg studies [101] gave further explanations of Huygens' observed phenomena. He developed a dissipationless, three-degree-of-freedom, linear model that represents some features of the original setup of Fig. 1 (his model is essentially equivalent to the one formed from the five-body (two clocks cases, two pendula and a beam) system shown in Fig. 1 by clamping each extended clock-case to its support beam, removing all friction, and removing the escapements). Korteweg then investigated how the observed natural frequencies and mode shapes would vary as model's parameters vary, and used his study results to make the hypothesis that explained the observed behavior of Huygens' real system. Korteweg's basic idea can be summarized as follows: the stable, steady-state motions of the real, nonlinear, two coupled clock system can be approximately represented by his model vibrating in one of its normal modes at the corresponding natural frequency. The

approximating mode and its frequency are found by: (i) adding linear friction to the model, (realistically assuming that the pendulum friction is extremely small while the beam-motion friction is small), (ii) determining the exponentially-damped oscillating modes of the lightly damped linear model which persist the longest and (iii) identifying the undamped normal mode that most closely approximates this persisting damped mode. It was found that the undamped mode corresponding to the persisting damped mode would have a frequency between the frequencies of the two pendula (oscillating independently from fixed pivots) and a mode shape with the pendula moving in opposition to each other. Korteweg studies showed that the actual nonlinear system's motion would be approximately like a modal motion of a related dissipationless linear system having similar inertial and stiffness properties; and that relative friction magnitudes would determine which mode would be the approximating one [36].

Following the path of Korteweg Senator [36] developed a five degrees of freedom model shown in Fig. 14. The aim of his study was to develop simple intuitive approximate theory that would explain the observed clocks' synchronizations. The developed theory considers the essential nonlinearities and discontinuities of the system, i.e., the impulsive acting of the escapements; allows consideration of non-identical clocks; and explicitly includes the suspended clock-case feature of Huygens' setup.

In addition to forming and analyzing the related dissipationless and damped-linear systems having the same inertial/stiffness/(damping) properties as the original nonlinear system, other related systems are also formed and analyzed. These include the related dissipationless nonlinear systems having the same inertial/stiffness/escapement properties as the original systems, and the related constrained single-degree-of-freedom nonlinear systems formed from the original systems by adding judiciously chosen rigid, massless, frictionless linear constraints. When the generalized constraining (reaction) forces/impulses of these systems are small, the necessarily proportional steady-state motions of these constrained systems are expected to accurately approximate the steady-state motions of the original intractable nonlinear systems.

Senator's approach is based on three main simplifications. One simplification used is to ignore all large amplitude pendula' oscillations, so the angles between the pendula and their vertical equilibrium positions and the rates of change of these angles are assumed to always remain small. The second simplification is to linearize all dampers (friction based dissipative elements). This linear friction simplification captures two essential features of the actual friction in the Huygens experiment, i.e., that at intermediate and high velocity amplitudes, friction forces increase as velocity magnitude increases, and, for suitably small friction parameter magnitudes, that cyclic energy dissipated is small in comparison to the energy that is cyclically converted between potential and kinetic forms. The third simplification is connected with the modeling of the nonlinear energy resupply features of the escapement mechanism. Huygens' pendulum clocks used a almost-400-year-old verge-and crown-wheel escapement design (see Fig. 7 and Section 2.2.1) for which Senator used the constant-impulse-magnitude escapement model of Andronov et al. [50]. For this model, at two opposite points in the pendulum displacement cycle, a crown-wheel tooth hits a pallet (the escapement fires), and a constant magnitude impulse is applied between a rigid body having the effective inertia of the pendulum at the pitch radius of the impact, and a rigid body having the effective inertia of the driving train at the pitch radius of the impact.

The sketch of Senator's model is shown in Fig. 14. It shows two coupled clocks, sliding beam and the suspended clock's cases which form the five-degree-of-freedom model. The coordinate vector is defined as  $x = \{x_1, u_2, y, u_4, x_5\}$ , where the  $x_i$ , ( $i = 1, 5$ ), denote the horizontal relative displacements of the pendulum mass centers measured from the center lines of the pivoted clock cases,  $u_j$ , ( $j = 2, 4$ ), denote the horizontal relative displacements of the clock-case mass centers measured from vertical lines drawn on the support mass, and  $y$  denotes the absolute horizontal displacement of the support mass (this coordinate ordering reflects the connectivity of the rigid bodies that comprise the model). The dissipation is modeled by two viscous dampers, both exerting horizontal retarding forces on the pendulum at its mass center. The friction in the pivot is modeled by a viscous damping coefficient,  $c_{pivot}$ , which multiplies the relative component of horizontal velocity  $\dot{x}$ , while the air resistance is modeled by a viscous damping coefficient,  $c_{air}$ , which multiplies the absolute component of horizontal velocity, which for this model is the same as the relative component. The escapement mechanism acts whenever relative displacement  $x$ , is zero and relative velocity  $\dot{x}_i$  is non-zero. At each of these instants the escapement fires, imparting a horizontal impulse of fixed magnitude  $I_i$  ( $i = 1, 5$ ), located between the pendulum and the clock-case at the level of the mass center of the pendulum, acting on the pendulum in the direction of its relative velocity  $\dot{x}_i$ .

Twelve parameters characterize the geometric and dynamical properties of both clock's pendulum, i.e.,  $m_i$  the mass of the  $i$ -th pendulum,  $e_i$  the  $i$ -th pendulum's length (the distance from its pivot to its mass center),  $\alpha_i$  the square of the ratio of the pendulum's radius of inertia about its mass center to its length (inertial effects of the connected linkage, gear pair, and verge are included by increasing  $\alpha$  so that total kinetic energy still equals  $\frac{1}{2}m_i(1 + \alpha_i)\dot{x}_i^2$ ),  $c_{pivot\ i}$ ,  $c_{air\ i}$ , as damping coefficients, and  $I_i$  escapement mechanism parameters. Twelve additional parameters describe this pivoted-case model, i.e., the individual clock-case masses  $m_j$ , the individual clock-case lengths  $e_j$ , the individual squares of ratios of radii of gyration about mass centers to lengths,  $\alpha_j$ , the individual pivot damping coefficient  $c_{pivot\ j}$ ; the individual air damping constants,  $c_{air\ j}$ , and the individual offsets of the pendulum pivots (the downward distances along the clock-case centerlines from the clock-case pivots to the pivots of the pendula)  $o_j$ , ( $j = 2, 4$ ). Finally, the beam is characterized by three support parameters,  $2m_{sup}$ ,  $2c_{sup}$ , and  $2k_{sup}$ . The resultant gravitational force on the  $i$ -th pendulum (or  $j$ -th clock's case) has magnitude  $m_i g$ , and acts downward through the mass center of the pendulum.

For the model of Fig. 14 one can derive a set of 5 linear second order differential equations (for details see [36]). After a complicated procedure of the parameters identification it was found [36] that the developed theory allows finding the regions in parameter space for which one can predict, with high certainty, whether or not synchronization can occur.

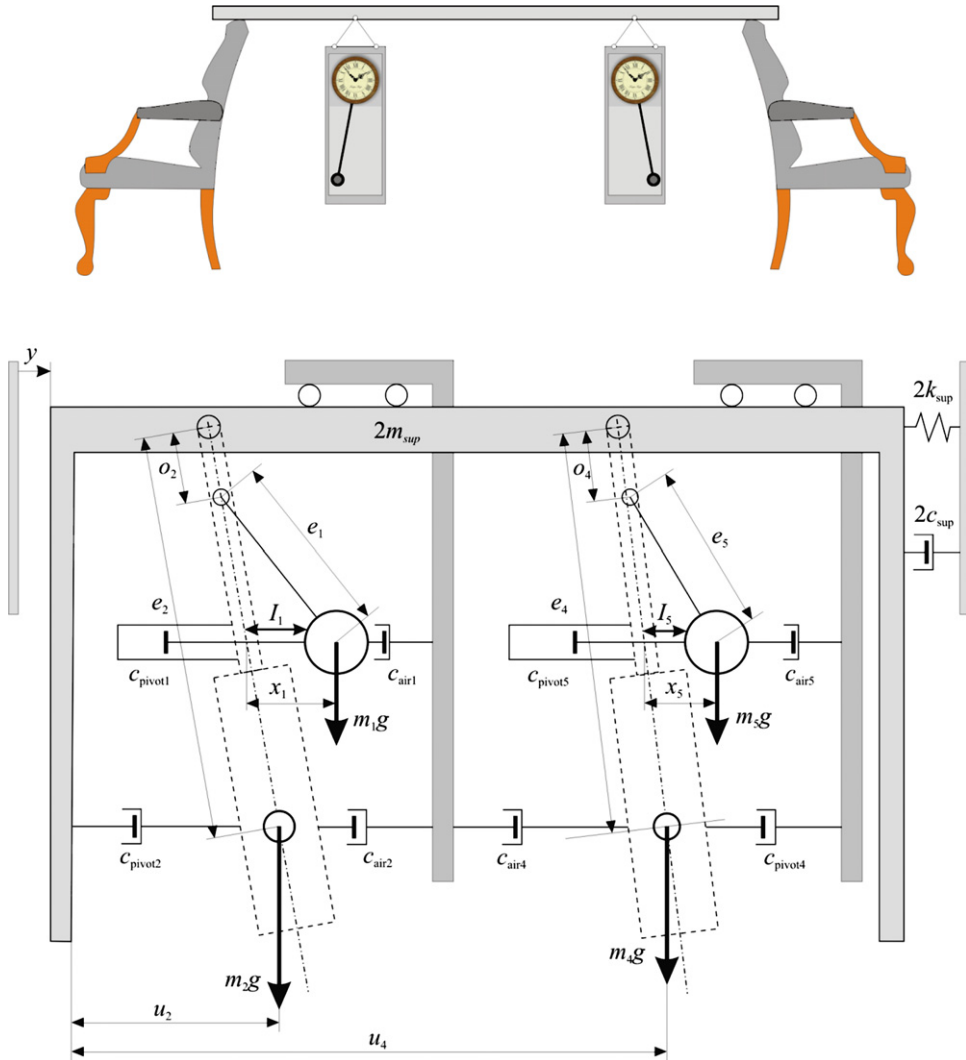


Fig. 14. Senator's model of the Huygens experiment (after [36]).

When synchronization is predicted (it is predicted that, as Huygens observed, the two clocks will synchronize with the pendula moving nearly in opposite phase), the theory allows determining the basic characteristics (approximate frequency, amplitudes, and relative phases) of the synchronized motions.

### 3.3. Model of two double spherical pendula

Examining the structure of the Huygens' setup (Fig. 1) one can expect the spherical motion of both clock cases (allowed by the method the clocks were hung from the beam) and the pendula so before describing the model used in our studies let us introduce the general model based on the coupled double spherical pendula. The system consists of a beam of mass  $M$ , moving along axis  $x$  and two spherical double pendula as shown in Fig. 15.

Each double spherical pendulum consists of: (i) upper spherical physical pendulum: two masses  $m_{1i}$  and  $m_{3i}$  mounted on a light rod, at distances  $l_{1i}$  and  $l_{3i}$  from the point of attachment, (ii) lower spherical pendulum length  $l_{2i}$  and mass  $m_{2i}$ . In this model upper pendula represent clock cases, lower pendula clocks' pendula. The mass  $m_{1i}$  and distances  $l_{1i}$  and  $l_{3i}$  determine the position of the center mass and inertial momentum of the clock. The oscillations of the pendula are damped by the linear dampers  $c_{\varphi 1i}$ ,  $c_{v 1i}$ ,  $c_{\varphi 2i}$  and  $c_{v 2i}$  (not shown in Fig. 15).

The assumed structure of the upper pendulum allows the flexible selection of the value of its mass  $m_{ui}$ , the position of the center of mass  $l_{ui}$  and inertial momentum  $B_{ui}$  (in relation to an axis perpendicular to the rod of the pendulum and passing through the center of its mass).

In the assumed one-dimensional case (Fig. 16) one has:  $m_{ui} = m_{1i} + m_{3i}$ ,  $m_{ui}l_{ui} = m_{1i}l_{1i} + m_{3i}l_{3i}$  and  $B_{ui} = m_{1i}(l_{ui} - l_{1i})^2 + m_{3i}(l_{ui} - l_{3i})^2$ . These equations allow for the estimation of the appointment  $m_{1i}$ ,  $m_{3i}$  and  $l_{3i}$  for given  $m_{ui}$ ,  $l_{ui}$  and  $B_{ui}$ .

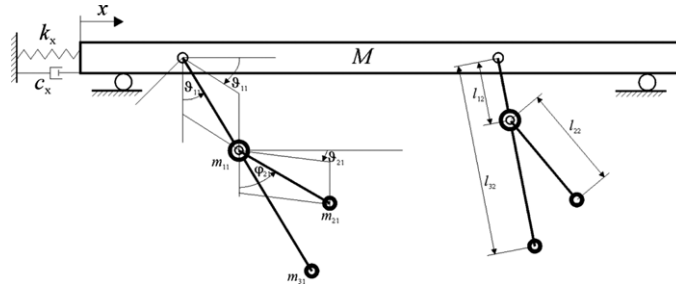


Fig. 15. Huygens' experiment modeled with two coupled double spherical pendula.

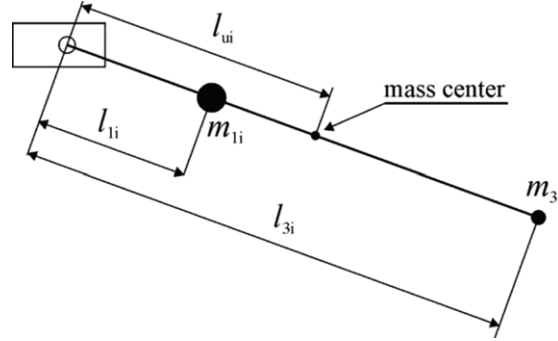


Fig. 16. Geometry of the double-pendulum.

The fourth parameter characterizing the upper pendulum, the distance  $l_{1i}$ , can be freely selected—for example, in such a way to have mass  $m_1$  in the suspension point of the lower pendulum.

The kinetic energy  $T$  and the potential energy  $V$  of the system are given respectively as

$$E = 0.5M\dot{x}^2 + \sum_{i=1}^2 (0.5m_1(\dot{x}_1^2 + \dot{y}_1^2 + \dot{z}_1^2) + 0.5m_3(\dot{x}_3^2 + \dot{y}_3^2 + \dot{z}_3^2) + 0.5m_2(\dot{x}_2^2 + \dot{y}_2^2 + \dot{z}_2^2))$$

and

$$V = \sum_{i=1}^2 ((m_{1i} + m_{2i})gl_{1i}(1 - \cos \varphi_{1i}) + m_{2i}gl_{2i}(1 - \cos \varphi_{2i}) + m_{3i}gl_{3i}(1 - \cos \varphi_{1i})),$$

where the independent coordinates:  $x, \varphi_{1i}, \vartheta_{1i}, \varphi_{2i}, \vartheta_{2i}, i = 1, \dots, 2$  are defined as shown in Fig. 17.

The relation between the coordinates of material points  $m_{1i}, m_{3i}$  and  $m_{2i}$  and independent coordinates is as follows:

$$\begin{aligned} x_{1i} &= x + l_{1i} \sin \varphi_{1i} \cos \vartheta_{1i} \\ y_{1i} &= l_{1i} \sin \varphi_{1i} \sin \vartheta_{1i} \\ z_{1i} &= l_{1i} \cos \varphi_{1i} \\ x_{3i} &= x + l_{3i} \sin \varphi_{1i} \cos \vartheta_{1i} \\ y_{3i} &= l_{3i} \sin \varphi_{1i} \sin \vartheta_{1i} \\ z_{3i} &= l_{3i} \cos \varphi_{1i} \\ x_{2i} &= x + l_{1i} \sin \varphi_{1i} \cos \vartheta_{1i} + l_{2i} \sin \varphi_{2i} \cos \vartheta_{2i} \\ y_{2i} &= l_{1i} \sin \varphi_{1i} \sin \vartheta_{1i} + l_{2i} \sin \varphi_{2i} \sin \vartheta_{2i} \\ z_{2i} &= l_{1i} \cos \varphi_{1i} + l_{2i} \cos \varphi_{2i}. \end{aligned}$$

Using the Lagrange equations:

$$\begin{aligned} l \frac{d}{dt} \left( \frac{\partial E}{\partial \dot{x}} \right) - \frac{\partial E}{\partial x} + \frac{\partial V}{\partial x} &= -c_x \dot{x} - k_x x \\ \frac{d}{dt} \left( \frac{\partial E}{\partial \dot{\varphi}_{1i}} \right) - \frac{\partial E}{\partial \varphi_{1i}} + \frac{\partial V}{\partial \varphi_{1i}} &= -c_{\varphi 1i} \dot{\varphi}_{1i} \\ \frac{d}{dt} \left( \frac{\partial E}{\partial \dot{\vartheta}_{1i}} \right) - \frac{\partial E}{\partial \vartheta_{1i}} + \frac{\partial V}{\partial \vartheta_{1i}} &= -c_{\vartheta 1i} \dot{\vartheta}_{1i} \\ \frac{d}{dt} \left( \frac{\partial E}{\partial \dot{\varphi}_{2i}} \right) - \frac{\partial E}{\partial \varphi_{2i}} + \frac{\partial V}{\partial \varphi_{2i}} &= -c_{\varphi 2i} \dot{\varphi}_{2i} + M_{Di} \quad i = 1, \dots, 2 \end{aligned}$$

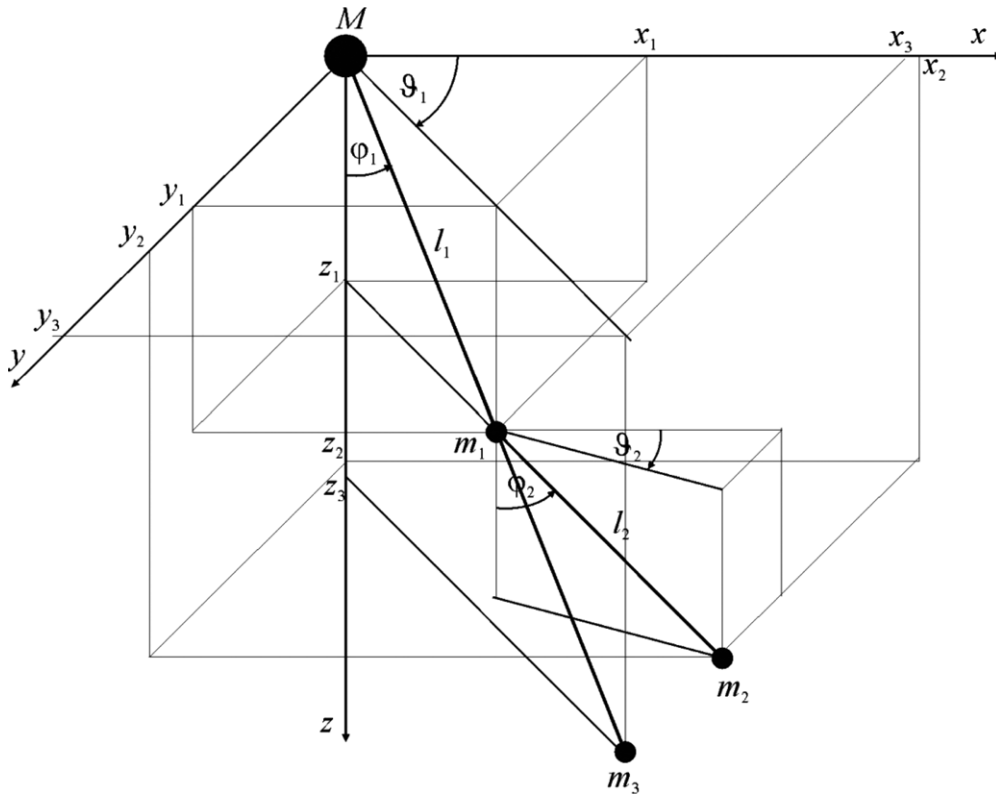


Fig. 17. Coordinates describing the oscillations of the double pendulum.

$$\frac{d}{dt} \left( \frac{\partial E}{\partial \dot{\vartheta}_{2i}} \right) - \frac{\partial E}{\partial \vartheta_{2i}} + \frac{\partial V}{\partial \vartheta_{2i}} = -c_{\vartheta_{1i}} \dot{\vartheta}_{1i}$$

one can derive the equations of motion in the following form

$$\sum_{i=1}^2 \left( \begin{array}{l} [m_{1i} + m_{2i}][l_{1i}\ddot{\varphi}_{1i} \cos \varphi_{1i} \cos \vartheta_{1i} - l_{1i}\dot{\varphi}_{1i}^2 \sin \varphi_{1i} \cos \vartheta_{1i} - 2l_{1i}\dot{\varphi}_{1i}\dot{\vartheta}_{1i} \cos \varphi_{1i} \sin \vartheta_{1i} \\ - l_{1i}\dot{\vartheta}_{1i} \sin \varphi_{1i} \sin \vartheta_{1i} - l_{1i}\dot{\vartheta}_{1i}^2 \sin \varphi_{1i} \cos \vartheta_{1i}] \\ + m_{3i}[l_{3i}\ddot{\varphi}_{1i} \cos \varphi_{1i} \cos \vartheta_{1i} - l_{3i}\dot{\varphi}_{1i}^2 \sin \varphi_{1i} \cos \vartheta_{1i} - 2l_{3i}\dot{\varphi}_{1i}\dot{\vartheta}_{1i} \cos \varphi_{1i} \sin \vartheta_{1i} \\ - l_{3i}\dot{\vartheta}_{1i} \sin \varphi_{1i} \sin \vartheta_{1i} - l_{3i}\dot{\vartheta}_{1i}^2 \sin \varphi_{1i} \cos \vartheta_{1i}] \\ + m_{2i}[l_{2i}\ddot{\varphi}_{2i} \cos \varphi_{2i} \cos \vartheta_{2i} - l_{2i}\dot{\varphi}_{2i}^2 \sin \varphi_{2i} \cos \vartheta_{2i} - 2l_{2i}\dot{\varphi}_{2i}\dot{\vartheta}_{2i} \cos \varphi_{2i} \sin \vartheta_{2i} \\ - l_{2i}\dot{\vartheta}_{2i} \sin \varphi_{2i} \sin \vartheta_{2i} - l_{2i}\dot{\vartheta}_{2i}^2 \sin \varphi_{2i} \cos \vartheta_{2i}] \end{array} \right) + \left[ M + \sum_{i=1}^2 (m_{1i} + m_{2i} + m_{3i}) \right] \ddot{x} = -c_x \dot{x} - k_x x \quad (22)$$

$$\begin{aligned} & [m_{1i} + m_{2i}][l_{1i}^2\ddot{\varphi}_{1i} + \ddot{x}l_{1i} \cos \varphi_{1i} \cos \vartheta_{1i} - l_{1i}^2\dot{\vartheta}_{1i}^2 \sin \varphi_{1i} \cos \varphi_{1i}] \\ & + m_{3i}[l_{3i}^2\ddot{\varphi}_{1i} + \ddot{x}l_{3i} \cos \varphi_{1i} \cos \vartheta_{1i} - l_{3i}^2\dot{\vartheta}_{1i}^2 \sin \varphi_{1i} \cos \varphi_{1i}] \\ & + m_{2i}l_{1i}l_{2i}[\ddot{\varphi}_{2i} \cos \varphi_{1i} \cos \varphi_{2i} \cos(\vartheta_{2i} - \vartheta_{1i}) - (\dot{\vartheta}_{1i}\dot{\vartheta}_{2i} + \dot{\varphi}_{2i}^2) \cos \varphi_{1i} \sin \varphi_{2i} \cos(\vartheta_{2i} - \vartheta_{1i}) \\ & + \dot{\varphi}_{2i}(\dot{\vartheta}_{1i} - \dot{\vartheta}_{2i}) \cos \varphi_{1i} \cos \varphi_{2i} \sin(\vartheta_{2i} - \vartheta_{1i}) + \ddot{\varphi}_{2i} \sin \varphi_{1i} \sin \varphi_{2i} + \dot{\varphi}_{2i}^2 \sin \varphi_{1i} \cos \varphi_{2i}] \\ & + [m_{1i} + m_{2i}]gl_{1i} \sin \varphi_{1i} + m_{3i}gl_{3i} \sin \varphi_{1i} = -c_{\varphi_{1i}}\dot{\varphi}_{1i} \end{aligned} \quad (23)$$

$$\begin{aligned} & [m_{1i} + m_{2i}][l_{1i}^2\ddot{\vartheta}_{1i} \sin^2 \varphi_{1i} + 2l_{1i}^2\dot{\vartheta}_{1i}\dot{\varphi}_{1i} \sin \varphi_{1i} \cos \varphi_{1i} - \ddot{x}l_{1i} \sin \varphi_{1i} \sin \vartheta_{1i}] \\ & + m_{3i}[l_{3i}^2\ddot{\vartheta}_{1i} \sin^2 \varphi_{1i} + 2l_{3i}^2\dot{\vartheta}_{1i}\dot{\varphi}_{1i} \sin \varphi_{1i} \cos \varphi_{1i} - \ddot{x}l_{3i} \sin \varphi_{1i} \sin \vartheta_{1i}] \\ & + m_{2i}l_{1i}l_{2i}[\ddot{\vartheta}_{2i} \sin \varphi_{1i} \sin \varphi_{2i} \cos(\vartheta_{2i} - \vartheta_{1i}) + \dot{\varphi}_{1i}\dot{\vartheta}_{2i} \cos \varphi_{1i} \sin \varphi_{2i} \cos(\vartheta_{2i} - \vartheta_{1i}) \\ & + \dot{\varphi}_{2i}\dot{\vartheta}_{2i} \sin \varphi_{1i} \cos \varphi_{2i} \cos(\vartheta_{2i} - \vartheta_{1i}) + \dot{\vartheta}_{2i}^2 \sin \varphi_{1i} \sin \varphi_{2i} \sin(\vartheta_{2i} - \vartheta_{1i}) \\ & - \dot{\varphi}_{1i}\dot{\varphi}_{2i} \cos \varphi_{1i} \cos \varphi_{2i} \sin(\vartheta_{2i} - \vartheta_{1i})] = -c_{\vartheta_{1i}}\dot{\vartheta}_{1i} \end{aligned} \quad (24)$$

$$m_{2i}[l_{2i}^2\ddot{\vartheta}_{2i} + \ddot{x}l_{2i} \cos \varphi_{2i} \cos \vartheta_{2i} - l_{2i}^2\dot{\vartheta}_{2i}^2 \sin \varphi_{2i} \cos \varphi_{2i}]$$

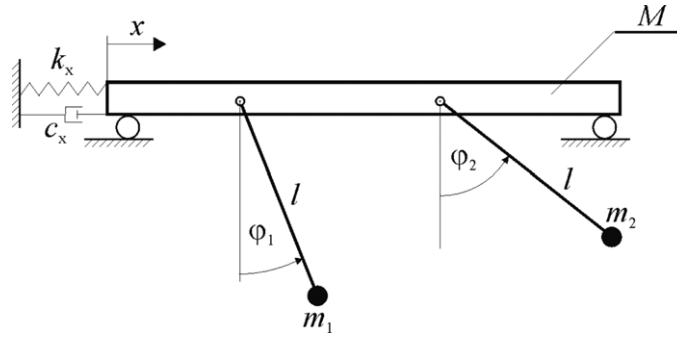


Fig. 18. The model of the system – two pendulum clocks are mounted to the beam which can move horizontally.

$$\begin{aligned}
 & + m_{2i} l_{1i} l_{2i} [\ddot{\varphi}_{1i} \cos \varphi_{1i} \cos \varphi_{2i} \cos(\vartheta_{2i} - \vartheta_{1i}) - (\dot{\vartheta}_{1i} \dot{\vartheta}_{2i} + \dot{\varphi}_{1i}^2) \cos \varphi_{1i} \cos \varphi_{2i} \cos(\vartheta_{2i} - \vartheta_{1i}) \\
 & + \dot{\varphi}_{1i} (\dot{\vartheta}_{1i} - \dot{\vartheta}_{2i}) \cos \varphi_{1i} \cos \varphi_{2i} \sin(\vartheta_{2i} - \vartheta_{1i}) + \ddot{\varphi}_{1i} \sin \varphi_{1i} \sin \varphi_{2i} + \dot{\varphi}_{1i}^2 \cos \varphi_{1i} \sin \varphi_{2i}] \\
 & + m_{2i} g l_{2i} \sin \varphi_{2i} = -c_{\varphi 2i} \dot{\varphi}_{2i} + M_{Di} \quad (25) \\
 & m_{2i} [l_{2i}^2 \ddot{\vartheta}_{2i} \sin^2 \varphi_{2i} + 2l_{2i}^2 \dot{\vartheta}_{2i} \dot{\varphi}_{2i} \sin \varphi_{2i} \cos \varphi_{2i} - \ddot{x} l_{2i} \sin \varphi_{2i} \sin \vartheta_{2i}] \\
 & + m_{2i} l_{1i} l_{2i} [\ddot{\vartheta}_{1i} \sin \varphi_{1i} \sin \varphi_{2i} \cos(\vartheta_{2i} - \vartheta_{1i}) + \dot{\varphi}_{1i} \dot{\vartheta}_{1i} \cos \varphi_{1i} \sin \varphi_{2i} \cos(\vartheta_{2i} - \vartheta_{1i}) \\
 & + \dot{\varphi}_{2i} \dot{\vartheta}_{1i} \sin \varphi_{1i} \cos \varphi_{2i} \cos(\vartheta_{2i} - \vartheta_{1i}) + \dot{\vartheta}_{1i}^2 \sin \varphi_{1i} \sin \varphi_{2i} \sin(\vartheta_{2i} - \vartheta_{1i}) \\
 & + \dot{\varphi}_{1i} \dot{\varphi}_{2i} \cos \varphi_{1i} \cos \varphi_{2i} \sin(\vartheta_{2i} - \vartheta_{1i})] = -c_{\vartheta 2i} \dot{\vartheta}_{2i} \quad (26)
 \end{aligned}$$

where  $i = 1, 2$ .

Eqs. (22)–(25) represent the most general dynamical model of Huygens' experiment. Our numerical studies show that this model cannot be used in the explanation of the clocks' synchronization for the reason that the spherical motion of the clocks' cases forced the spherical oscillations of the clock's pendula and perturbs the action of the escapement mechanisms (designed to work for the pendulum oscillations which are close to planar). Additionally the spherical motion of the clock's cases can be practically eliminated by the appropriate balancing of the case (possibly this was the reason why Huygens added additional weights to the clock's cases – Fig. 2). Spherical motion has been also eliminated in our experiments described in Section 4.1.

### 3.4. Three degrees of freedom discontinuous model

By clamping the clocks cases to the beam and allowing only planar oscillations of the lower pendula one can reduce the model described in Section 3.3 to three degrees of freedom model shown in Fig. 18. It consists of the rigid beam and two pendulum clocks suspended on it. The beam of mass  $M$  can move in a horizontal direction, its movement is described by coordinate  $x$ . The mass of the beam is connected to the refuge of a linear spring and linear damper  $k_x$  and  $c_x$ . The clocks' pendulum consists of the light beam of the length  $l$  and mass mounted at its end. We consider two cases (i) the pendula with the same length  $l$  but different masses  $m_1$  and  $m_2$ , and (ii) the pendula with the same mass and different length. The same length of both pendula guarantees that the clocks are accurate, i.e., both show the same time. The motion of the pendula is described by angles  $\varphi_1$  and  $\varphi_2$  and is damped by dampers (not shown in Fig. 18) with damping coefficients  $c_{\varphi 1}$  and  $c_{\varphi 2}$ . The pendula are driven by the escapement mechanism described in details in Section 2.2 [48,49,47,60,43,102]. Notice that when the angular displacements of swinging pendula are less than certain angle  $\gamma_N$ , the escapement mechanisms generate the constant moments  $M_{N1}$  and  $M_{N2}$ . We consider two cases, i.e., (i) the damping coefficients  $c_{\varphi 1,2}$  and moments  $M_{N1,2}$  are proportional to the pendula' masses  $m_{1,2}$ , (ii) the damping coefficients  $c_{\varphi 1,2}$  and moments  $M_{N1,2}$  are equal and independent of pendula' masses  $m_{1,2}$ . The proportionality in (i) causes that in the lack of forcing (when the clock is not wound) the oscillations of both pendula decay with the same speed. In both cases, when the beam is fixed, the pendula oscillate with the same amplitude and the movement of the beam may change both the period and the amplitude of pendula oscillations.

This mechanism acts in two successive steps i.e., the first step is followed by the second one and the second one by the first one. In the first step if  $0 < \varphi_i < \gamma_N$  ( $i = 1, 2$ ) then  $M_{Di} = M_{Ni}$  and when  $\varphi_i < 0$  then  $M_{Di} = 0$ . For the second stage one has for  $-\gamma_N < \varphi_i < 0$   $M_{Di} = -M_{Ni}$  and for  $\varphi_i > 0$   $M_{Di} = 0$ . The energy supplied by the escapement mechanic balance the energy dissipated due to the damping. The parameters of this mechanics have been chosen in the way that for the beam  $M$  at rest both pendula perform oscillations with the same amplitude. Typically the pendulum clocks oscillate with amplitude smaller than  $2\pi/36$  and for clocks with long pendula like marine clocks this amplitude is even smaller [48].

The equations of motion are as follow:

$$m_i l_i^2 \ddot{\varphi}_i + m_i \ddot{x} \cos \varphi_i + c_{\varphi i} \dot{\varphi}_i + m_i g l_i \sin \varphi_i = M_{Di}, \quad (27)$$

$$\left(M + \sum_{i=1}^2 m_i\right) \ddot{x} + c_x \dot{x} + k_x x + \sum_{i=1}^2 m_i l_i (\ddot{\varphi}_i \cos \varphi_i - \dot{\varphi}_i^2 \sin \varphi_i) = 0, \quad (28)$$

$i = 1, 2$ . Notice that Eqs. (27) and (28) can be derived from Eqs. (22)–(26) by setting  $l_{1i} = 0, l_{3i} = 0, x_{1i} = x, y_{1i} = 0, z_{1i} = 0, x_{3i} = x, y_{3i} = 0, z_{3i} = 0, x_{2i} = x + l_{2i} \sin \varphi_{2i}, y_{2i} = 0, z_{2i} = l_{2i} \cos \varphi_{2i}$  and allowing lower pendula to oscillate in  $x$ - $z$  plane. Eqs. (27) and (28) describe the dynamical system which performs the self-excited oscillations [50].

The clocks are designed in such a way that the pendula perform periodic motion with a period  $2\pi/\alpha$  where  $\alpha$  is constant. The escapement mechanism provides the necessary amount of energy to compensate the dissipation and makes the pendulum motion periodic. Under these assumptions in the state of phase or antiphase synchronization the motion of the clock's pendula has be approximated by:

$$\varphi_i = \Phi_i \sin(\alpha t + \beta_i), \quad (29)$$

and

$$\begin{aligned} \dot{\varphi}_i &= \alpha \Phi_i \cos(\alpha t + \beta_i), \\ \ddot{\varphi}_i &= -\alpha^2 \Phi_i \sin(\alpha t + \beta_i), \end{aligned} \quad (30)$$

where  $\Phi_i$  are constant amplitudes of pendula's oscillations.

Our numerical simulations (e.g. Fig. 12) show that the continuous solution given by Eq. (29) is a good approximation of the pendula' oscillations calculated from discontinuous equations (27) and (28) in the case of both identical and nonidentical clocks. Substituting Eqs. (29) and (30) into Eq. (28) and assuming that the pendula have the same length ( $l_1 = l_2 = l$ ) one gets:

$$\left(M + \sum_{i=1}^2 m_i\right) \ddot{x} + c_x \dot{x} + k_x x = \sum_{i=1}^2 (m_i l \alpha^2 \Phi_i \sin(\alpha t + \beta_i) + m_i l \alpha^2 \Phi_i^3 \cos^2(\alpha t + \beta_i) \sin(\alpha t + \beta_i)). \quad (31)$$

Considering  $\cos^2 \alpha \sin \alpha = 0.25 \sin \alpha + 0.75 \sin 3\alpha$ , and denoting

$$U = M + \sum_{i=1}^2 m_i, \quad F_{1i} = m_i l \alpha^2 (\Phi_i + 0.25 \Phi_i^3), \quad F_{3i} = 0.75 m_i l \alpha^2 \Phi_i^3, \quad (32)$$

we have

$$U \ddot{x} + c_x \dot{x} + k_x x = \sum_{i=1}^2 (F_{1i} \sin(\alpha t + \beta_i) + F_{3i} \sin(3\alpha t + 3\beta_i)). \quad (33)$$

Assuming the small value of the damping coefficient  $c_x$  the solution of Eq. (33) can be rewritten in the following form

$$x = \sum_{i=1}^2 (X_{1i} \sin(\alpha t + \beta_i) + X_{3i} \sin(3\alpha t + 3\beta_i)), \quad (34)$$

where

$$\begin{aligned} X_{1i} &= \frac{F_{1i}}{k_x - \alpha^2 U} = \frac{m_i l \alpha^2 (\Phi_i + 0.25 \Phi_i^3)}{k_x - \alpha^2 U}, \\ X_{3i} &= \frac{F_{3i}}{k_x - 9\alpha^2 U} = \frac{0.25 m_i l \alpha^2 \Phi_i^3}{k_x - 9\alpha^2 U}. \end{aligned} \quad (35)$$

Eq. (34) implies the following acceleration of the beam  $M$ :

$$\ddot{x} = \sum_{i=1}^2 (A_{1i} \sin(\alpha t + \beta_i) + A_{3i} \sin(3\alpha t + 3\beta_i)), \quad (36)$$

where

$$\begin{aligned} A_{1i} &= -\frac{m_i l \alpha^4 (\Phi_i + 0.25 \Phi_i^3)}{k_x - \alpha^2 U}, \\ A_{3i} &= -\frac{0.25 m_i l \alpha^4 \Phi_i^3}{k_x - 9\alpha^2 U}. \end{aligned} \quad (37)$$

Notice that Eq. (36) consists of the first and third harmonic components only.

### 3.4.1. Energy balance of the clocks' pendula

Multiplication of both sides of Eq. (27) by the angular velocity of the  $i$ -th pendulum gives:

$$m_i l^2 \ddot{\varphi}_i \dot{\varphi}_i + m_i g l \dot{\varphi}_i \sin \varphi_i = M_{Di} \dot{\varphi}_i - c_{\varphi i} \dot{\varphi}_i^2 - m_i \ddot{x} l \cos \varphi_i \dot{\varphi}_i. \quad (38)$$

In the case of the periodic motion of the pendula after integration equation (38) gives the energy balance of the  $i$ -th pendulum:

$$\int_0^T m_i l^2 \ddot{\varphi}_i \dot{\varphi}_i dt + \int_0^T m_i g l \dot{\varphi}_i \sin \varphi_i dt = \int_0^T M_{Di} \dot{\varphi}_i dt - \int_0^T c_{\varphi i} \dot{\varphi}_i^2 dt - \int_0^T m_i \ddot{x} l \cos \varphi_i \dot{\varphi}_i dt. \quad (39)$$

Left hand side of Eq. (39) represents the decrease of the total energy of the  $i$ -th pendulum. In the case of the periodic behavior of system (27) and (28) this decrease is equal to zero, so

$$\int_0^T m_i l^2 \ddot{\varphi}_i \dot{\varphi}_i dt + \int_0^T m_i g l \dot{\varphi}_i \sin \varphi_i dt = 0. \quad (40)$$

The work done by the escapement mechanism during tone period of pendulum's oscillations can be expressed as

$$W_i^{DRIVE} = \int_0^T M_{Di} \dot{\varphi}_i dt = 2 \int_0^{\gamma_N} M_{Ni} d\varphi_i = 2M_{Ni} \gamma_N. \quad (41)$$

We assume that the amplitudes of the pendula  $\varphi_{1,2}$  are larger than  $\gamma_N$ . In such a case  $W_{DRIVE}$  does not on the pendula's displacement  $\varphi_{1,2}$  and velocity  $\dot{\varphi}_i$ . The energy dissipated in the damper is given by

$$W_i^{DAMP} = \int_0^T c_{\varphi i} \dot{\varphi}_i^2 dt = \int_0^T c_{\varphi i} \alpha^2 \Phi_i^2 \cos^2(\alpha t + \beta_i) dt = \pi \alpha c_{\varphi i} \Phi_i^2. \quad (42)$$

(In the integration of Eq. (42) the relation  $\int_0^T \cos \alpha t \cos \alpha t dt = 0.5T = \frac{\pi}{\alpha}$  has been used).

The last component of Eq. (39) represents the energy transferred from the  $i$ -th pendulum to the beam  $M$  (the pendulum loses part of its energy to force the beam to oscillate), so we have:

$$W_i^{SYN} = \int_0^T m_i \ddot{x} l \cos \varphi_i \dot{\varphi}_i dt. \quad (43)$$

Substituting Eqs. (41)–(43) into Eq. (39) one obtains energy balance for the  $i$ -th pendulum.

$$\begin{aligned} W_1^{DRIVE} &= W_1^{DAMP} + W_1^{SYN}, \\ W_2^{DRIVE} &= W_2^{DAMP} + W_2^{SYN}. \end{aligned} \quad (44)$$

Notice that the energies  $W_{1,2}^{SYN}$  are responsible for the clocks' synchronization.

### 3.4.2. Energy balance of the beam and whole system (26) and (27)

Multiplying equation of the beam motion (28) by beam velocity  $\dot{x}$  one gets:

$$\left( M + \sum_{i=1}^2 m_i \right) \ddot{x} + c_x \dot{x}^2 + k_x x \dot{x} + \left( \sum_{i=1}^2 m_i l (\ddot{\varphi}_i \cos \varphi_i - \dot{\varphi}_i^2 \sin \varphi_i) \right) \dot{x} = 0. \quad (45)$$

Integrating Eq. (45) over the period of oscillations we obtain the following energy balance:

$$\int_0^T \left( M + \sum_{i=1}^2 m_i \right) \ddot{x} \dot{x} dt + \int_0^T c_x \dot{x}^2 dt = - \int_0^T \left( \sum_{i=1}^2 m_i l (\ddot{\varphi}_i \cos \varphi_i - \dot{\varphi}_i^2 \sin \varphi_i) \right) \dot{x} dt - \int_0^T c_x \dot{x}^2 dt. \quad (46)$$

Left hand side of Eq. (46) represents the increase of the total energy of the beam which for the periodic oscillations is equal to zero:

$$\int_0^T \left( M + \sum_{i=1}^2 m_i \right) \ddot{x} \dot{x} dt + \int_0^T c_x \dot{x}^2 dt = 0. \quad (47)$$

The first component on the right-hand side of Eq. (46) represents the work performed by the horizontal component of the force with which the pendula act on the beam causing its motion:

$$W_{beam}^{DRIVE} = - \int_0^T \left( \sum_{i=1}^2 m_i l (\ddot{\varphi}_i \cos \varphi_i - \dot{\varphi}_i^2 \sin \varphi_i) \right) \dot{x} dt. \quad (48)$$

The second component on the right hand side of Eq. (46) represents the energy dissipated by the damper  $c_x$ :

$$W_{beam}^{DAMP} = \int_0^T c_x \dot{x}^2 dt. \quad (49)$$

Substituting Eqs. (47)–(49) into Eq. (46) one gets the energy balance in the following form

$$W_{beam}^{DRIVE} = W_{beam}^{DAMP}. \quad (50)$$

In the case of the periodic oscillations it is possible to prove that

$$W_1^{SYN} + W_2^{SYN} = W_{beam}^{DRIVE}. \quad (51)$$

Assuming  $W_1^{DRIVE} = W_2^{DRIVE}$  and adding Eqs. (44) and (50)

$$2W^{DRIVE} + W_{beam}^{DRIVE} = W_1^{DAMP} + W_2^{DAMP} + W_1^{SYN} + W_2^{SYN} + W_{beam}^{DAMP},$$

or after considering Eq. (51) one obtains

$$2W^{DRIVE} = W_1^{DAMP} + W_2^{DAMP} + W_{beam}^{DAMP}. \quad (52)$$

Eq. (52) represents the energy balance of the whole system (27) and (28).

Now let us consider the properties of Eq. (44) in a few special cases of the pendula synchronization.

(i) *Energy balance during the anti-phase synchronization (identical pendula)*

In the case of the antiphase synchronization of two identical pendula the beam  $M$  is in rest [42,43]. There is no energy transfer between pendula and the beam so Eq. (44) has the form

$$W_i^{DRIVE} = W_i^{DAMP}, \quad (53)$$

( $i = 1, 2$ ). This balance for two clocks' pendula will be numerically illustrated in Section 4.2 (Fig. 25). Substituting Eqs. (41) and (42) into Eq. (53) one gets

$$2M_{Ni}\gamma_N = \pi\alpha c_{\varphi_i} \Phi_i^2 \quad (54)$$

( $i = 1, 2$ ) so one gets the expression

$$\Phi_i = \sqrt{\frac{2M_{Ni}\gamma_N}{\pi\alpha c_{\varphi_i}}}. \quad (55)$$

( $i = 1, 2$ ) for the amplitude of the pendulum's oscillations.

(ii) *Energy balance during the phase synchronization (pendula with different masses)*

In the case of two nonidentical clocks (with different pendula masses) mounted to the beam  $M$  one can observe phase synchronization of the pendula. The beam performs horizontal oscillations and the energy  $W_i^{SYN}$  is not equal to zero. Substituting pendulum's velocity Eq. (30), beam's acceleration Eq. (36) into Eq. (43) and taking into account the simplification  $\cos\varphi_i = 1.0$ , one gets the expression for the energy transferred from  $i$ -th pendulum to the beam:

$$W_i^{SYN} = \int_0^T (m_i l \ddot{x} \cos\varphi_i) \dot{\varphi}_i dt = \int_0^T m_i l \left( \sum_{j=1}^2 (A_{1j} \sin(\alpha t + \beta_j) + A_{3j} \sin(3\alpha t + 3\beta_j)) \right) \alpha \Phi_i \cos(\alpha t + \beta_i) dt. \quad (56)$$

After further calculations one gets:

$$W_i^{SYN} = m_i l \alpha \Phi_i \sum_{j=1}^2 A_{1j} \frac{\pi}{\alpha} (-\cos\beta_j \sin\beta_i + \sin\beta_j \cos\beta_i) = m_i l \alpha \Phi_i \sum_{j=1}^2 A_j \frac{\pi}{\alpha} \sin(\beta_j - \beta_i) \quad (57)$$

and after substitution of Eq. (37):

$$W_i^{SYN} = \frac{-m_i l^2 \alpha^4 \pi \Phi_i}{k_x - \alpha^2 U} \sum_{j=1}^2 m_j (\Phi_j + 0.25 \Phi_j^3) \sin(\beta_j - \beta_i). \quad (58)$$

Setting  $\beta_1 = 0.0$  (one of the phase angles can be arbitrarily chosen) and taking into consideration the following simplification  $\Phi_i + 0.25 \Phi_i^3 \approx \Phi_i$ , Eq. (58) can be rewritten as:

$$\begin{aligned} W_1^{SYN} &= -\frac{m_1 l^2 \alpha^4 \pi \Phi_1}{k_x - \alpha^2 U} m_2 \Phi_2 \sin\beta_2 = W^{SYN}, \\ W_2^{SYN} &= \frac{m_2 l^2 \alpha^4 \pi \Phi_2}{k_x - \alpha^2 U} m_1 \Phi_1 \sin\beta_2 = -W^{SYN}. \end{aligned} \quad (59)$$

Eq. (59) show that both synchronization energies are equal and so the energy balance of both pendula (Eq. (44)) can be written as

$$\begin{aligned} W_1^{DRIVE} &= W_1^{DAMP} + W^{SYN} \\ W_2^{DRIVE} + W_2^{SYN} &= W_2^{DAMP}. \end{aligned} \quad (60)$$

Substituting Eqs. (41) and (42), (59) into Eq. (60) one gets:

$$\begin{aligned} 2M_{N1}\gamma_N &= \pi\alpha c_{\varphi 1}\Phi_1^2 - \frac{m_1 l^2 \alpha^4 \pi \Phi_1}{k_x - \alpha^2 U} m_2 \Phi_2 \sin \beta_2, \\ 2M_{N2}\gamma_N &= \pi\alpha c_{\varphi 2}\Phi_2^2 + \frac{m_2 l^2 \alpha^4 \pi \Phi_2}{k_x - \alpha^2 U} m_1 \Phi_1 \sin \beta_2, \end{aligned} \quad (61)$$

so

$$\sin \beta_2 = \frac{2M_{N2}\gamma_N - \pi\alpha c_{\varphi 2}\Phi_2^2}{\frac{m_2 l^2 \alpha^4 \pi \Phi_2}{k_x - \alpha^2 U} m_1 \Phi_1}. \quad (62)$$

Eqs. (61) and (62) give relation between the pendula's amplitudes  $\Phi_1$  and  $\Phi_2$  and the phase angle  $\beta_2$ . Note, that Eq. (62) does not allow calculations of  $\Phi_1$ ,  $\Phi_2$  and  $\beta_2$  but show that numerically calculated values fill this relation.

(iii) *Energy dissipated by the  $c_x$ -damper*

Energy dissipated by the  $c_x$ -damper during the period of system oscillations is given by

$$W_b^{DAMP} = \int_0^T c_x \dot{x}^2 dt. \quad (63)$$

Assuming the harmonic oscillations of the beam  $M$  which are characterized by the amplitude  $X$ , i.e.:

$$x = X \sin(\alpha t + \psi), \quad \dot{x} = \alpha X \cos(\alpha t + \psi), \quad (64)$$

where  $\psi$  is a phase angle which determines the phase shift of the beam motion in respect of the first pendulum (with phase angle  $\beta_1$ ). Comparing Eqs. (34) and (64), assuming  $\beta_1 = 0$  and taking into consideration only the first harmonic one gets the following formula

$$\vartheta = \arctan \left( \frac{X_{12}}{X_{11} + X_{12} \cos \beta_2} \right).$$

Substituting Eq. (64) into Eq. (63) one gets

$$W_b^{DAMP} = \int_0^T c_x \dot{x}^2 dt = c_x \alpha \pi X^2. \quad (65)$$

(iv) *The case of the small damping of the pendula*

Let us consider the particular case when the damping of the pendula is small, i.e.,  $c_{\varphi i}$  are small, and such is the moment generated by the escapement mechanism. We have

$$\frac{W_1^{DRIVE}}{W^{SYN}} \approx 0.0, \quad \frac{W_2^{DRIVE}}{W^{SYN}} \approx 0.0, \quad \frac{W_1^{DAMP}}{W^{SYN}} \approx 0.0, \quad \frac{W_1^{DAMP}}{W^{SYN}} \approx 0.0. \quad (66)$$

Taking into consideration Eqs. (61) and (66), Eq. (59) has the form

$$\begin{aligned} W_1^{SYN} &= \frac{-m_1 l^2 \alpha^4 \pi \Phi_1}{k_x - \alpha^2 U} m_2 \Phi_2 \sin \beta_2 = 0.0, \\ W_2^{SYN} &= \frac{m_2 l^2 \alpha^4 \pi \Phi_2}{k_x - \alpha^2 U} m_1 \Phi_1 \sin \beta_2 = 0.0. \end{aligned} \quad (67)$$

Eq. (67) are fulfilled in two cases; (i)  $\beta_2 = 0.0^\circ$ , so as  $\beta_1 = 0.0^\circ$  indicates the state of complete synchronization, the pendula behave exactly in the same way and there is no transfer of energy between them, (ii)  $\beta_2 = 180.0^\circ$ , so as  $\beta_1 = 0.0^\circ$  indicates the state of antiphase synchronization.

### 3.5. Three degrees of freedom model with van der Pol's friction

The continuous model of two coupled clocks can be derived from the one described in Section 3.4 when instead of the clocks with pendula driven by discontinuous escapement mechanism, one considers two self-excited pendula with van der Pol type of damping. The mathematical description of such pendula contains the self-excited component  $c_{\varphi vdp} \dot{\varphi}$  and energy-dissipating component  $c_{\varphi vdp} \zeta \dot{\varphi}^2$ . The balance of these components results in the creation of a stable limit cycle.

The equations of motion of the ( $c_{\varphi vdp} < 0$ ) considered system are as follows:

$$\begin{aligned} m_1 l^2 \ddot{\varphi}_1 + m_1 \ddot{x} l \cos \varphi_1 + c_{\varphi vdp} \dot{\varphi}_1 (1 - \zeta \varphi_1^2) + m_1 g l \sin \varphi_1 &= 0 \\ m_2 l^2 \ddot{\varphi}_2 + m_2 \ddot{x} l \cos \varphi_2 + c_{\varphi vdp} \dot{\varphi}_2 (1 - \zeta \varphi_2^2) + m_2 g l \sin \varphi_2 &= 0 \end{aligned} \quad (68)$$

$$\left( M + \sum_{i=1}^2 m_i \right) \ddot{x} + c_x \dot{x} + k_x x + \sum_{i=1}^2 m_i l (\ddot{\varphi}_i \cos \varphi_i - \dot{\varphi}_i^2 \sin \varphi_i) = 0. \quad (69)$$

Eqs. (68) and (69) contrary to the Eqs. (27) and (28) are continuous.

The energy balance of the continuous model (68) and (69) can be analyzed as follows. Multiplying both sides of Eqs. (68) by angular velocity  $\dot{\varphi}_i$  one gets:

$$m_i l^2 \ddot{\varphi}_i \dot{\varphi}_i + m_i g l \dot{\varphi}_i \sin \varphi_i = -c_{\varphi vdp} \dot{\varphi}_i^2 + c_{\varphi vdp} \zeta \dot{\varphi}_i^2 \varphi_i^2 - m_i \ddot{x} l \cos \varphi_i \dot{\varphi}_i, \quad i = 1, 2. \quad (70)$$

In the case of the periodic oscillations with period  $T$  integration of Eq. (69) gives the following energy balance:

$$\int_0^T m_i l^2 \ddot{\varphi}_i \dot{\varphi}_i dt + \int_0^T m_i g l \dot{\varphi}_i \sin \varphi_i dt = - \int_0^T c_{\varphi vdp} \dot{\varphi}_i^2 dt + \int_0^T c_{\varphi vdp} \zeta \dot{\varphi}_i^2 \varphi_i^2 dt - \int_0^T m_i \ddot{x} l \cos \varphi_i \dot{\varphi}_i dt, \quad (71)$$

where  $i = 1, 2$ . Left hand side of Eq. (71) represents the increase of the total energy of  $i$ -th pendulum which in the case of periodic oscillations is equal to zero:

$$\int_0^T m_i l^2 \ddot{\varphi}_i \dot{\varphi}_i dt + \int_0^T m_i g l \dot{\varphi}_i \sin \varphi_i dt = 0, \quad i = 1, 2. \quad (72)$$

The energy supplied to the system by the van-der-Pol's damper in one period of oscillations is given by

$$W_i^{SELF} = - \int_0^T c_{\varphi vdp} \dot{\varphi}_i^2 dt, \quad i = 1, 2. \quad (73)$$

The next component on the right hand side of Eq. (71) represents the energy dissipated by the van-der-Pol's damper:

$$W_i^{VDP} = - \int_0^T c_{\varphi vdp} \zeta \varphi_i^2 \dot{\varphi}_i^2 dt, \quad i = 1, 2. \quad (74)$$

The last component of Eq. (71) represents the energy transfer from the pendulum to the beam or to the second pendulum (via beam):

$$W_i^{SYN} = \int_0^T m_i \ddot{x} l \cos \varphi_i \dot{\varphi}_i dt, \quad i = 1, 2. \quad (75)$$

Substituting Eqs. (72)–(75) into Eq. (71) one gets pendula's energy balances in the form

$$\begin{aligned} W_1^{SELF} - W_1^{VDP} - W_1^{SYN} &= 0, \\ W_2^{SELF} - W_2^{VDP} - W_2^{SYN} &= 0. \end{aligned} \quad (76)$$

Multiplying the equation of the beam motion (69) by beam velocity  $\dot{x}$  one gets:

$$\left( M + \sum_{i=1}^2 m_i \right) \ddot{x} \dot{x} + c_x \dot{x}^2 + k_x x \dot{x} + \left( \sum_{i=1}^2 m_i l (\ddot{\varphi}_i \cos \varphi_i - \dot{\varphi}_i^2 \sin \varphi_i) \right) \dot{x} = 0. \quad (77)$$

Integrating Eq. (77) over the period of oscillations we obtain the following energy balance:

$$\int_0^T \left( M + \sum_{i=1}^2 m_i \right) \ddot{x} \dot{x} dt + \int_0^T k_x x \dot{x} dt = - \int_0^T \left( \sum_{i=1}^2 m_i l (\ddot{\varphi}_i \cos \varphi_i - \dot{\varphi}_i^2 \sin \varphi_i) \right) \dot{x} dt - \int_0^T c_x \dot{x}^2 dt. \quad (78)$$

Left hand side of Eq. (79) represents the increase of the total energy of the beam which for the periodic oscillations is equal to zero:

$$\int_0^T \left( M + \sum_{i=1}^2 m_i \right) \ddot{x} \dot{x} dt + \int_0^T k_x x \dot{x} dt = 0. \quad (79)$$

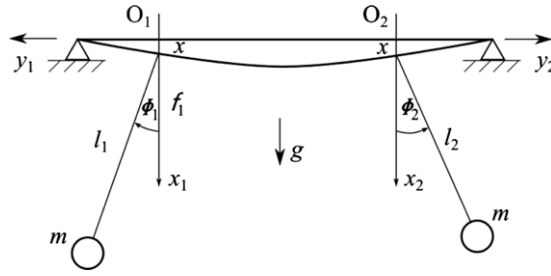


Fig. 19. Two clocks suspended on the beam which can perform transversal oscillations (after [35]).

The first component on the right-hand side of Eq. (78) represents the work performed by the horizontal component of the force with which pendula act on the beam causing its motion:

$$W_{beam}^{DRIVE} = - \int_0^T \left( \sum_{i=1}^2 m_i l_i (\ddot{\varphi}_i \cos \varphi_i - \dot{\varphi}_i^2 \sin \varphi_i) \right) \dot{x} dt. \quad (80)$$

The second component on the right hand side of Eq. (78) represents the energy dissipated by the damper  $c_x$ :

$$W_{beam}^{DAMP} = \int_0^T c_x \dot{x}^2 dt. \quad (81)$$

Substituting Eqs. (79) and (81) into Eq. (78) one gets energy balance in the following form

$$W_{beam}^{DRIVE} - W_{beam}^{DAMP} = 0. \quad (82)$$

In the case of the periodic oscillations it is possible to prove that

$$W_1^{SYN} + W_2^{SYN} = W_{beam}^{DRIVE} = W_{beam}^{DAMP} \quad (83)$$

so adding Eqs. (76) and (82) and considering Eq. (83) one obtains

$$W_1^{SELF} + W_2^{SELF} - W_1^{VDP} - W_2^{VDP} - W_{beam}^{DAMP} = 0. \quad (84)$$

Eq. (84) represents the energy balance of the whole system (68) and (69).

### 3.6. Model with the transversal oscillations of the beam

The models described in Sections 3.2–3.5 do not consider the transversal displacements of the beam as these displacements are very small and the observed phenomena of the clocks' synchronization occur far below the resonances for transversal oscillations of the typical wooden beam. The model with a low stiffness beam (string) has been considered in [35]. The clocks are suspended symmetrically about the middle of the beam as shown in Fig. 19. The beam deflection is described by the vertical displacement  $x$  of one of the suspension points for a specified symmetric deflection function. The positions of the pendula are determined by the angles  $\varphi_i$  ( $i = 1, 2$ ) counted from the vertical axes  $x_i$  in the opposite directions and assumed to be small. It has been assumed that the pendula masses  $m$  are identical, but the lengths  $l_i$  are similar but still different.

The kinetic energy of the system

$$T = \frac{1}{2} M \dot{x}^2 + \frac{1}{2} m \sum_{i=1}^2 (\dot{x}^2 - 2l_i \sin(\varphi_i) \dot{\varphi}_i + l_i^2 \dot{\varphi}_i^2),$$

where  $M$  is the effective mass of the beam with the virtual masses of clock mechanisms and cases (without pendula). The potential energy of the system is

$$V = \frac{1}{2} M \omega_{beam}^2 x^2 - mg \sum_{i=1}^2 l_i \cos \varphi_i,$$

where  $\omega_{beam}$  is the frequency of free oscillations of the beam with virtual masses without pendula and  $g$  is the acceleration of gravity. The equations of motion have the form

$$(M + 2m) \ddot{x} - m \sum_{i=1}^2 l_i (\varphi_i \ddot{\varphi}_i + \dot{\varphi}_i^2) = -M \omega_{beam}^2 x + Q_x \quad (85)$$

$$m l_i^2 \ddot{\varphi}_i - m l_i \varphi_i \ddot{x} = -m g l_i \varphi_i + Q_i,$$

where  $i = 1, 2$ ,  $Q_x$  is the linear-friction force in the beam and  $Q_i$  are the van der Pol nonlinear-friction forces. We write these generalized forces as

$$\begin{aligned}\frac{Q_x}{M + 2m} &= -\varepsilon_0 \dot{x}, \\ \frac{Q_i}{l_i m} &= \varepsilon_i \left(1 - \frac{S_i^2}{S_0^2}\right) \dot{S}_i,\end{aligned}$$

where  $\varepsilon_0$  and  $\varepsilon_i$  are the friction coefficients,  $S_i = l_i \varphi_i$ , and  $S_0$  are the deflections of the pendula at which the damping changes its sign.

Eq. (85) can be rewritten as

$$\begin{aligned}x'' + 2\frac{\varepsilon_0}{\omega}x' + 4\frac{\omega_0^2}{\omega^2}x &= \mu \left[ (y_1^2)'' + (y_2^2)'' \right], \\ y_i'' + \left( a_i - \frac{x''}{l_i} \right) y_i &= \delta (1 - y_i^2) y_i',\end{aligned}\tag{86}$$

where

$$\begin{aligned}\frac{M}{M + 2m} \omega_{beam}^2 &= \omega_0^2, \\ \frac{mS_0^2}{2l_1(M + 2m)} &\approx \frac{mS_0^2}{2l_2(M + 2m)} = \mu,\end{aligned}$$

$S_1/S_2 = y_1$ ,  $a_i = 4\omega_l^2/\omega^2$ ,  $g/l_i = \omega_l^2$ ,  $2\varepsilon_1 S_0^2/\omega l_1 \approx 2\varepsilon_2 S_0^2/\omega l_2 = \delta$ . In Eqs. (86), the prime denotes differentiation with respect to the nondimensional time  $z = \omega t/2$  ( $\omega$  is the unknown frequency of beam oscillations). We set  $l_1 \approx l_2$  in the coefficients of small nonlinear terms and in the coefficients of the van der Pol damping.

In [35] Eq. (86) have been studied using the approximate analytical method of harmonic balance. It has been shown that the exact antiphase synchronization of nonidentical pendula cannot occur but slightly different pendula can perform synchronous motion close to antiphase oscillations.

## 4. Synchronization of two pendulum clocks

### 4.1. Experimental observations

For our experiments we take two contemporary pendulum clocks (type: SN-13, produced in 2003 in the Factory of Clocks in Torun, Poland) which are shown in Fig. 20(a)–(d). These clocks have typical escapement mechanisms described in [43,48] and the pendula of the length 0.269 (m) and mass 0.158 (kg). The total mass of the clock is equal to 5.361 (kg). The clocks are covered in the wooden case. The clocks in experiment have been selected in such a way to be as identical as possible but we noticed a small time difference of 1 (s) after 24 h. When the clocks have been hung on the wall as in Fig. 20(a) no synchronization has been observed.

Next the clocks have been hung on the wooden beam (length – 1.13 (m), mass – 1.45 (kg)) and located on two chairs as in the original Huygens experiment in Fig. 1. Our setup is shown in Fig. 20(b). In this case we have not observed clocks synchronizations but we noticed the frequent switch off of one of the clocks (the amplitude death of its pendulum). This effect occurs due to the spherical motion of the clocks' cases and subsequently their pendula. The spherical motion of the pendula (with too large amplitudes) switches off the escapement mechanism which is designed for the planar motion of the pendulum. To reduce the amplitudes of the spherical oscillations we balanced the clocks by adding additional masses into their cases but we have not observed the synchronization.

Later two chairs have been replaced by the tables with a flat horizontal desks. On the desk we put some oil to reduce the friction and allow beam sliding on the table desks but the synchronizations has not been observed (Fig. 20(c)). Finally, the synchronization has been observed in the setup shown in Fig. 20(d) the beam with a hanging clock has been located on the rolls which can roll on the table desks. We have been trying to reduce the friction by polishing the surfaces of the beam, table desks and rolls. Depending on initial conditions it has been possible to observe both in-phase and anti-phase synchronization of the clock's pendula.

Similar results have been obtained in the experiments performed at the “Mekhanobr” Institute in Sankt Petersburg [8] and at Georgia Institute of Technology in Atlanta [33]. Blekhman [8] reports the results of a laboratory reproduction of the coupled clocks in which he observes both in-phase and antiphase synchronization. He also states that these results are in full agreement with the theoretical study base on continuous model (Eqs. (68) and (69) in Section 3.5) in which he predicts that both in-phase and antiphase motions are stable under the same circumstances (i.e., the system has two coexisting attractors). However no details of this experiments are available. Experiments of [33] are well documented. They re-examine Huygens's synchronization observations in an experiment with two pendulum clocks mounted side by side on a single wooden beam.

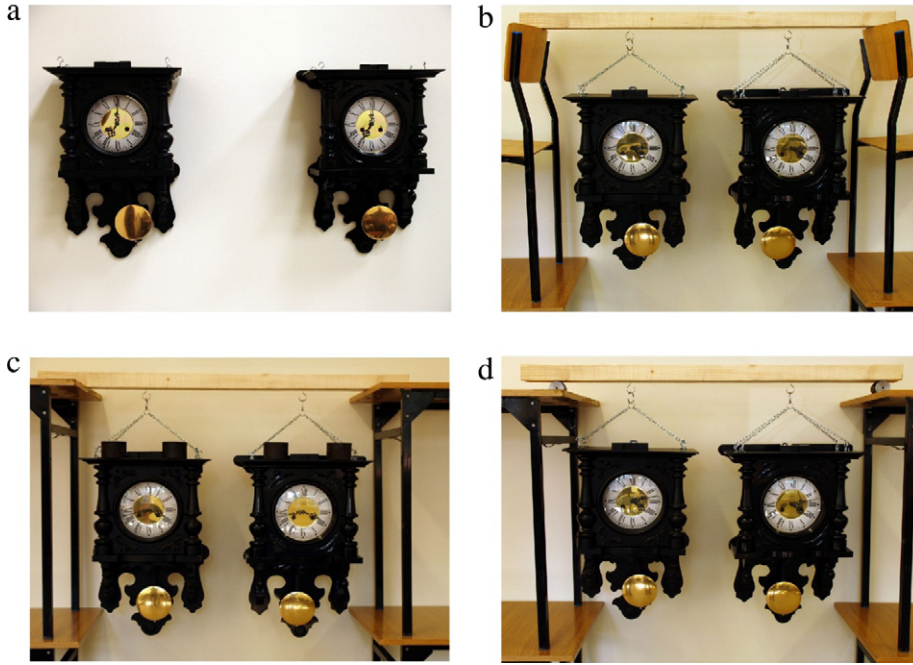


**Fig. 20.** Experiments with two pendulum clocks: (a) clocks hanging on the wall, (b) clocks hanging from the beam located on the chairs' backs, (c) clocks hanging from the beam which can slide on the tables' desks, (d) clocks hanging from the beam which can roll horizontally on the tables' desks.

The commercially available pendulum clocks (spring-wound time pieces - Model 771-000, Uhrenfabrik Franz Hermle & Sohn, Gosheim, Germany) have been used. Each clock contains a 14.0 cm pendulum (with a nominal frequency of 1.33 (Hz)) of mass  $m = 0.082$  (kg); the pendulum is coupled to an anchor escapement, which enables the clock movement to function with small angular displacements of approximately  $8^\circ$  from vertical. The beam is mounted on a low-friction wheeled cart (Model ME-9454, Pasco Scientific, Roseville, CA). The combined system of clocks, beam and cart is placed atop a slotted track (ME-9429A, Pasco Scientific), which permits the system to translate freely in a direction parallel to the beam. The total mass of the cart and clocks without the pendulums is  $M$ . Weights are added to and removed from the cart to change  $M$  and, thereby, to change the system mass ratio  $\mu = m/(2m + M)$ . The motion of each pendulum is monitored by tracking a laser beam reflected from the pendulum suspension using a position-sensing detector (Model 1L30, On-Trak Photonics, Lake Forest, CA). The lasers and detectors are mounted on the system, permitting measurement of each pendulum's angular position in the system reference frame. The voltage signal from each detector is recorded using a computer-based data-acquisition system; complex demodulation of the signals yields measurement of each pendulum's oscillation amplitude, frequency and phase as a function of time. The clocks synchronize in anti-phase for some values of the system mass ratio  $\mu$  (comparable with that reported by Huygens). Simultaneously the beating oscillations leading to the amplitude death have been observed.

#### 4.2. Numerical results

In our numerical simulations Eqs. (27) and (28) or (68) and (69) have been integrated by the Runge–Kutta method. The initial conditions have been set as follows; (i) for the beam  $x(0) = \dot{x}(0) = 0$ , (ii) for the pendula the initial conditions  $\varphi_i(0), \dot{\varphi}_i(0)$  have been calculated from the assumed initial phase differences  $\beta_1$  and  $\beta_2$  (in all calculations  $\beta_1 = 0$  has been taken) using Eqs. (29) and (30), i.e.,  $\varphi_1(0) = 0, \dot{\varphi}_1(0) = \alpha\Phi, \varphi_2(0) = \Phi \sin \beta_2, \dot{\varphi}_2(0) = \alpha\Phi \cos \beta_2$ .

To study the stability of the solution of Eqs. (27) and (28) we add perturbations  $\delta_i$  and  $\sigma$  to the variables  $\varphi_i$  and  $x$  and obtain the following linearized variational equation:

$$m_i l_i^2 \ddot{\delta}_i + m_i \ddot{\sigma} l_i \cos \varphi_i + m_i l_i (g \cos \varphi_i - \ddot{x} \sin \varphi_i) + c_{\varphi_i} \dot{\delta}_i = 0, \quad (87)$$

$$(M + m_1 + m_2) \ddot{\sigma} + \sum_{i=1}^2 (m_i l_i \ddot{\delta}_i^2 \cos \varphi_i - m_i l_i \dot{\varphi}_i^2 \delta_i \cos \varphi_i - m_i l_i \ddot{\varphi}_i \delta_i \sin \varphi_i - 2m_i l_i \dot{\varphi}_i \dot{\delta}_i \sin \varphi_i) + c_x \dot{\sigma} + k_x \sigma = 0,$$

where  $i = 1, 2$ . The solution of Eqs. (27) and (28) given by  $\varphi_i(t)$  and  $x(t)$  is stable while the solution of Eqs. (87)  $\delta_i(t)$  and  $\sigma(t)$  tends to zero for  $t \rightarrow \infty$ .

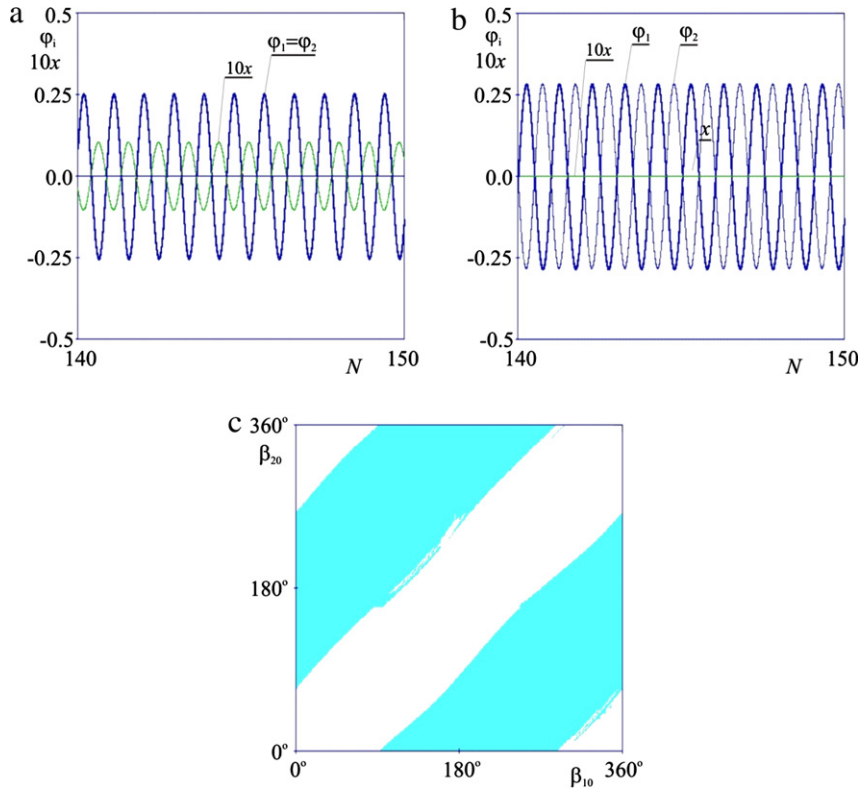


**Fig. 21.** (Color online) Synchronization of two identical pendulum clocks:  $m_1 = m_2 = 1.0$  (kg),  $l = g/4\pi^2 = 0.2485$  (m),  $M = 10.0$  (kg),  $c_{\varphi_1} = c_{\varphi_2} = 0.0083$  (N s m),  $c_x = 1.53$  (N s/m),  $k_x = 4.0$  (N/m),  $\gamma_N = 5.0^\circ$ ,  $M_{N1} = M_{N2} = 0.075$  (N m); (a, b) time series of pendula  $\varphi_1$ ,  $\varphi_2$  and beam  $x$  displacements, time on the horizontal axis is given in the following way  $t = NT$ , where  $N = 1, 2, 3, \dots$  and  $T = 1$  (s), (a) complete synchronization ( $\varphi_1 = \varphi_2$ ) pendula are in the antiphase to the oscillations of the beam  $M$ , (b) antiphase synchronization ( $\varphi_1 = -\varphi_2$ ), beam  $M$  is at rest, (c) basins of attraction of complete synchronization (white color) and antiphase synchronization (gray/blue online color) in  $\beta_{10} - \beta_{20}$  plane,  $x(0) = 0.0$ ,  $\dot{x}(0) = 0.0$ ,  $\varphi_{i0} = \Phi \sin \beta_{i0}$ ,  $\dot{\varphi}_{i0} = \alpha \Phi \cos \beta_{i0}$ .

#### 4.2.1. Synchronization of two identical pendula

Depending on initial conditions one can observe two different types of synchronization in the considered system. Two pendula with identical masses and periods of oscillations can obtain the state of complete synchronization when ( $\varphi_1 = \varphi_2$ ) and beam  $M$  oscillates in antiphase to the pendula or the state of antiphase synchronization when ( $\varphi_1 = -\varphi_2$ ) and beam  $M$  is at rest [33,8,45].

Both types of synchronization are shown in Fig. 21(a)–(c). In our numerical simulations we consider the following parameter values: pendula' masses -  $m_1 = m_2 = 1.0$  (kg), the length of the pendula  $l = g/4\pi^2 = 0.2485$  (m) (it has been selected in such a way that when the beam  $M$  is at rest the period of the pendulum oscillations is equal to  $T = 1.0$  (s) and oscillations frequency to  $\alpha = 2\pi$  (s $^{-1}$ )),  $g = 9.81$  (m/s $^2$ ) is an acceleration due to the gravity, beam mass  $M = 10.0$  (kg), damping coefficients  $c_{\varphi_1} = c_{\varphi_2} = 0.0083$  (N s m) and  $c_x = 1.53$  (N s/m) and stiffness coefficient  $k_x = 4.0$  (N/m). When the displacements of the pendula are smaller than  $\gamma_N = 5.0^\circ$  the escapement mechanisms generate driving moments  $M_{N1} = M_{N2} = 0.075$  (N m) and allow the pendula to oscillate with amplitude  $\Phi_1 = \Phi_2 = \Phi = 0.2575$  ( $\approx 14.75^\circ$ ) while beam  $M$  is at rest.

Fig. 21(a) presents the complete synchronization of the pendula of both clocks, i.e., the pendula' displacements (which are the same  $\varphi_1 = \varphi_2$ ) and the displacements of the beam  $x$  (shown in 10 times magnification). The time series are shown in the stationary state after the decay of transients. Time on the horizontal axis is given in the following way  $t = NT$ , where  $N = 1, 2, 3, \dots$  and  $T$  is a period of pendulum's oscillations when the beam is at rest. Notice that the numerically estimated value of the amplitude  $\Phi_{1,2} = 0.283$  is approximately equal to the value which can be calculated from Eq. (55). In Fig. 21(b) we present the example of antiphase synchronization, i.e.,  $\varphi_1(t) = \varphi_2(t + 0.5T)$  (or  $\varphi_1(t) = -\varphi_2(t)$ ) and the beam  $M$  is at rest as  $x = 0.0$ . Both types of synchronization have been obtained for the same parameter values but different initial conditions. Fig. 21(c) shows the basins of attraction of both types of synchronization in  $(\beta_{10}, \beta_{20})$  plane. White and gray (blue online) colors indicate initial conditions leading respectively to complete and antiphase synchronization. In the case of complete synchronization both clocks are significantly faster (nearly 6 min per hour – Fig. 21(a)) in reference to the clock mounted to the nonmoving base. This difference occurs as the result of the pendula' motion in the antiphase to the beam. In the case of antiphase synchronization (Fig. 21(b)) the clocks remain accurate.

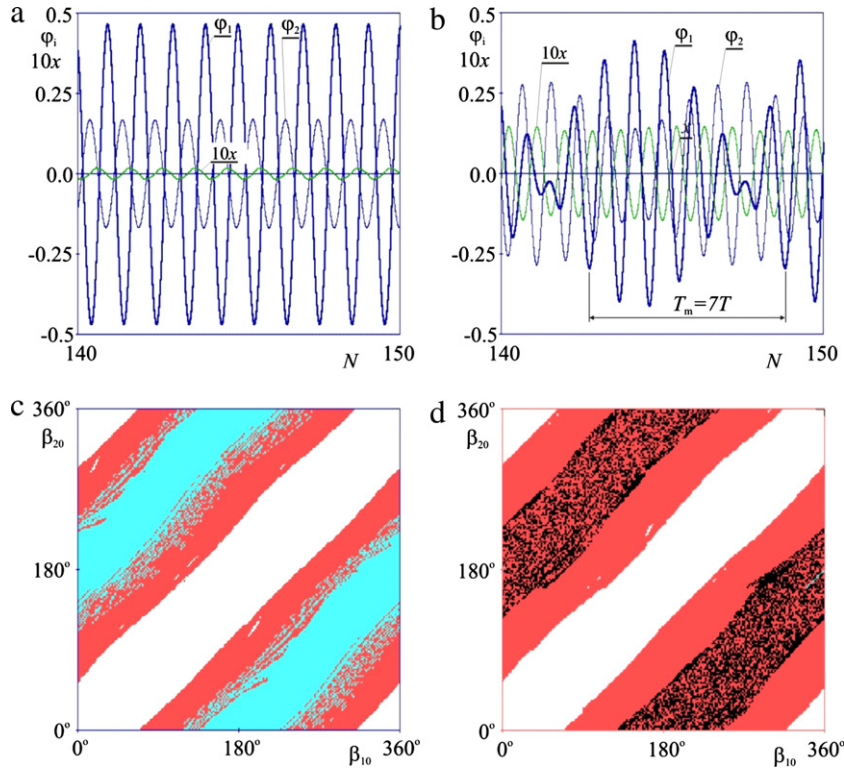


**Fig. 22.** (Color online) Synchronization of two pendula with different masses:  $m_1 = 1.0$  (kg),  $l = g/4\pi^2 = 0.2485$  (m),  $M = 10.0$  (kg),  $c_x = 1.53$  (N s/m),  $k_x = 4.0$  (N/m),  $\gamma_N = 5.0^\circ$ ,  $c_{\varphi_1} = 0.0083$  (N s),  $c_{\varphi_2} = 0.0083 \times m_2$  (N s m),  $M_{N1} = 0.075$  (N m),  $M_{N2} = 0.075 \times m_2$  (N m); (a, b) time series of pendula  $\varphi_1$ ,  $\varphi_2$  and beam  $x$  displacements, time on the horizontal axis is given in the following way  $t = NT$ , where  $N = 1, 2, 3, \dots$  and  $T = 1$  (s), (a) phase synchronization:  $m_2 = 2.65$  (kg),  $\beta_{10} = 10^\circ$ ,  $\beta_{20} = 130^\circ$ ; (b) long period synchronization:  $m_2 = 2.65$  (kg),  $T_m \approx 7T$ ,  $\beta_{10} = 1^\circ$ ,  $\beta_{20} = 90^\circ$ ; (c) basins of attraction of different types of synchronization: complete synchronization (white), phase synchronization (light gray, blue color online), long period synchronization (dark gray, red color online) in  $\beta_{10} - \beta_{20}$  plane:  $x(0) = 0.0$ ,  $\dot{x}(0) = 0.0$ ,  $\varphi_{10} = \Phi \sin \beta_{10}$ ,  $\dot{\varphi}_{10} = \alpha \Phi \cos \beta_{10}$ ,  $m_2 = 2.65$  (kg), (d) basins of attraction of different types of synchronization: complete synchronization (white), long period synchronization (dark gray, red color online) chaotic behavior (black) in  $\beta_{10} - \beta_{20}$  plane:  $x(0) = 0.0$ ,  $\dot{x}(0) = 0.0$ ,  $\varphi_{10} = \Phi \sin \beta_{10}$ ,  $\dot{\varphi}_{10} = \alpha \Phi \cos \beta_{10}$ ,  $m_2 = 3.105$  (kg).

#### 4.2.2. Synchronization of two pendula with different masses

(i) *Damping coefficients  $c_{\varphi_{1,2}}$  and moments  $M_{Ni}$  proportional to the pendula masses  $m_{1,2}$*

When the clocks have the pendula with different masses ( $m_1 \neq m_2$ ), the considered system shows three different types of synchronous behavior. The first one is the complete synchronization ( $\varphi_1 = \varphi_2$ ) already observed in the case of identical systems in Section 4.2.1. The second one is the phase synchronization which evolves from the anti-phase synchronization of the identical systems. For nonidentical masses of the pendula the phase difference between pendula decreases and is smaller than  $\pi$  ( $180^\circ$ ) and contrary to the case of identical clocks the beam  $M$  is not at rest and pendula' amplitudes are not equal.

Different types of synchronization states and their basins of attraction are presented in Fig. 22(a)–(d). In our numerical simulations we consider the following parameter values:  $l = g/4\pi^2 = 0.2485$  (m),  $M = 10.0$  (kg),  $c_x = 1.53$  (N s/m),  $k_x = 4.0$  (N/m),  $m_1 = 1.0$  (kg),  $m_2 = 2.65$  (kg),  $\gamma_N = 5.0^\circ$ ,  $c_{\varphi_1} = 0.0083$  (N m s),  $c_{\varphi_2} = 0.0083 \times m_2$  (N m s),  $M_{N1} = 0.075$  (N m),  $M_{N2} = 0.075 \times m_2$  (N m). Fig. 22(a) presents the phase synchronization in which the pendula' displacements  $\varphi_1$  and  $\varphi_2$  are shifted by the angle close to  $\pi$  but smaller than this value. Similarly, the oscillations of the beam  $x$  are phase shifted to the pendula' oscillations by the value close but not equal to  $\pi/2$ . The first pendulum (with smaller mass  $m_1$ ) exhibits the oscillations with the larger amplitude (than in the case when beam  $M$  is at rest). The analysis of Section 3.4.2 explains this phenomenon showing that this pendulum is driven by the second pendulum via beam  $M$  (the part of pendulum 2 energy is transferred to pendulum 1). As the result the amplitude of the second pendulum's oscillations is larger (than in the case when beam  $M$  is at rest).

In the considered system besides the complete and phase synchronization one can observe the synchronization state in which  $\varphi_1 - \varphi_2$  is a periodic function. As the period of this function  $T_m$  is larger than  $T$  (the period of pendula' oscillations in the case when beam  $M$  is at rest) this type of generalized synchronization is called a long period synchronization. The long period synchronization can be a special case of  $n : m$  synchronization observed in the self-excited continuous systems [103,50]. Since the system (27) and (28) is discontinuous and we have not proved the existence of the quasiperiodic solution on the torus in it we decide to use other name. Fig. 22(b) presents the example of this type of synchronization obtained for the initial conditions  $\beta_{10} = 1.0^\circ$  and  $\beta_{20} = 90.0^\circ$ . One can observe that  $T_m$  is equal to  $7T$ . Long period synchronization can

be explained by the periodic decrease of the amplitude  $\Phi_1$  of pendulum 1 oscillations. When this amplitude is smaller than the minimum value  $\Phi_1 = \gamma_N$  the escapement mechanism is switched off. These switches off introduce the perturbation to the system. The basins of attraction of three coexisting attractors are shown in Fig. 22(c) in  $\beta_{10} - \beta_{20}$  plane. White and light gray (blue online) colors indicate initial conditions leading respectively to complete and phase synchronization while the region shown in dark gray (red online) color indicates initial conditions leading to long period synchronization. Our calculations show, that the dark gray basin of long period synchronization appears at  $m_2 \approx 2.4$  (kg). With the increase of  $m_2$  the basin of phase synchronization becomes smaller and finally disappears for  $m_2 \approx 2.8$  (kg). In the considered system one can observe long period synchronization states with different  $T_m$  (the largest observed  $T_m$  is equal to 51T). Long period synchronization can coexist with the chaotic behavior of the clocks' pendula (see also Section 4.2.4). The example of such coexistence is shown in Fig. 22(d) ( $m_2 = 3.105$  (kg)) where the basins of complete (white color), long period with  $T_m = 13T$  (dark gray, red online) synchronization and chaotic behavior (black color) are shown.

In the case of phase synchronization both clocks are slightly slower (nearly 20 (s) per hour –Fig. 22(a)) in reference to the clock mounted to the nonmoving base. The same difference occurs in the case of long period synchronization (25 (s) per hour –Fig. 22(b)).

In Fig. 23(a)–(c) we present the bifurcation diagram of the system (27) and (28). The mass of pendulum 2 –  $m_2$  has been taken as a control parameter. On the vertical axis the displacements of the pendula  $\varphi_1, \varphi_2$ , the beam displacement  $x$  (for better visibility  $x$  has been multiplied by 10); values  $\varphi_2$  and  $x$  have been taken at the time of the greatest positive displacement of the first pendulum  $\varphi_1$ , i.e., when  $\dot{\varphi}_1$  changes the sign from positive to negative values. In Fig. 23(a) and 31(b) the bifurcation diagrams for respectively increasing and decreasing values of  $m_2$  are shown. In Fig. 23(a) we start from the antiphase synchronization of identical systems (i.e.,  $m_2 = 1.0$  (kg)). The antiphase synchronization is replaced by the phase synchronization (PS) with decreasing phase shift which can be observed in the interval  $1.0 < m_2 < 12.3$  (kg). For larger values of  $m_2$  one observes long period synchronization (LPS) and chaotic oscillations (C) of the clocks' pendula ( $12.3 < m_2 < 15.25$  (kg)). This behavior is replaced by complete synchronization for  $m_2 > 15.25$  (kg). Fig. 23(b) shows that starting from the complete synchronization (CS) for  $m_2 = 26$  (kg) and decreasing the values of  $m_2$  we observe this type of synchronization in the whole interval  $1.0 < m_2 < 26.0$  (kg). In Fig. 23(c) we start from the chaotic oscillations for  $m_2 = 15.0$  (kg) and decrease the value of the control parameter  $m_2$ . Chaotic oscillations with the windows of long period synchronization are preserved in the interval  $2.9 < m_2 < 15.0$  (kg) and for smaller values of  $m_2$  are replaced by complete synchronization.

Fig. 23(a)–(c) confirms the coexistence of different types of synchronous behavior. For  $1.0 < m_2 < 2.9$  (kg) complete and phase synchronizations coexist. In the interval  $2.9 < m_2 < 12.3$  (kg) we observe complete, phase and long period synchronization (with different  $n$ ). For larger values of  $m_2$  ( $12.3 < m_2 < 15.25$  (kg)) phase synchronization disappears and we observe complete and long period synchronization. Finally, for  $m_2 > 15.25$  only the complete synchronization is possible.

The system behavior for  $m_2$  smaller than  $m_1$  is discussed in Fig. 24(a, b). Bifurcation diagram is presented in Fig. 24(a) where we start from the phase synchronization for  $m_2 = 1.0$  (kg) and decrease the value of control parameter up to  $m_2 = 0.1$  (kg). Phase synchronization is preserved in the interval  $1.0 > m_2 > 0.285$  (kg) (it coexists with complete synchronization). For smaller values of  $m_2$  we observe only the complete synchronization. The disappearance of the phase synchronization is explained in Fig. 24(b) where we present the time series of the pendula displacements  $\varphi_1$  and  $\varphi_2$  for  $m_2 = 0.285$  (kg) (close to the threshold value). Notice that the amplitude of pendulum 1 is only slightly larger than  $\gamma_N = 5.0^\circ$ . Further decrease of  $m_2$  results in the switch off of the escapement mechanism and allows the transition to complete synchronization. For  $m_2 < m_1$  long period synchronization has not been observed. Notice that in Fig. 24(b) the phase shift  $\beta_2$  between pendula's displacements is smaller than  $\pi$  ( $180.0^\circ$ ) and approximately equal to  $126^\circ$ . Similarly, as in the example of Fig. 22(a), the difference in the pendula's amplitudes is created by the energy transfer from pendulum 1 to pendulum 2, as described in Section 3.4.2 by Eqs. (60).

To explain why the antiphase synchronization of the identical clocks is replaced by the phase synchronization of nonidentical ones, let us consider the energy balance of the synchronized states shown in Fig. 25(a, b).

In the case of antiphase synchronization of identical pendula (Fig. 25(a)) we have two independent streams of energy (both fulfill Eq. (53)), as both pendula dissipate the same amount of energy as they gain from the escapement mechanism. In Fig. 25(b) we presented the energy balance of the pendula with different masses in the state of phase synchronization. We consider the parameter values of Fig. 25(b) and numerically calculated pendulum's amplitudes  $\Phi_1 = 0.121$  and  $\Phi_2 = 0.548$ . The streams fulfill Eq. (60). The energy supplied by the escapement mechanism to the first pendulum (one with smaller amplitude)  $W_1^{DRIVE}$  is divided in to the energy dissipated in the damper  $c_{\varphi_1}$  and energy  $W^{SYN}$  transferred to the second pendulum. Notice that the phase shift  $\beta_2$  calculated from Eq. (62) is approximately the same as the numerically calculated value  $\beta_2 = 126^\circ$  (see Fig. 25(b)). Eqs. (41), (42) and (49) allow the estimation of the energies:  $W_i^{DRIVE}$ ,  $W_i^{DAMP}$  and  $W_i^{SYN}$ . The comparison of analytical and numerical results is presented in Table 1.

The differences between analytical and numerical results are small (values  $W_1^{DRIVE}$  and  $W_2^{DRIVE}$  are exact) which confirm the accuracy of our energy balance approach. The value of  $W_b^{DAMP} = 0.00029$  (N m) is significantly smaller than the values of other energies and is not considered in Fig. 25(a, b) and Table 1.

The analytical studies of Section 3.4 are based on the assumption that the periods of pendula' oscillations are constant and equal to  $2\pi/\alpha$ . When the clocks are coupled via movable beam the pendula's periods are not constant and depend on the

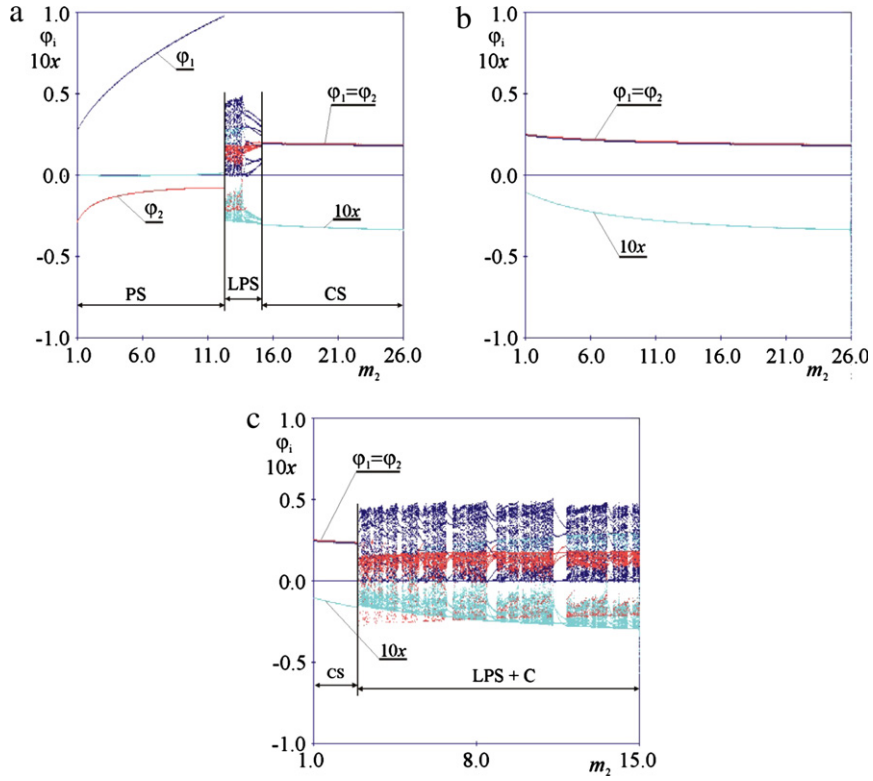


**Fig. 23.** (Color online) Bifurcation diagrams of system (27) and (28):  $\varphi_1, \varphi_2$  and  $x$  versus control parameter  $m_2$ :  $\Phi_1 \approx \gamma_N = 5.0^\circ, m_1 = 1.0$  (kg),  $l = g/4\pi^2 = 0.2485$  (m),  $M = 10.0$  (kg),  $c_x = 1.53$  (N s/m),  $k_x = 3.94$  (N/m),  $\gamma_N = 5.0^\circ, c_{\varphi_1} = 0.0083$  (N s m),  $c_{\varphi_2} = 0.0083 \times m_2$  (N s m),  $M_{N1} = 0.075$  (N m),  $M_{N2} = 0.075 \times m_2$  (N m); (a)  $m_2$  increases from 1 to 26.0, (b)  $m_2$  decreases from 26.0 to 1.0, (c)  $m_2$  decreases from 15.0 to 1.0.

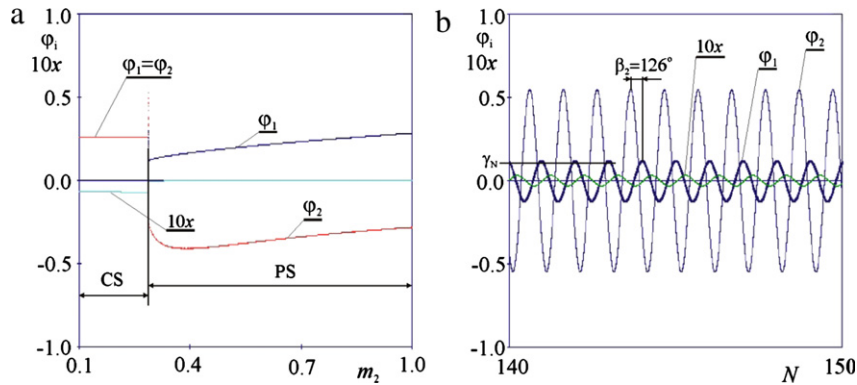


**Fig. 24.** (Color online) (a) Bifurcation diagram of system (27) and (28):  $\varphi_1, \varphi_2$  and  $x$  versus control parameter  $m_2$ ;  $m_2$  decreases from 1.0 (kg) to 0.1 (kg), (b) time series of  $\varphi_1, \varphi_2$  and  $x$  during the phase synchronization:  $\Phi_1 \approx \gamma_N = 5.0^\circ, m_1 = 1.0$  (kg),  $l = g/4\pi^2 = 0.2485$  (m),  $M = 10.0$  (kg),  $c_x = 1.53$  (N s/m),  $k_x = 3.94$  (N/m),  $\gamma_N = 5.0^\circ, c_{\varphi_1} = 0.0083$  (N s m),  $c_{\varphi_2} = 0.0083 \times m_2$  (N s m),  $M_{N1} = 0.075$  (N m),  $M_{N2} = 0.075 \times m_2$  (N m).

**Table 1**

Comparison of analytical and numerical results:  $m_1 = 1.0$  (kg),  $m_2 = 0.289$  (kg),  $l = g/4\pi^2 = 0.2485$  (m),  $M = 10.0$  (kg),  $c_x = 1.53$  (N s/m),  $k_x = 3.94$  (N/m),  $\gamma_N = 5.0^\circ, c_{\varphi_1} = 0.0083$  (N s),  $c_{\varphi_2} = 0.0083 \times m_2$  (N s m),  $M_{N1} = 0.075$  (N m),  $M_{N2} = 0.075 \times m_2$  (N m).

	Numerical	Analytical
$W_1^{SYN}$	$W_1^{SYN} = \int_0^T m_1 \ddot{x} l \cos \varphi_1 \dot{\varphi}_1 dt = -0.0101$ (N m)	$W_1^{SYN} = -W_2^{SYN}$
$W_2^{SYN}$	$W_2^{SYN} = \int_0^T m_2 \ddot{x} l \cos \varphi_2 \dot{\varphi}_2 dt = 0.0100$ (N m)	$W_2^{SYN} = \frac{2m_2 l^2 \alpha^4 \pi \Phi_1}{k_x - \alpha^2 U} m_2 \Phi_2 \sin \beta_2 = 0.0107$ (N m)
$W_1^{DRIVE}$	$W_1^{DRIVE} = 2M_{N1} \gamma_N = 0.0131$ (N m)	$W_1^{DRIVE} = 2M_{N1} \gamma_N = 0.0131$ (N m)
$W_2^{DRIVE}$	$W_2^{DRIVE} = 2M_{N2} \gamma_N = 0.0036$ (N m)	$W_2^{DRIVE} = 2M_{N2} \gamma_N = 0.0036$ (N m)
$W_1^{DAMP}$	$W_1^{DAMP} = \int_0^T c_{\varphi_1} \dot{\varphi}_1^2 dt = 0.0028$ (N m)	$W_1^{DAMP} = \pi \alpha c_{\varphi_1} \Phi_1^2 = 0.0024$ (N m)
$W_2^{DAMP}$	$W_2^{DAMP} = \int_0^T c_{\varphi_2} \dot{\varphi}_2^2 dt = 0.0137$ (N m)	$W_2^{DAMP} = \pi \alpha c_{\varphi_2} \Phi_2^2 = 0.0143$ (N m)

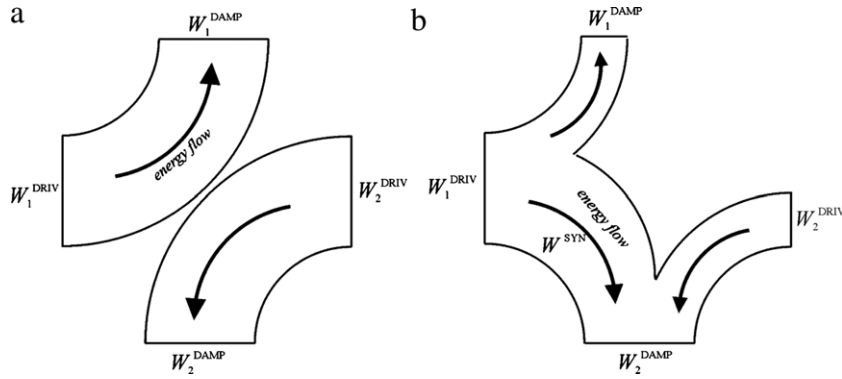


**Fig. 25.** Energy balance of pendula; (a) antiphase synchronization of identical pendula – there is no transfer of energy between pendula, (b) phase synchronization of the pendula with different masses:  $m_1 = 1.0$  (kg) and  $m_2 = 0.289$  (kg) and  $\phi_1 \approx \gamma_N = 5.0^\circ$  – pendulum 1 transfers the energy to pendulum 2 via beam  $M$ .

pendula's masses. The variations of this period are small (for example smaller than 5% for the  $m_2/m_1 = 11$  and parameters of Table 1).

(ii) *Constant damping coefficients  $c_{\varphi 1} = c_{\varphi 2} = c_\varphi$  and constant driving moments  $M_{N1} = M_{N2} = M_N$*

In the numerical simulations presented below we used the following system parameters: mass of pendulum 1  $m_1 = 1.0$  (kg); the length of the pendula  $l = g/4\pi^2 = 0.2485$  (m) (it has been selected in such a way that when the beam  $M$  is at rest, the period of pendulum oscillations is equal to  $T = 1.0$  (s) and oscillations frequency to  $\alpha = 2\pi$  ( $s^{-1}$ )),  $g = 9.81$  ( $m/s^2$ ) is an acceleration due to the gravity, beam mass  $M = 10.0$  (kg), damping coefficients  $c_{\varphi 1} = c_{\varphi 2} = c_\varphi = 0.01$  (N s) and  $c_x = 1.53$  (N s/m) and stiffness coefficient  $k_x = 4.0$  (N/m). When the displacements of the pendula are smaller than  $\gamma_N = 5.0^\circ$ , the escapement mechanisms generate driving moments  $M_{N1} = M_{N2} = 0.075$  (N m) and allow the pendula to oscillate with amplitude  $\Phi_1 = \Phi_2 = \Phi = 0.2575$  ( $\approx 14.75^\circ$ ) when beam  $M$  is at rest. Additionally in the continuous clocks' model Eqs. (68) and (69) we consider the following values of van der Pol's damper (causing the self-excited oscillations) coefficients  $c_{\varphi vdp} = -0.01$  (N s m) and  $\zeta = 60.0$ . Note that because the self-oscillations  $c_{\varphi vdp}$  and damping  $\zeta$  coefficients of two pendula are the same, in the case of the unmovable beam both pendula have the same amplitude  $\Phi = 0.26$  ( $\approx 15^\circ$ ) regardless of their masses. The motion of the beam may change both the period and oscillations amplitude. In both discontinuous (Eqs. (27) and (28)) and continuous (Eqs. (68) and (69)) models mass  $m_2$  of pendulum 2 has been taken as a control parameter. It varies in the wide interval to examine the influence of its changes on the type of the observed synchronization as the primary objective of these simulations is to investigate the influence of the nonidentity of the pendula on the observed types of synchronization.

(a) *From complete to (almost) antiphase synchronization*

The evolution of the behavior of the discontinuous system (27) and (28) starting from complete synchronization of identical clocks ( $m_1 = m_2 = 1.0$  (kg)) and the increase of the values of control parameter  $m_2$  is illustrated in Fig. 26(a)–(d). In Fig. 26(a) we present the bifurcation diagram of the system. The mass of pendulum 2 –  $m_2$  has been taken as a control parameter and it increases in the interval  $[1.0, 41.0]$ . In the initial state ( $m_1 = m_2$ ) the pendula exhibit complete synchronization.

The increase of the bifurcation parameter leads to the reduction of the oscillations amplitudes of both pendula which are in the state of almost complete synchronization; their movements are not identical, but very close to identical as shown in Fig. 26(b). Fig. 26(b) shows the displacements of the pendula  $\varphi_1, \varphi_2$  and the beam  $x$  (for better visibility enlarged 10 times) for  $m_1 = 1.0$  (kg) and  $m_2 = 3.0$  (kg). Notice that  $\varphi_1 \approx \varphi_2$  as the differences are hardly visible. Further increase of the mass  $m_2$  results in the further reduction of pendula's amplitudes and the increase of the beam amplitude as can be seen in Fig. 26(c) for the  $m_2 = 20.0$  (kg). The period of pendula's oscillations decreases (in Fig. 26(b) we observe 11.5 periods while in Fig. 26(c) 17.5 in the same time interval). This reduction is due to the fact that while increasing the mass of pendulum 2, the center of the mass moves towards the ends of the pendula, i.e., towards the material points with masses  $m_1$  and  $m_2$  and moves away from the beam with constant mass  $M$  ( $M = 10$  (kg) is smaller than  $m_2$ ). For  $m_2 = 30.2$  (kg) the amplitude of pendula's oscillations decreases to limit  $\Phi \approx \gamma_N = 5^\circ$ , below which the escapement mechanism is turned off. For larger values of  $m_2$ , we observe the oscillations of pendulum 1 with amplitude  $\Phi \approx 15^\circ$ , and small oscillations of pendulum 2 (whose escapement mechanism is switched off as can be seen in Fig. 26(d)). The pendulum moves due to the energy supplied to it by pendulum 1 via the beam.

The evolution of the van der Pol's system (Eqs. (68) and (69)) behavior starting from complete synchronization of identical pendula ( $m_1 = m_2 = 1.0$  (kg)) and increasing the value of control parameter  $m_2$  is illustrated in Fig. 27(a)–(f). Fig. 27(a) presents the bifurcation diagram for the increasing values of  $m_2$  ( $m_2 \in [1.0, 6.0]$ ). On the vertical axis we show the

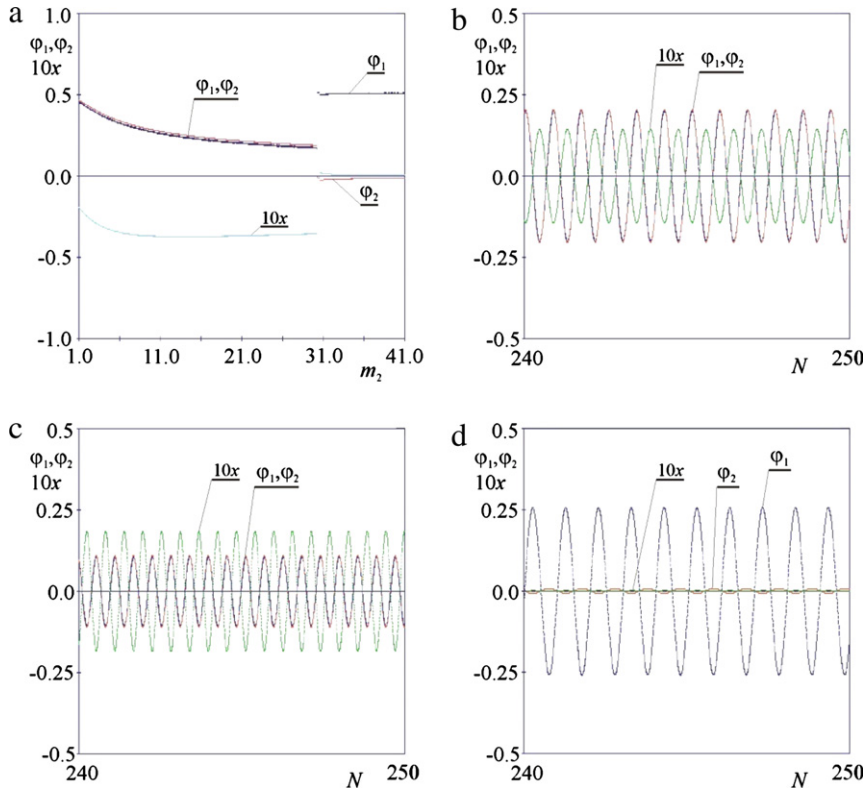


**Fig. 26.** Evolution from complete to almost antiphase synchronization; (a) bifurcation diagram for increasing values of  $m_2$ , (b) time series of almost complete synchronization  $m_1 = 1.0$  (kg) and  $m_2 = 3.0$  (kg); (c) time series of almost complete synchronization  $m_1 = 1.0$  (kg) and  $m_2 = 20.0$  (kg); (d) time series of almost antiphase synchronization for  $m_1 = 1.0$  (kg) and  $m_2 = 35.0$  (kg)—the escapement mechanism of pendulum 2 is switched off.

maximum values pendulum 1 displacement  $\varphi_1$ , and the displacement of pendulum 2  $\varphi_2$  and the beam  $x$  recorded at the moments when  $\varphi_1$  is maximum. Calculating this diagram we start with a state of complete synchronization of pendula with masses  $m_1 = m_2 = 1.0$  (kg), during which two pendula move in the same way ( $\varphi_1 = \varphi_2$ ) in the antiphase to the movement of the beam.

Increasing the value of  $m_2$  we observe that initially both pendula are in the state of almost-complete synchronization. Fig. 27(b) calculated for  $m_1 = 1.0$  (kg),  $m_2 = 2.0$  (kg) shows pendula's displacements  $\varphi_1 \approx \varphi_2$  and the displacement of the beam  $x$  (for better visibility enlarged 10 times) as a function of time. Notice that the differences  $\varphi_1 - \varphi_2$  are hardly visible.

Further increase of mass  $m_2$  causes the increase of the amplitude of the pendula's oscillations and the increase of the beam oscillations amplitude as can be seen in Fig. 27(d) ( $m_2 = 3.5$  (kg)). One observes also the decrease of the period of the pendulum oscillations (Fig. 27(b) presents 11.25 periods of oscillations while Fig. 27(d) - 12 periods in the same time). This is due to the fact that with increasing the mass of pendulum 2, the center of the mass moves towards the ends of the pendula, i.e., towards the material points with masses  $m_1$  and  $m_2$  and moves away from the beam with constant mass.

Noteworthy is the fact that in a state of complete synchronization, when the displacements of both pendula fulfill the relation  $\varphi_1(t) = \varphi_2(t)$ , the energy transmitted to the beam by each pendulum is proportional to its mass. Therefore these energies satisfy the following equations:

$$\begin{aligned}
 W_1^{SELF} &= \int_0^T c_{\varphi v dp} \dot{\varphi}_1^2 dt = \int_0^T c_{\varphi v dp} \dot{\varphi}_2^2 dt = W_2^{SELF}, \\
 W_1^{VDP} &= \int_0^T c_{\varphi v dp} \zeta \dot{\varphi}_1^2 \varphi_1^2 dt = \int_0^T c_{\varphi v dp} \zeta \dot{\varphi}_2^2 \varphi_2^2 dt = W_2^{VDP}, \\
 W_1^{SYN} &= \int_0^T m_1 \ddot{x} l \cos \varphi_1 \dot{\varphi}_1 dt = \frac{m_1}{m_2} \int_0^T m_2 \ddot{x} l \cos \varphi_2 \dot{\varphi}_2 dt = \frac{m_1}{m_2} W_2^{SYN}.
 \end{aligned} \tag{88}$$

After substituting Eq. (8) into Eqs. (76) and (76) become contradictory (except in the special non-robust case of two identical pendula when  $m_1 = m_2$ ). In the general case when  $m_1 \neq m_2$  instead of complete synchronization we observe occurs almost-complete synchronization, during which pendula's displacements and velocities are almost equal and appropriate energies

satisfy the following equations:

$$\begin{aligned}
 W_1^{DAMP} &= \int_0^T c_\varphi \dot{\varphi}_1^2 dt \approx \int_0^T c_\varphi \dot{\varphi}_2^2 dt = W_2^{DAMP}, \\
 W_1^{SYN} &= \int_0^T m_1 \ddot{x} \cos \varphi_1 \dot{\varphi}_1 dt \approx \int_0^T m_2 \ddot{x} \cos \varphi_2 \dot{\varphi}_2 dt = W_2^{SYN}, \\
 W_1^{SELF} &= \int_0^T c_{\varphi v dp} \dot{\varphi}_1^2 dt \approx \int_0^T c_{\varphi v dp} \dot{\varphi}_2^2 dt = W_2^{SELF}, \\
 W_1^{VDP} &= \int_0^T c_{\varphi v dp} \zeta \dot{\varphi}_1^2 dt \approx \int_0^T c_{\varphi v dp} \zeta \dot{\varphi}_2^2 dt = W_2^{VDP}, \\
 W_1^{SYN} &= \int_0^T m_1 \ddot{x} \cos \varphi_1 \dot{\varphi}_1 dt \approx \int_0^T m_2 \ddot{x} \cos \varphi_2 \dot{\varphi}_2 dt = W_2^{SYN}.
 \end{aligned} \tag{89}$$

After substitution of Eq. (89) the energy equations (76) are satisfied for pendula of different masses. Fig. 27(c) shows the values of all energies as a function of mass  $m_2$ . As one can see, for  $m_2 < 4.0$  (kg) all energies are positive. This means that both pendula transfer the part of their energy to the beam, causing its motion (see Eq. (83)).

For  $m_2 = 4.0$  (kg), the system undergoes bifurcation, an attractor of almost complete synchronized state loses its stability and we observe a jump to the co-existing attractor of almost-antiphase synchronization as shown in Fig. 27(e) ( $m_2 = 5.0$  (kg)). The amplitudes of the pendula's oscillations are different but the phase shift between the pendula is close to  $\pi$  ( $180^\circ$ ). The oscillations of the beam are so small that they are not visible in the scale of Fig. 27(e).

One can show that when one change the mass of pendulum 1 to  $m_1 = 2.0$  (kg),  $m_1 = 3.0$  (kg),  $m_1 = 4.0$  (kg), the bifurcation from almost-complete to almost-antiphase synchronizations occurs respectively for  $m_2 = 3.0$  (kg),  $m_2 = 2.0$  (kg) and  $m_2 = 1.0$  (kg). This bifurcation occurs when the total mass of both pendula reach critical value  $m_{cr} = 5.0$  (kg), which depends on the system parameters, particularly on the beam parameters  $M$ ,  $c_x$  and  $k_x$ .

Fig. 27(f) shows the time series of the beam vibrations and the two pendula oscillations in the case of identical masses  $m_1 = m_2 = 3.0$  (kg) in the state of complete synchronization. These results have been obtained for identical initial conditions, so that they constitute de facto the pendulum of mass  $m = 6.0$  (kg)  $> m_{cr}$ . It is easy to see that this synchronized state is unstable: small disturbances lead to a stable coexisting attractor of antiphase synchronization. Notice that for pendula with slightly different masses (e.g.,  $m_1 = 2.99$  (kg) and  $m_2 = 3.01$  (kg)) it is impossible to obtain a result similar to that shown in Fig. 27(f) even for identical initial conditions. Different pendula's masses cause that initially an almost-complete synchronization is observed but small differences in  $\varphi_1$  and  $\varphi_2$  lead to the stable almost-antiphase synchronization.

Both discontinuous (Eqs. (27) and (28)) and continuous (Eqs. (68) and (69)) models show the same three types of synchronized behavior. The bifurcation diagram of Fig. 26(a) (discontinuous model) shows the existence of: (i) complete synchronization for  $m_1 = m_2 = 1.0$  (kg), (ii) almost complete synchronization for  $1.0 < m_2 < 30.3$  (kg), (iii) almost antiphase synchronization, with one pendulum with turned off escapement mechanism (in Fig. 26(a) pendulum 2 has a turned off mechanism) for  $m_2 > 30.3$  (kg) and the bifurcation diagram of Fig. 27(a) (continuous model) shows: (i) complete for  $m_1 = m_2 = 1.0$  (kg), (ii) almost-complete for  $1.0 < m_2 < 4.0$  (kg), (iii) almost-antiphase for  $m_2 > 4.0$  (kg). The quantitative differences in both models occur due to the possibility of the breakdown of the energy supply in the discontinuous model (switch-off of the escapement mechanism) while in the continuous model energy is supplied permanently.

#### (b) From complete synchronization to quasiperiodic oscillations

The evolution of system (27) and (28) behavior starting from complete synchronization of identical pendula ( $m_1 = m_2 = 1.0$  (kg)) and the decrease of the values of the control parameter  $m_2$  is illustrated in Fig. 28(a)–(d). Fig. 28(a) shows the bifurcation diagram for decreasing values of mass  $m_2$  ( $m_2 \in [0.01, 1.00]$ ). In the interval  $1.0 > m_2 > 0.25$  (kg), both pendula are in a state of almost-complete synchronization. Their oscillations are “almost identical” as can be seen in Fig. 28(b) for  $m_1 = 1.0$  (kg) and  $m_2 = 0.01$  (kg). The differences between the amplitudes and phases of  $\varphi_1$  and  $\varphi_2$  are close to zero, both pendula remain in the (almost) antiphase to the oscillations of the beam. Further reduction of mass  $m_2$  leads to the loss of synchronization and the motion of the system becomes quasiperiodic as shown in Fig. 28(c). Fig. 28(d) presents the Poincare map (the displacements and velocities of the pendula have been taken at the moments of the greatest positive displacement of the first pendulum) for  $m_2 = 0.2$  (kg).

Evolution of system (68) and (69) behavior starting from complete synchronization of identical pendula ( $m_1 = m_2 = 1.0$  (kg)) and decreasing the values of the control parameter  $m_2$  is illustrated in Fig. 29(a)–(d). Fig. 28(a) shows the bifurcation diagram for decreasing values of the mass  $m_2$  ( $m_2 \in [0.01, 1.00]$ ). In the interval  $1.0 > m_2 > 0.0975$ , both pendula are in a state of almost-complete synchronization. Their oscillations are “almost identical” as can be seen in Fig. 29(b) for  $m_1 = 1.0$  (kg) and  $m_2 = 0.01$  (kg), the differences between the amplitudes and phases of  $\varphi_1$  and  $\varphi_2$  are close to zero, both pendula remain in the (almost) antiphase to the oscillations of the beam.

Fig. 29(c) shows the values of different energies. As in the interval  $1.0 < m_2 < 4.0$  (kg) of Fig. 29(c), all energies are positive and both pendula drive the beam  $M$ . Further reduction of mass  $m_2$  leads to the loss of synchronization and the motion of the system becomes quasi-periodic. Fig. 29(d) presents the Poincare map (the displacements and velocities of the pendula have been taken at the moments of greatest positive displacement of the first pendulum) for  $m_2 = 0.07$  (kg). The

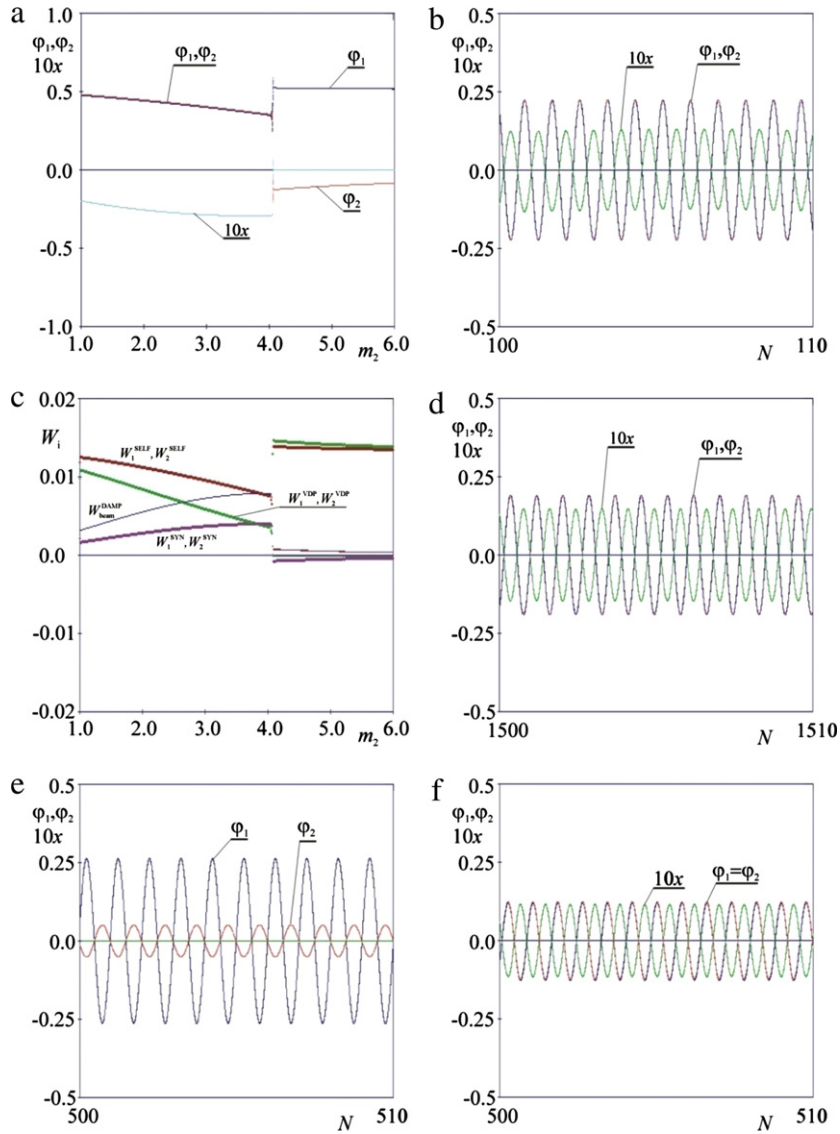


**Fig. 27.** Evolution from complete to almost antiphase synchronization; (a) bifurcation diagram for increasing values of  $m_2$ , (b) time series of almost complete synchronization  $m_1 = 1.0$  (kg) and  $m_2 = 2.0$  (kg); (c) plots of system's energy; (d) time series of almost complete synchronization for  $m_1 = 1.0$  (kg) and  $m_2 = 3.5$  (kg); (e) time series of almost antiphase synchronization:  $m_1 = 1.0$  (kg),  $m_2 = 5.0$  (kg); (f) nonstationary complete synchronization:  $m_1 = m_2 = 3.0$  (kg).

mechanism of the loss of stability is explained in Fig. 29(c). In the interval  $0.35 > m_2 > 0.07$  (kg) the energy dissipated by the first pendulum  $W_1^{VDP}$  approaches the level of the energy supplied by the self-excited component of the this pendulum  $W_1^{SELF}$ . Consequently, the energy  $W_1^{SYN}$  supplied by the first pendulum to the beam decreases. The energy  $W_2^{SELF}$  supplied to the system by the second pendulum also decreases. For  $m_2 < 0.07$  (kg) the energy balance is disrupted: pendulum  $m_2$  has not enough energy to cause its own oscillations, the oscillations of the beam and additionally support the oscillations of the first pendulum. In this case the almost-antiphase synchronization is not possible (see Section 3.5) and the system (68) and (69) exhibits quasiperiodic oscillations.

In this case both discontinuous and continuous models show qualitatively the same behavior but with large quantitative differences. The bifurcation diagram of Fig. 28(a) shows the existence of; (i) complete synchronization for  $m_1 = m_2 = 1.0$  (kg), (ii) almost complete synchronization for  $1.0 > m_2 > 0.0975$  (kg), (iii) the lack of synchronization and quasiperiodic oscillations for  $m_2 < 0.25$  (kg) while the bifurcation diagram of Fig. 29(a) shows the existence of; (i) complete synchronization for  $m_1 = m_2 = 1.0$  (kg), (ii) almost-complete synchronization for  $1.0 > m_2 > 0.0975$  (kg), (iii) the lack of synchronization and quasiperiodic oscillations for  $m_2 < 0.0975$  (kg).

(d) From antiphase to almost-antiphase synchronization

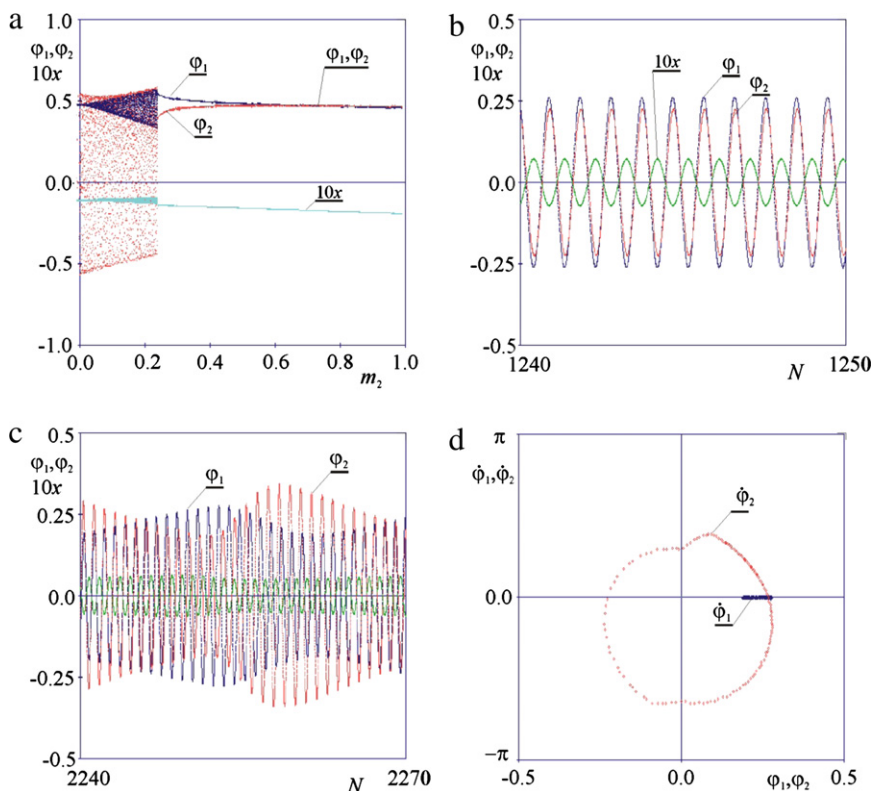


**Fig. 28.** Evolution from complete synchronization to quasiperiodic oscillations; (a) bifurcation diagram for increasing values of  $m_2$ , (b) time series of almost complete synchronization for  $m_1 = 1.0$  (kg) and  $m_2 = 0.3$  (kg), (c) time series of quasiperiodic oscillations for  $m_1 = 1.0$  (kg) and  $m_2 = 0.2$  (kg), (d) Poincaré map showing quasiperiodic oscillations for  $m_1 = 1.0$  (kg) and  $m_2 = 0.2$  (kg).

The evolution of system (27) and (28) behavior starting from antiphase synchronization of identical pendula ( $m_1 = m_2 = 1.0$  (kg)) and the increase of the values of the control parameter  $m_2$  is illustrated in Fig. 30(a)–(c). Fig. 30(a) presents another bifurcation diagram for the increasing values of  $m_2$  ( $m_2 \in [1.0, 41.0]$ ). This time we start with a state of antiphase synchronization of pendula with masses  $m_1 = m_2 = 1.0$  (kg), during which two pendula are moving in the same way, such that  $\varphi_1(t) = -\varphi_2(t)$  and the beam is at rest.

The increase of bifurcation parameter  $m_2$  leads to the increase of the oscillations amplitude of pendulum 1 (with constant mass ( $m_1 = 1.0$  (kg))) and the decrease of the amplitude of pendulum 2 (with increasing mass  $m_2$ ). The pendula remain in the state of almost-complete synchronization as the phase shift between their displacements is close to  $\pi$  ( $180^\circ$ ) as shown in Fig. 30(b) for  $m_1 = 1.0$  (kg) and  $m_2 = 2.0$  (kg). In Fig. 30(b) displacements  $\varphi_1$  and  $\varphi_2$  are almost in antiphase (difference between antiphase and almost antiphase is hardly visible). The beam is oscillating and its displacement  $x$  is shifted by approximately  $\pi/2$  ( $90^\circ$ ) (respectively forward and backward) in relation to the pendula' displacements. The beam oscillations are caused by the energy transmitted to the beam by pendulum 2. Part of this energy is dissipated in the beam damper  $c_x$  and part is transferred to pendulum 1. As the results of this transfer pendulum 1 oscillates with the amplitude larger than initial  $\Phi \approx 15^\circ$  (see discussion in Section 3.4). When mass  $m_2$  reaches the value equal to 4.45 (kg) the amplitude of pendulum 2 oscillations decreases below the critical value  $\Phi \approx \gamma_N = 5^\circ$ . In the interval  $4.45 < m_2 < 5.30$  (kg) the escapement mechanism of pendulum 2 is turned off and we observe quasiperiodic oscillations of the system (27) and (28). The example of quasiperiodic oscillations is shown in Fig. 30(c). There are two irregular phases of these oscillations: (i) after turning off the escapement mechanism of pendulum 2, it does not provide energy to pendulum 1, the amplitude of pendulum 1 oscillations decreases and simultaneously the amplitude of pendulum 2 oscillations increases and its escapement mechanism is turned on, (ii) after switching on of the escapement mechanism of pendulum 2, it provides the energy to pendulum 1, which causes the reduction of pendulum 2 amplitude and leads to the switch off of the escapement mechanism. For  $m_2 > 5.3$  (kg) the escapement mechanism of pendulum 2 is turned off and the system tends to almost antiphase synchronization.

The evolution of system (68) and (69) behavior starting from antiphase synchronization of identical pendula ( $m_1 = m_2 = 1.0$  (kg)) and increasing the values of the control parameter  $m_2$  is illustrated in Fig. 31(a)–(d). Fig. 31(a) presents another bifurcation diagram for the increasing values of  $m_2$  ( $m_2 \in [1.0, 6.0]$ ). We start again with a state of antiphase synchronization of pendula with masses  $m_1 = m_2 = 1.0$  (kg), during which the two pendula are moving in the same way ( $\varphi_1 = -\varphi_2$ ) and the beam is at rest.

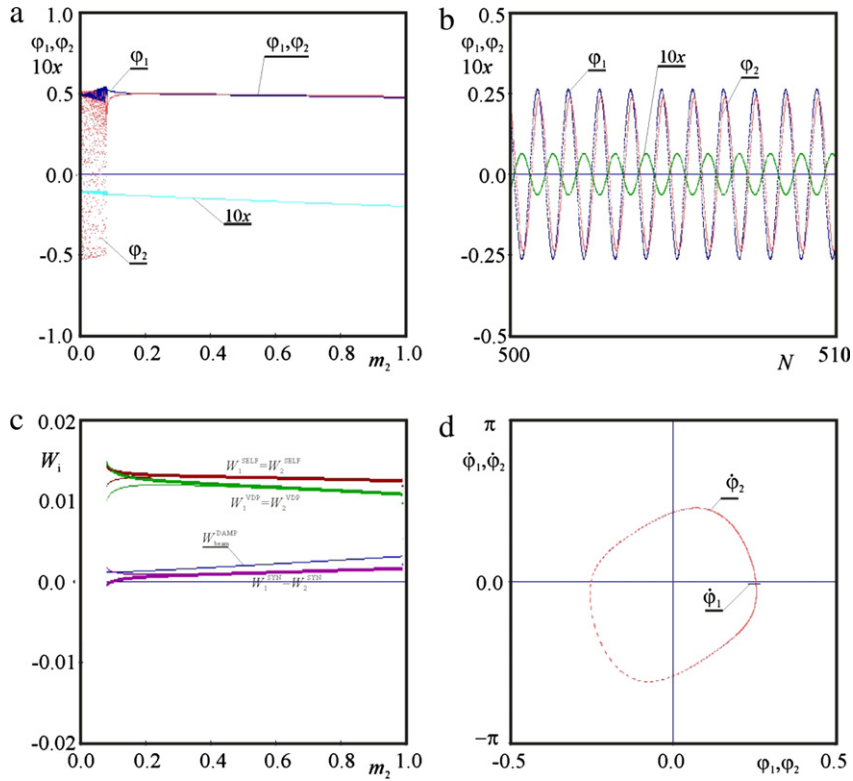


**Fig. 29.** Evolution from complete synchronization to quasiperiodic oscillations; (a) bifurcation diagram for increasing values of  $m_2$ , (b) time series of almost complete synchronization for  $m_1 = 1.0$  (kg) and  $m_2 = 0.1$  (kg), (c) energy plots, (d) Poincare map showing quasiperiodic oscillations for  $m_1 = 1.0$  (kg) and  $m_2 = 0.07$  (kg).

The increase of the control parameter  $m_2$  leads to the reduction of pendulum 2 amplitude of oscillations but the amplitude of oscillations of pendulum 1 remains nearly constant. The pendula remain in a state of almost-phase synchronization: phase shift between the displacements is close to  $\pi$  ( $180^\circ$ ), as shown in Fig. 31(b) ( $m_1 = 1.0$  (kg),  $m_2 = 1.5$  (kg)). The displacement of the beam is practically equal to zero.

In the state of antiphase synchronization when pendula's oscillations satisfy the condition  $\varphi_1(t) = -\varphi_2(t)$ , two van der Pol's dampers dissipate the same amount of energy. The energies transmitted by both pendula to the beam have absolute values proportional to pendula's masses and opposite signs:

$$\begin{aligned}
 W_1^{SELF} &= \int_0^T c_{\varphi vdp} \dot{\varphi}_1^2 dt = \int_0^T c_{\varphi vdp} \dot{\varphi}_2^2 dt = W_2^{SELF}, \\
 W_1^{VDP} &= \int_0^T c_{\varphi vdp} \zeta \dot{\varphi}_1^2 \varphi_1^2 dt = \int_0^T c_{\varphi vdp} \zeta \dot{\varphi}_2^2 \varphi_2^2 dt = W_2^{VDP}, \\
 W_1^{SYN} &= \int_0^T m_1 \ddot{x} \cos \varphi_1 \dot{\varphi}_1 dt = -\frac{m_1}{m_2} \int_0^T m_2 \ddot{x} \cos \varphi_2 \dot{\varphi}_2 dt = -\frac{m_1}{m_2} W_2^{SYN}.
 \end{aligned} \tag{90}$$

After substituting the energy values satisfying Eqs. (90) into Eqs. (76) and (76) are not contradictory equations only when the beam acceleration is zero, which implies the zero value of its velocity and acceleration (in the synchronization state the behavior of the system is periodic). This condition requires balancing of the forces which act on the pendulum beam, and this in turn requires that the pendulum has got the same mass. If the masses of the pendula are different, instead of antiphase synchronization we observe an almost-antiphase synchronization, during which the pendula have different amplitude and the phase shift between them is close, but not equal to  $\pi$  ( $180^\circ$ ). Hence

$$\begin{aligned}
 W_1^{SELF} &\neq W_2^{SELF}, \\
 W_1^{VDP} &\neq W_2^{VDP}, \\
 W_1^{SYN} &\neq W_2^{SYN}.
 \end{aligned} \tag{91}$$

The values of each considered energy are shown in Fig. 31(c). In the state of almost-antiphase synchronization we have  $W_1^{SELF} < W_1^{VDP}$  and  $W_2^{SELF} > W_2^{VDP}$ . Part of the energy  $W_2^{SELF}$  supplied by the van-der-Pol's damper of pendulum 2 (with a

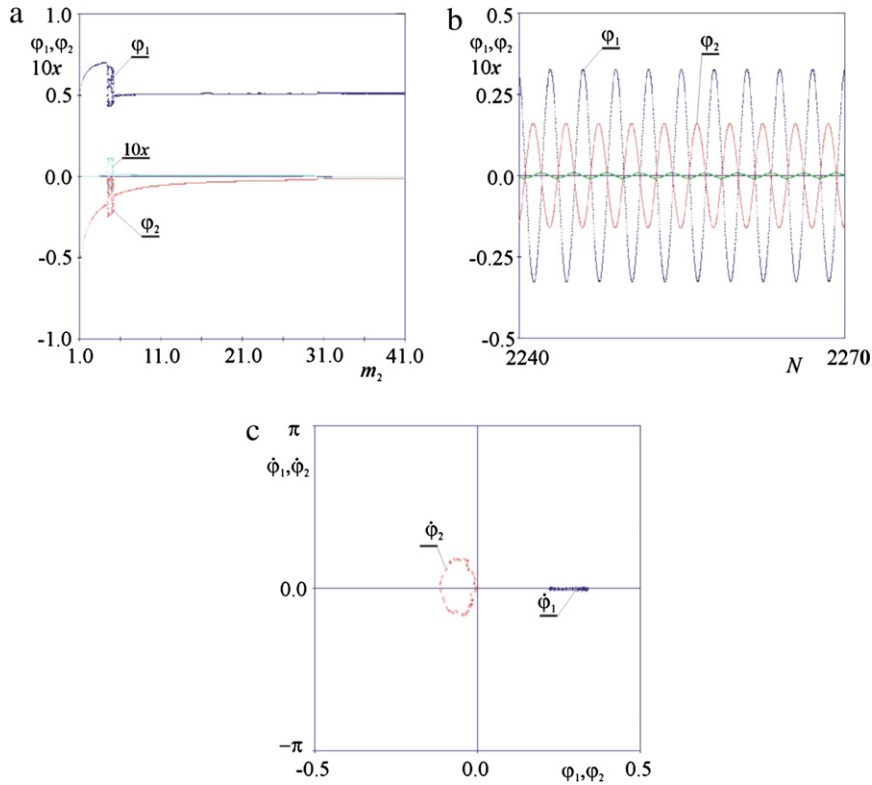


**Fig. 30.** Evolution from antiphase to almost antiphase synchronization; (a) bifurcation diagram for increasing values of  $m_2$ , (b) time series of almost antiphase synchronization for  $m_1 = 1.0$  (kg) and  $m_2 = 2.0$  (kg), (c) Poincare map of quasiperiodic oscillations for  $m_1 = 1.0$  (kg) and  $m_2 = 5.0$  (kg).

greater mass) is transferred via the beam (as  $W_2^{SYN}$ ) to pendulum 1 (for this pendulum it is a negative energy denoted by  $W_1^{SYN}$ ) and together with the energy  $W_1^{SELF}$  dissipated as  $W_1^{VDP}$  by van der Pol damper. Van der Pol's component of pendulum 2 dissipates the rest of the energy  $W_2^{SELF}$ , as  $W_2^{VDP}$ . The energy dissipated by the beam damper is negligibly small, because the beam virtually does not move.

Fig. 31(d) shows the time series of the system oscillations for  $m_2 = 20.0$  (kg). We observe that further increase of  $m_2$  causes the reduction of the amplitude of pendulum 2 oscillations; the amplitude of oscillations of pendulum 1 remains unchanged. It can be observed that when the mass  $m_2$  increases, the equality of forces, with which the pendula act on the beam occurs at decreasing amplitude of oscillations of pendulum 2. Pendulum 1 (with smaller mass) has a virtually constant amplitude of oscillations and works here as the classical dynamical damper.

The comparison of Figs. 27(a) and 31(a) indicates that in the interval  $1.0 < m_2 < 4.0$  (kg) almost-complete and almost-antiphase synchronization coexist (the initial conditions decide about which of them takes place).

The comparison of the discontinuous and continuous models show the quantitative difference as the continuous model does not show quasi-periodic behavior. The bifurcation diagram of Fig. 30(a) shows the existence of: (i) antiphase synchronization for  $m_1 = m_2 = 1.0$  (kg), (ii) almost-antiphase synchronization for  $1.0 < m_2 < 4.45$  (kg), (iii) the lack of synchronization and quasi-periodic oscillations for  $4.45 < m_2 < 5.3$  (kg), (iv) almost-antiphase synchronization with the switch off of the escapement mechanism of pendulum 2 for  $m_2 > 5.3$  (kg) and the diagram shown in Fig. 31(a) shows the existence of: (i) antiphase synchronization for  $m_1 = m_2 = 1.0$  (kg), (ii) almost-antiphase synchronization for  $1.0 < m_2 < 6.0$  (kg) (our research shows that this state is preserved for larger values  $m_2$ ).

#### (e) From antiphase synchronization to quasiperiodic oscillations

The evolution of system (27) and (28) behavior starting from antiphase synchronization of identical pendula ( $m_1 = m_2 = 1.0$  (kg)) and the decrease of the values of the control parameter  $m_2$  is illustrated in Fig. 32(a, b). Fig. 32(a) shows the bifurcation diagram of the system (27) and (28) for decreasing values of  $m_2$  ( $m_2$  decreases from an initial value 1.0 (kg) up to 0.01 (kg)). We start from the state of antiphase synchronization observed for  $m_1 = m_2 = 1.0$  (kg). In the interval  $1.0 > m_2 > 0.38$  (kg) both pendula are in the state of almost antiphase synchronization. Their displacements are out of phase by an angle close to  $180^\circ$  as shown in Fig. 32(b) showing the time series of  $\phi_1$ ,  $\phi_2$  and  $x$  for  $m_1 = 1.0$  (kg) and  $m_2 = 0.5$  (kg). When mass  $m_2$  decreases from 1.0 (kg) to 0.56 (kg), the amplitude of oscillations of pendulum 1 decreases and the amplitude of oscillations of pendulum 2 increases. In the interval  $0.56 > m_2 > 0.38$  (kg) we observe a fast decrease of pendulum 2 amplitude up to the limit value  $\phi \approx \gamma_N = 5^\circ$ . For  $m_2 = 0.38$  (kg) system (27) and (28) changes the

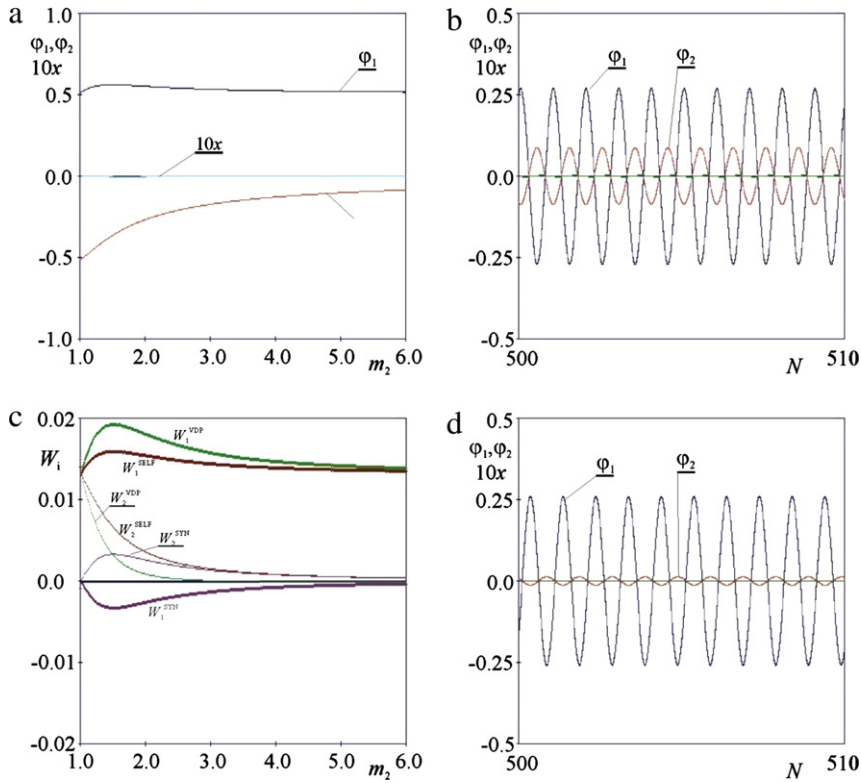


**Fig. 31.** Evolution from antiphase to almost antiphase synchronization; (a) bifurcation diagram for increasing values of  $m_2$ , (b) time series of almost antiphase synchronization for  $m_1 = 1.0$  (kg) and  $m_2 = 1.5$  (kg), (c) energy plots, (d) time series of almost antiphase synchronization for  $m_1 = 1.0$  (kg) and  $m_2 = 20.0$  (kg).

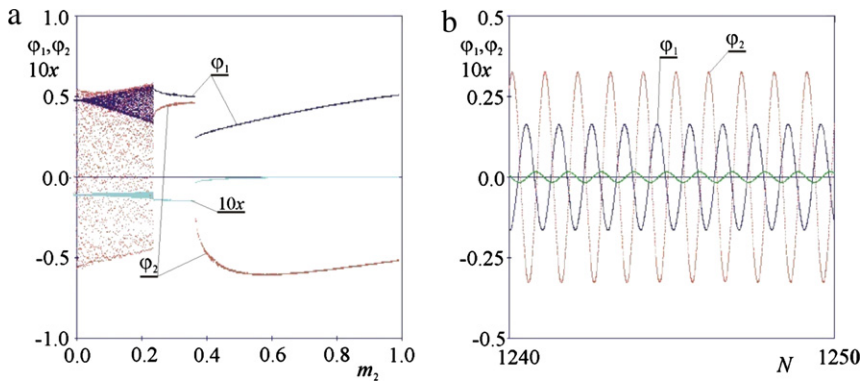


**Fig. 32.** Evolution from antiphase synchronization to quasiperiodic oscillations; (a) bifurcation diagram of system (27) and (28) for decreasing  $m_2$ , (b) time series of almost antiphase synchronization for  $m_1 = 1.0$  (kg),  $m_2 = 0.5$  (kg).

type of the synchronization to almost complete (previously observed in Fig. 28(a, b)). Further reduction of  $m_2$  leads to the quasi-periodic motion of the system (as described in Section b).

The evolution of system (68) and (69) behavior starting from antiphase synchronization of identical pendula ( $m_1 = m_2 = 1.0$  (kg)) and decreasing the values of the control parameter  $m_2$  are illustrated in Fig. 33(a)–(d). Fig. 33(a) shows the bifurcation diagram of the system (68) and (69) for decreasing values of  $m_2$  ( $m_2$  decreases from an initial value 1.0 up to 0.01). We start from the state of antiphase synchronization observed for  $m_1 = m_2 = 1.0$  (kg). In the interval  $1.0 > m_2 > 0.45$  (kg), both pendula are in the state of almost-antiphase synchronization, as shown in Fig. 33(b) for  $m_2 = 0.5$  (kg). We observe a phenomenon similar to that of Fig. 31(a), i.e., when decreasing mass  $m_2$ , the amplitude of oscillations of pendulum 1 decreases (in this case pendulum 1 has larger mass), the amplitude of pendulum 2 oscillations is practically constant and pendulum 2 acts as a dynamical damper. In Fig. 33(c) one can see the negative energy  $W_2^{\text{SYN}}$ —there is a transfer of energy from pendulum 1 to pendulum 2.

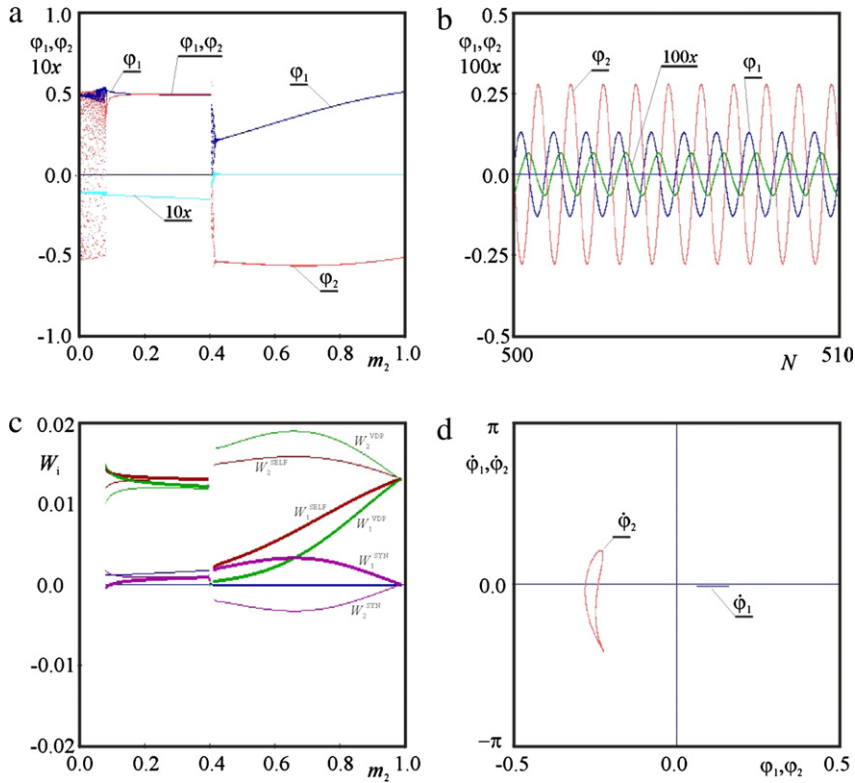


**Fig. 33.** Evolution from antiphase synchronization to quasiperiodic oscillations; (a) Bifurcation diagram of system (68) and (69) for decreasing  $m_2$ , (b) time series of almost antiphase synchronization for  $m_1 = 1.0$ ,  $m_2 = 0.5$ , (c) energy plots, (d) Poincare maps showing quasiperiodic oscillations for  $m_1 = 1.0$  (kg) and  $m_2 = 0.44$  (kg).

For  $m_2 = 0.45$  (kg) we observe the loss of synchronization due to the fact that energy  $W_1^{\text{SELF}}$  becomes equal to energy  $W_1^{\text{SYN}}$  which means that all the energy supplied to pendulum 1 by van der Pol's damper is transmitted to pendulum 2 via the beam. For smaller values of  $m_2$ , pendulum 2 is not able to supply the energy needed to maintain a state of almost-antiphase synchronization and the systems first obtains the state of almost-complete synchronization, and next when  $m_2 < 0.095$  (kg) exhibits unsynchronized quasi-periodic oscillations. The behavior of the system for  $m_2 < 0.415$  (kg) has been described in Section 4.2.2(b).

In the narrow interval between the state of almost antiphase and the state of almost-complete synchronization, i.e., for  $0.45 > m_2 > 0.415$  (kg) we observe quasiperiodic oscillations of the system, as shown on the Poincare map of Fig. 33(d) ( $m_2 = 0.44$  (kg)).

The bifurcation diagram of Fig. 32(a) shows the existence of: (i) antiphase synchronization for  $m_1 = m_2 = 1.0$  (kg), (ii) almost antiphase synchronization for  $1.0 > m_2 > 0.38$  (kg), (iii) almost complete synchronization for  $0.38 > m_2 > 0.25$  (kg), (iv) the lack of synchronization and quasiperiodic oscillations for  $m_2 < 0.25$  (kg) and the bifurcation diagram of Fig. 33(a) shows the existence of: (i) antiphase synchronization for  $m_1 = m_2 = 1.0$  (kg), (ii) almost-antiphase synchronization for  $1.0 > m_2 > 0.45$  (kg), (iii) the lack of synchronization and a quasi-periodic oscillations for  $0.45 > m_2 > 0.415$  (kg), (iv) almost-complete synchronization for  $0.415 > m_2 > 0.095$ , (v) the lack of synchronization and quasi-periodic oscillations for  $m_2 < 0.095$  (kg).

#### 4.2.3. Synchronization of two pendula with different lengths

This section presents our results obtained for the case of clock's pendula with the same mass but different lengths. In numerical calculations we consider the following parameter values. The first pendulum is characterized by:  $m = 1.0$  (kg),  $l_1 = g/4\pi^2 = 0.2485$  (m) (i.e., in the case when the beam is at rest its period of free oscillations is equal to  $T_0 = 1$  (s) and its frequency is equal to  $\alpha_{10} = 2\pi$ ;  $g = 9.81$  (m/s<sup>2</sup>),  $c_{\varphi_1} = 0.01$  (N s m),  $M_{N1} = 0.075$  (N m),  $\gamma_N = 5^\circ$ . When the beam is at rest the pendulums perform the oscillations with amplitude  $\Phi_{10} \approx 15^\circ$ . The second pendulum has the same mass  $m$  and  $\gamma_N$ . Its length is equal to  $l_2 = \xi^2 l_1$  (i.e.,  $\alpha_2 = \alpha_1/\xi$  and  $T_{20} = \xi T_{10}$ ) and  $c_{\varphi_2} = \xi c_{\varphi_1}$ ,  $M_{N2} = \xi M_{N1}$ . The coefficient  $\xi$  is called the scale factor of the second pendulum. The proportionality of the damping coefficients and escapement mechanisms' moments of both pendula result in the equality of the amplitudes  $\Phi_{20} = \Phi_{10}$ . In Fig. 34 we show the oscillations  $\varphi_1$  and  $\varphi_2$  of pendula 1 (thick line) and 2 (thin line) suspended on nonmoving beam versus time represented by the number of oscillation periods of the first pendulum  $N$ .

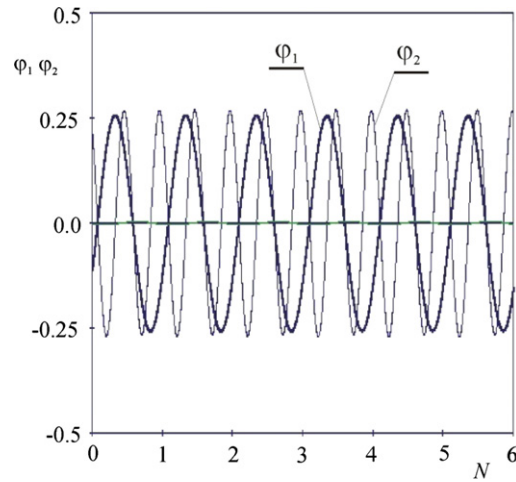


Fig. 34. Oscillations of two pendula:  $\xi = 0.5$ .

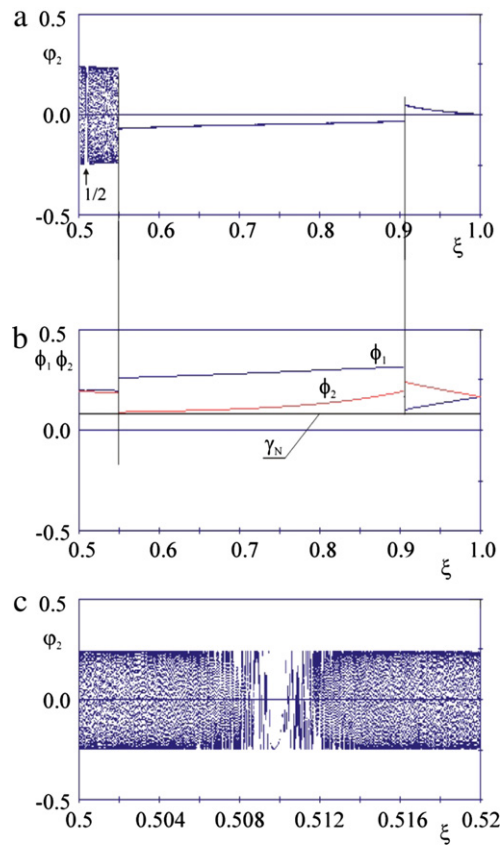
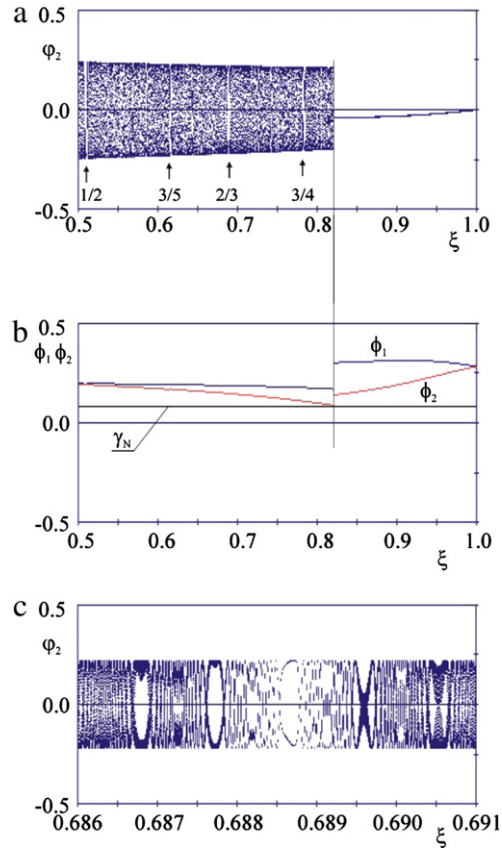


Fig. 35. (a) Bifurcation diagram of system (27) and (28) for decreasing  $\xi$ ; (bifurcation diagram: starts with  $\xi = 1.0$  and  $\varphi_{10} = \varphi_{20} = 0.26$  and ends with  $\xi = 0.5$ ), (b) minima of amplitudes of pendula's oscillations, (c) enlargement of (a) in the neighborhood of synchronization  $1/2$ .

As  $\xi = 0.5$  one can observe that  $T_{20} = 0.5T_{10}$  and that the amplitudes of both pendula are the same. Beam's parameters are as follows: its mass is assumed to be  $M = 5.0$ , the stiffness  $k_x$  and damping coefficients  $c_x$  are related to the beam mass, i.e.,  $k_x = 0.1M$ ,  $c_x = M$ .

Figs.(a) and 36(a) show respectively the bifurcation diagrams of the system (27) and (28) calculated for decreasing and increasing values of  $\xi$ . In Fig. 37(a)–(f) the time series of characteristic system behavior are presented.



**Fig. 36.** (a) Bifurcation diagram of system (27) and (28) for increasing  $\xi$ ; (bifurcation diagram: starts with  $\xi = 0.5$  and  $\varphi_{10} = \varphi_{20} = 0.26$  and ends with  $\xi = 1.0$ ) (b) minima of amplitudes of pendula's oscillations; (c) enlargement of (a) in the neighborhood of synchronization  $2/3$ .

In the bifurcation diagrams the position  $\varphi_2$  of pendulum 2 (registered at the moment when pendulum 1 passes through 0 with a positive velocity ( $\varphi_1 = 0.0, \dot{\varphi}_1 > 0.0$ )) is plotted versus  $\xi$  parameter. The calculations presented in Fig. 35(a) started at  $\xi = 1.0$  (i.e., identical pendula) and the following initial conditions  $x_0 = 0.0, v_0 = 0.0, \varphi_{10} = 0.26, \dot{\varphi}_{10} = 0.0, \varphi_{20} = 0.26, \dot{\varphi}_{20} = 0.0$  for which the system is in a state of in-phase synchronization shown in Fig. 37(a). Next, the value of  $\xi$  has been reduced by the step  $\Delta\xi = 0.00125$  up to  $\xi = 0.5$ . With the decrease of  $\xi$  (i.e., the shortening of the length of pendulum 2), in-phase synchronization persists till  $\xi = 0.92$ . Fig. 37(a) presents the example of 1 : 1 in-phase synchronization for  $\xi = 0.95$ . Both pendula are moving in the anti-phase to the motion of the beam so their periods of oscillations decrease  $T_1 < T_{10}$  and  $T_2 < T_{20}$ . The differences of the values of the amplitudes of both pendula cause that  $T_{10} - T_1 > T_{20} - T_2$  and after the transient the systems reach common value  $T = 0.84$ .

For the smaller values of  $\xi$  one observes the transition to anti-phase synchronization shown in Fig. 37(b). This type of behavior is preserved up to  $\xi = 0.55$ . Notice that for  $\xi = 0.55$  the ratio of the lengths of both pendula is equal to  $l_2/l_1 = \xi^2 = 0.3025$  (i.e., the triple difference in the lengths). In Fig. 37(b) an example of anti-phase 1 : 1 synchronization obtained for  $\xi = 0.92$  is shown. Pendulum 1 moves in anti-phase with the motion of the beam and its period decreases ( $T_1 < T_{10}$ ) while pendulum 2 moves in phase with the beam motion and its period increases ( $T_2 > T_{20}$ ). After an initial transient the periods of oscillations reach the common value  $T_{20} < T = 0.98 < T_{10}$ .

With further increase of the values of  $\xi$  in the interval  $0.55 > \xi > 0.51$  one observes the quasiperiodic behavior. In this interval the desynchronization of both pendula occurs. The example of quasiperiodic behavior for  $\xi = 0.6871$  is shown in Fig. 37(c, d). Time series of the system (27) and (28) are shown in Fig. 37(c) and the Poincaré map showing the position of pendulum 2 at the time when pendulum 1 is moving through zero with positive velocity is presented in Fig. 37(d). The closed curve at the Poincaré map confirms that the behavior is quasiperiodic. The subsequent change in the pendula' configuration leads to 1 : 2 synchronization explained in Fig. 37(e). Fig. 37(e) shows the synchronization obtained by doubling the period of pendulum 2 ( $\xi = 0.51$ ). Common period of pendula's oscillations is equal to the period of pendulum 1 –  $T_1$  and two periods of pendulum 2, i.e.,  $T = T_1 = 2T_2 = 0.94$ . Noteworthy is the fact that in the case of nonmoving beam this synchronization will occur for  $\xi = 0.5 = 1/2$  and  $T_1 = 2T_2$ . In the case of oscillating beam this transition is shifted (from  $\xi = 0.50$  to  $\xi = 0.51$ ) as due to the different pendula's displacements  $\varphi_1 \neq \varphi_2$  and their different lengths  $l_1 \neq l_2$  the resultant of the forces with which the pendula act on the beam is not always equal to zero. Fig. 35(b) explains why different types of synchronization are visible along the bifurcation diagram in Fig. 35(a). The amplitudes of both pendula  $\Phi_1$  and  $\Phi_2$  versus

coefficient  $\xi$  are shown together with the value of the operations angle of the escapement mechanism  $\gamma_N$ . Notice that for  $\xi = 0.92$ , when the in-phase 1 : 1 synchronization is replaced by the anti-phase 1 : 1 synchronization, the amplitude of pendulum 1  $\Phi_1$  decreases to the value equal to  $\gamma_N$ . With further decrease of  $\xi$  the escapement mechanism of pendulum 1 does not operate and the amplitude  $\Phi_1$  decreases due to the damping  $c_{\varphi_1}$ . The escapement mechanism starts to operate again due to the large amplitude difference and the system reach anti-phase 1 : 1 synchronization. With further decrease of  $\xi$  the amplitude of pendulum 2  $\Phi_2$  decreases up to the critical value  $\gamma_N$  ( $\xi = 0.55$ ) when the escapement mechanism of this pendulum is switched off. The perturbation which results from this switched off desynchronize pendula. For smaller values of  $\xi$ , one observes quasiperiodic behavior. In this case the values of  $\Phi_1$  and  $\Phi_2$  are not constant for given  $\xi$ , so Fig. 35(b) shows their minimum values. As both minimum values of  $\Phi_1$  and  $\Phi_2$  are nearly twice larger than the value of  $\gamma_N$  the escapement mechanisms of both pendula are not switched off during the quasiperiodic behavior. Fig. 35(c) shows the enlarged part of the diagram of Fig. 35(a). Synchronization 1 : 2 is visible on it as a single line of  $\varphi_2$  in the interval  $0.51 > \xi > 0.5095$ . The length of this interval is equal to  $\Delta\xi = 0.0005$ , i.e., the given length of pendulum 1, say  $l_1 \approx 0.25$  (m) the length of pendulum 2 can change only by 0.0001 (m), so the practical importance of this synchronization is rather low. In the last considered interval  $0.5095 > \xi > 0.5$  the system (27) and (28) shows quasiperiodic behavior. With further decrease of  $\xi$  one can observe the 1/3 synchronization (not shown in Fig. 35(a)) for  $\xi = 0.3375$ . In this case the oscillation period common for both pendula  $T$  is equal to the period of pendulum 1  $T_1$  and three periods of pendulum 2  $T_2$ , i.e.,  $T = T_1 = 3T_2$ .

Fig. 36(a)–(c) shows the bifurcation diagram calculated for the increasing values of  $\xi$  (from 0.5 to 1.0). Differently to the case of decreasing  $\xi$ , the interval of quasiperiodic behavior is larger as can be seen in Fig. 36(a). Such a behavior exists for  $0.5 < \xi < 0.82$  so in the interval  $0.55 < \xi < 0.82$  one can observe two co-existing attractors; periodic (1 : 1 anti-phase synchronization) and quasiperiodic one. The quasiperiodic interval is characterized by the periodic windows, for example these visible for  $\xi = 0.68875$  ( $\approx 2/3$ ),  $\xi = 0.6168$  ( $\approx 3/5$ ),  $\xi = 0.783$  ( $\approx 3/4$ ). Fig. 36(b) allows the determination of the moments when the escapement mechanism is switched off. For the quasiperiodic behavior in the interval  $0.5 < \xi < 0.82$  the minimum values of  $\Phi_1$  and  $\Phi_2$  are larger than  $\gamma_N$  so the mechanism is not switched off. With the decrease of  $\xi$  the amplitude of pendulum 2 decreases and is equal to  $\gamma_N$  for  $\xi = 0.82$ . For further increase of  $\xi$  the escapement mechanism of pendulum 2 is switched off, the quasiperiodic behavior is perturbed and the regime of anti-phase 1 : 1 synchronization is achieved. Fig. 36(c) shows the enlargement of the part of bifurcation diagram of Fig. 36(a). In the interval  $0.6885 < \xi < 0.6888$  one observes 2 : 3 synchronization. This type of synchronization has been achieved by the doubling of the period of pendulum 1  $T_1$  and tripling the period of pendulum 2 –  $T_2$ . The time series characteristic for this behavior are shown in Fig. 37(f) ( $\xi = 0.6887$ ). The period of oscillations common for both pendula is equal to  $T = 2T_1 = 3T_2 = 1.91$  (s). For  $\xi = 0.783$  we observe 3 : 4 synchronization and for  $\xi = 0.6158$  3 : 5 synchronization. All these synchronized regimes exist in the very narrow intervals of  $\xi$ .

The bifurcation diagrams of Figs. 43(a)–(c) and 44(a)–(c) show the existence of two different attractors for some  $\xi$ -intervals. For  $1.0 > \xi > 0.92$  one can observe 1 : 1 in-phase and 1 : 1 anti-phase synchronization, and for  $0.82 > \xi > 0.55$  1 : 1 anti-phase synchronization and quasiperiodic behavior (or 1 : 2, 2 : 3, 3 : 4, ... synchronization in the narrow windows).

The question how the co-existing attractors are sensitive to the external perturbations cannot be generally answered as both phase and parameter spaces of the system are high-dimensional. We partially deal with this problem by performing the following experiment. Having assume that the system is operating on one of the coexisting attractors we perturb the state of pendulum 2 and observe to which attractor the system will approach. Such a procedure allows the estimation of the basins of attraction of the coexisting attractors shown in Fig. 38(a)–(c).

The perturbation of the state of pendulum 2 means the change of its position to the new state given by  $\varphi_{20}$  and  $\dot{\varphi}_{20}$ . Other system parameters, i.e.,  $\varphi_1$ ,  $\dot{\varphi}_1$ ,  $x$  and,  $\dot{x}$  are not changed at the moment of perturbation. Then the system (1) performs the transient evolution which leads to one of the coexisting attractors. Notice that such perturbation can influence the acting of the escapement mechanism. If in the moment of perturbation the mechanism is in the first stage (see eq. Section 2.2) and new value of  $\varphi_{20}$  is larger than  $\gamma_N$ , the mechanism moves to step 2. When in the unperturbed state the mechanism is in step 2 and new value of  $\varphi_{20}$  is smaller than  $-\gamma_N$ , the mechanism goes to step 1. For other cases the perturbation has no influence on the acting of the escapement mechanism.

In the example presented in Fig. 38(a) we assume that system (1) performs 1 : 1 in-phase synchronization for  $\xi = 0.95$  (the coexisting attractor is anti-phase 1 : 1 synchronization). When the system has been in the state given by:  $\varphi_1 = 0.0$ ,  $\dot{\varphi}_1 = 0.9616$ ,  $\varphi_2 = 0.01808$ ,  $\dot{\varphi}_2 = 1.4945$ ,  $x = -0.001635$ ,  $\dot{x} = -0.080947$  pendulum 2 has been perturbed to the state given by  $(\varphi_{20}, \dot{\varphi}_{20})$ . The initial perturbations  $(\varphi_{20}, \dot{\varphi}_{20})$  after which system (27) and (28) returns to 1 : 1 in-phase synchronization are shown in navy blue and these after which the system goes to anti-phase 1 : 1 synchronization are shown in blue.

Fig. 38(b) presents the results obtained for  $\xi = 0.95$  and the initial state given by  $\varphi_1 = 0.0$ ,  $\dot{\varphi}_1 = 1.9525$ ,  $\varphi_2 = -0.0207$ ,  $\dot{\varphi}_2 = -1.48$ ,  $x = -0.000267$ ,  $\dot{x} = -0.0221$ , i.e., the system has been on the 1 : 1 anti-phase synchronization attractor at the moment of perturbation. The basins of in-phase and anti-phase synchronization are shown respectively in navy and blue.

For  $\xi = 0.6887$  system (1) has two attractors; 1 : 1 anti-phase and 2 : 3 synchronization (see Fig. 38(c)). In the time of perturbation the system has been in the state:  $\varphi_1 = 0.0$ ,  $\dot{\varphi}_1 = 1.8385$ ,  $\varphi_2 = -0.05257$ ,  $\dot{\varphi}_2 = -0.558$ ,  $x = 0.00004$ ,  $\dot{x} = -0.0559$  exhibiting 1 : 1 anti-phase synchronization. The basins of 1 : 1 anti-phase and 2 : 3 synchronization are shown respectively in blue and red in Fig. 38(c).

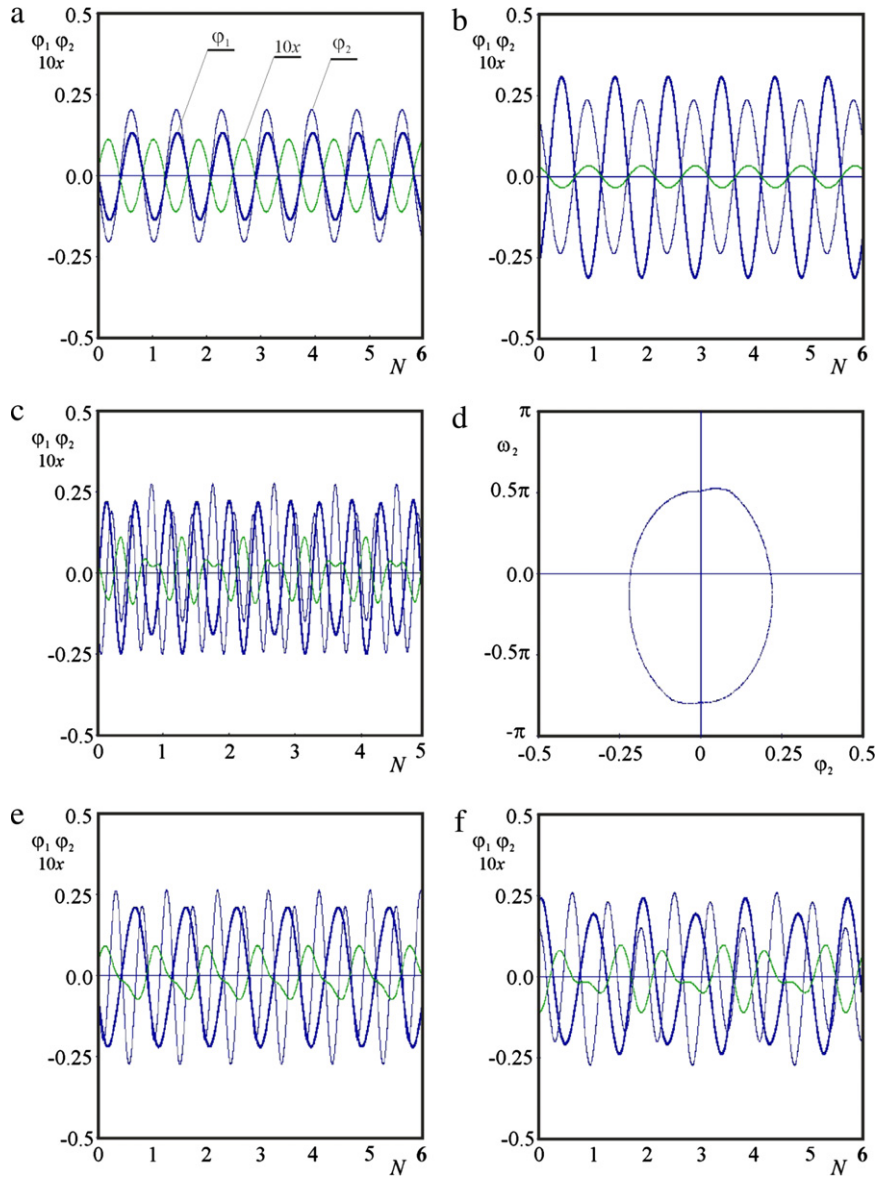


**Fig. 37.** Different types of synchronization of the clock pendula; (a) in-phase synchronization 1/1 for  $\xi = 0.95$ ; (b) antiphase synchronization 1/1 for  $\xi = 0.95$ ; (c) time series of quasiperiodic oscillations for  $\xi = 0.6871$ , (d) Poincaré map for  $\xi = 0.6871$ , (e) synchronization 1/2 for  $\xi = 0.51$ ; (f) synchronization 2/3 for  $\xi = 0.6887$ .

#### 4.2.4. Chaos in the coupled clocks

In this section we give evidence that the pendula of two coupled clocks can exhibit robust chaos. Let us return to the system of Section 4.2.2(i), i.e., the pendula with the same length but different masses. In our numerical simulations equations (27) and (28) have been integrated by the 4th-order Runge–Kutta method adopted for the discontinuous systems (the integration step has been decreased when the trajectory has been approaching discontinuity at  $\varphi_i \pm \gamma_N$ ). The initial conditions have been set as follow; (i) for the beam  $x(0) = \dot{x}(0) = 0$ , (ii) for the pendula the initial conditions  $\varphi_1(0)$ ,  $\dot{\varphi}_1(0)$  have been calculated from the assumed initial phases  $\beta_{10}$  and  $\beta_{20}$ , i.e.,  $\varphi_1(0) = \Phi \sin \beta_{10}$ ,  $\dot{\varphi}_1(0) = \alpha \Phi \cos \beta_{10}$ ,  $\varphi_2(0) = \Phi \sin \beta_{20}$ ,  $\dot{\varphi}_2(0) = \alpha \Phi \cos \beta_{20}$ , where  $\Phi$  and  $\alpha = 2\pi/T$  are respectively the amplitude and the frequency of the pendula when the beam  $M$  is at rest. We consider the following parameter values:  $\gamma_N = 5.0^\circ$ ,  $l = g/4\pi^2 = 0.2485$  (m),  $M = 10.0$  (kg),  $m_1 = 1$  (kg),  $c_x = 1.53$  (N s/m),  $k_x = 3.94$  (N/m),  $c_{\varphi_1} = 0.0083 \times m_1$  (N s),  $c_{\varphi_2} = 0.0083 \times m_2$  (N s),  $M_{N1} = 0.075 \times m_1$  (N m),  $M_{N2} = 0.075 \times m_2$  (N m) and  $m_2 \in [3.10, 4.27]$ , for which system (27) and (28) exhibits the coexistence of (CS), (LPS) and chaotic behavior.

In Fig. 39(a)–(d) we show Poincaré maps for typical periodic and chaotic solutions. We plot position  $\varphi_2$  and velocity  $\dot{\varphi}_2$  of the second pendulum when the first pendulum has zero velocity  $\dot{\varphi}_1 = 0$  and changes its sign from positive to negative.

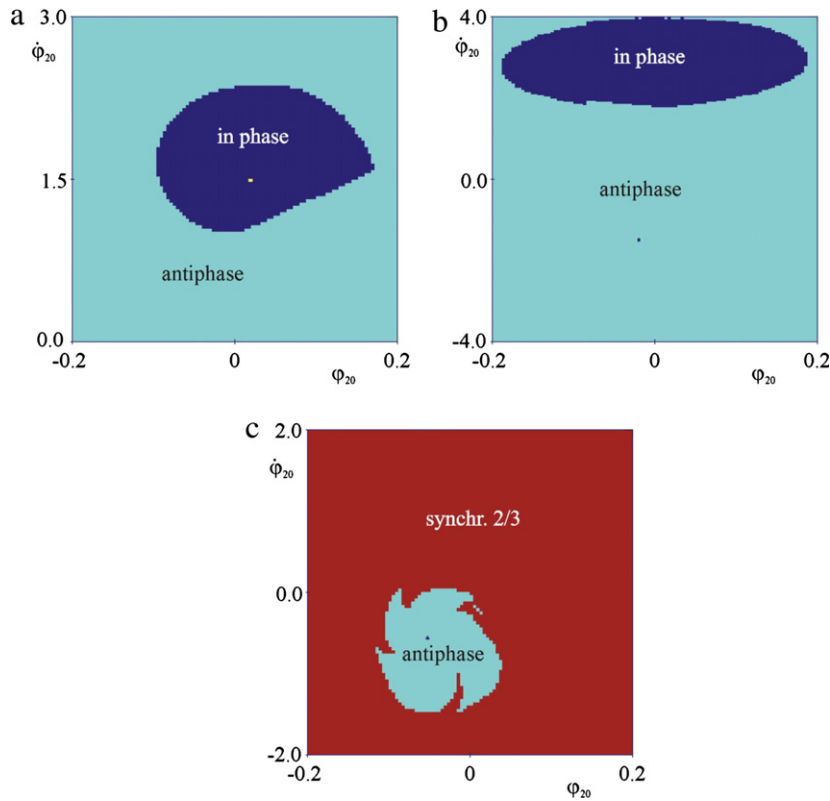


**Fig. 38.** Basins of attraction of the coexisting attractors: (a)  $\xi = 0.95$ ; (b)  $\xi = 0.96$ , (c)  $\xi = 0.6887$ .

The examples of (LPS) with periods  $6T$ ,  $35T$  and  $59T$  are shown in Fig. 39(a)–(c) and Fig. 39(d) presents chaotic behavior. The pendulum trajectory of Fig. 39(d) is characterized by the largest Lyapunov exponent equal to 0.127. As Eqs. (27) and (28) are discontinuous one cannot directly calculate the largest Lyapunov exponent from the linearized dynamics around the trajectory so we adapted the synchronization method described in [104,105]. These calculations confirm that the coupled clocks can exhibit chaotic behavior.

Next for a given value of  $m_2$  we consider the influence of the escapement mechanism parameters ( $\gamma_N$  and  $M_N$ ) on the behavior of clocks' pendula. We assume that the energy supplied to the system is the same in all cases, i.e., the product of  $\gamma_N M_N$  is constant, so when we change  $\gamma_N$  we also recalculate  $M_N$ . Notice that in the case of identical clocks (pendula with the same masses) one can observe only two states: in-phase motion (complete synchronization (CS)) and anti-phase motion (phase synchronization (PS) with the phase shift equal to  $\pi$ ). Recall Fig. 21(c) showing a typical basin of attraction for identical clocks. Navy blue and yellow colors indicate (CS) and (PS) synchronizations respectively. When we take the close values of initial phases the system tends to complete in-phase synchronization. This tendency is not significantly changed for nonidentical clocks (even with the large differences in pendula's masses). When the clocks are nonidentical they cannot exhibit antiphase synchronizations. In the initial conditions' domain in which identical clocks show antiphase synchronization (yellow in Fig. 21(c)) one observes the coexistence of (PS), (LPS) synchronizations and chaotic motion of pendula. Fig. 40(a)–(f) shows the basins of attraction for  $m_2 = 3.105$  (kg) and six different values of escapement mechanism parameter  $\gamma_N$  ( $\gamma_N = 4.5^\circ$  (a);  $\gamma_N = 4.8^\circ$  (b);  $\gamma_N = 5.0^\circ$  (c);  $\gamma_N = 5.05^\circ$  (d);  $\gamma_N = 5.1^\circ$  (e);  $\gamma_N = 5.2^\circ$  (f)). The numbers on the basins indicate the period of the (LPS) and (C) denotes the chaotic behavior. One can see the main range – period 1 (CS) synchronization remains the same in all six cases, so when the initial conditions of both pendula are close to each other, then the parameters of the escapement mechanism have no influence on the pendula's dynamics. For larger differences in initial conditions one can observe (LPS) with different periods (in the range from  $6T$  to  $59T$ ) and chaotic behavior. As it has been already mentioned all these phenomena are observed in the range of anti-phase synchronization observed for identical masses of both pendula (see Fig. 21(c)). In Fig. 40(a) one can observe the coexistence of  $11T$  and  $23T$ ,  $11T$  remains unchanged up to  $\gamma_N = 5.2$ , then in Fig. 48(b)  $6T$  appears. In Fig. 40(c)  $6T$  attractor is dominant, then for  $\gamma_N = 5.05$   $6T$  disappears and  $12T$  (possible period doubling bifurcation of  $6T$ ),  $30T$  and chaos (C) can be observed (Fig. 40(d)). Then for  $\gamma_N = 5.05$  (Fig. 40(e)) all previous states are replaced by  $59T$  (LPS). In Fig. 40(f) two new LPS ranges appear:  $13T$  (replacing  $11T$ ) and  $35T$ . The largest Lyapunov exponent of the chaotic attractors presented in Fig. 40(a)–(f) varies between 0.095 and 0.125. Most of (LPS) and (C) basins are small open sets of escapement mechanism parameters (practically small perturbation leads to their disappearance and the system jumps to another coexisting attractor).

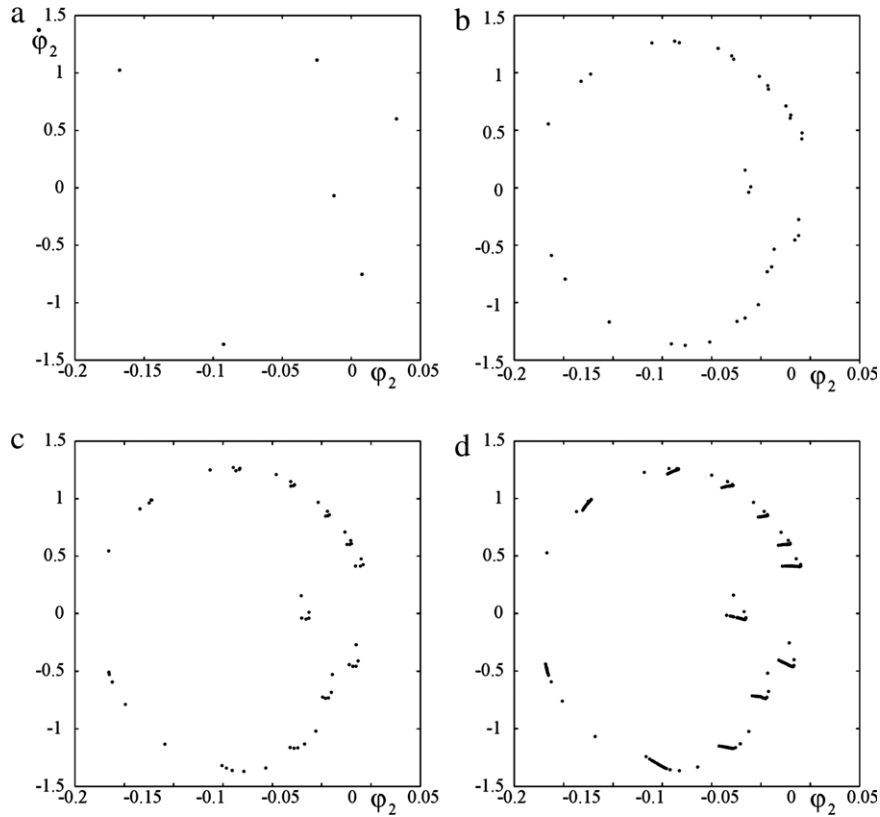


**Fig. 39.** Poincaré maps ( $\varphi_2, \dot{\varphi}_2$ ) for different (LPS) and chaotic attractors;  $m_1 = 1.0$  (kg),  $m_2 = 3.105$  (kg),  $l = g/4\pi^2 = 0.2485$  (m),  $M = 10.0$  (kg),  $c_x = 1.53$  (N s/m),  $k_x = 3.94$  (N/m),  $c_{\varphi_1} = 0.0083 \times m_1$  (N s m),  $c_{\varphi_2} = 0.0083 \times m_2$  (N s),  $M_{N1} = 0.075 \times m_1$  (N m),  $M_{N2} = 0.075 \times m_2$  (N m): (a)  $\gamma_N = 4.9^\circ$ ,  $T = 6$ , (b)  $\gamma_N = 5.2^\circ$ ,  $T = 35$ , (c),  $\gamma_N = 5.1^\circ$ ,  $T = 59$ , (d)  $\gamma_N = 4.9^\circ$ , chaotic behavior.

**Table 2**

Synchronous states observed in two coupled clocks.

Identical pendula	<ul style="list-style-type: none"> <li>– Complete synchronization: <math>\varphi_1(t) = \varphi_2(t)</math>, <math>\varphi_1(t) - \varphi_2(t) = 0</math></li> <li>– Antiphase synchronization: <math>\varphi_1(t) = -\varphi_2(t)</math>, <math>\varphi_1(t) - \varphi_2(t) = \pi</math></li> </ul>
Nonidentical pendula	<ul style="list-style-type: none"> <li>– Almost complete synchronization: the phase shift between <math>\varphi_1(t)</math> and <math>\varphi_2(t)</math> is close to zero (if <math>l_1 = l_2</math> then <math>\varphi_1(t) \approx \varphi_2(t)</math>)</li> <li>– Almost antiphase synchronization: the phase shift between <math>\varphi_1(t)</math> and <math>\varphi_2(t)</math> is close to <math>\pi</math>,</li> <li>– For <math>l_1 = l_2</math> long period synchronization during: <math>\varphi_1 - \varphi_2</math> is a periodic function of <math>t</math>.</li> </ul>

### 4.3. Discussion

In the considered systems of two clocks suspended on the horizontally movable beam (Eqs. (27), (28), (68) and (69)) one can observe the following types of synchronizations: (i) the complete synchronization during which the pendula's displacements fulfill the relation  $\varphi_1(t) = \varphi_2(t)$  and the phase shift between pendula's displacements  $\varphi_1(t)$  and  $4\varphi_2(t)$  is equal to zero, (ii) the almost complete synchronization during the phase shift between pendula' displacements  $\varphi_1(t)$  and  $\varphi_2(t)$  is close to zero, (iii) antiphase synchronization during which the pendula' displacements fulfill the relation  $\varphi_1(t) = -\varphi_2(t)$  and the phase shift between the pendulum displacements is equal to  $\pi$  ( $180^\circ$ ), (iv) almost antiphase synchronization during which the phase shift between the pendulum displacements is close to  $\pi$  ( $180^\circ$ ). For the pendula with the same lengths in case (ii) pendula's displacements fulfill the relation  $\varphi_1(t) \approx \varphi_2(t)$ . Note that types (i) and (iii) are possible only for nonrobust case of identical pendulum masses ( $m_1 = m_2$ ). For cases (ii) and (iv) pendula's energy balance looks differently as can be seen in Fig. 41(a)–(c) (discontinuous model) and Fig. 42(a, b) (continuous model). Additionally, for the pendula with the same lengths there exists the possibility of long period synchronization during which the difference of the pendula's displacements  $\varphi_1 - \varphi_2$  is a periodic function of time and chaotic behavior of the clocks' pendula [45]. The pendula with different lengths can oscillate with different periods and one can observe 1:2, 1:3, 2:3, etc. synchronizations. The synchronous states of two coupled clocks are summarized in Table 2.

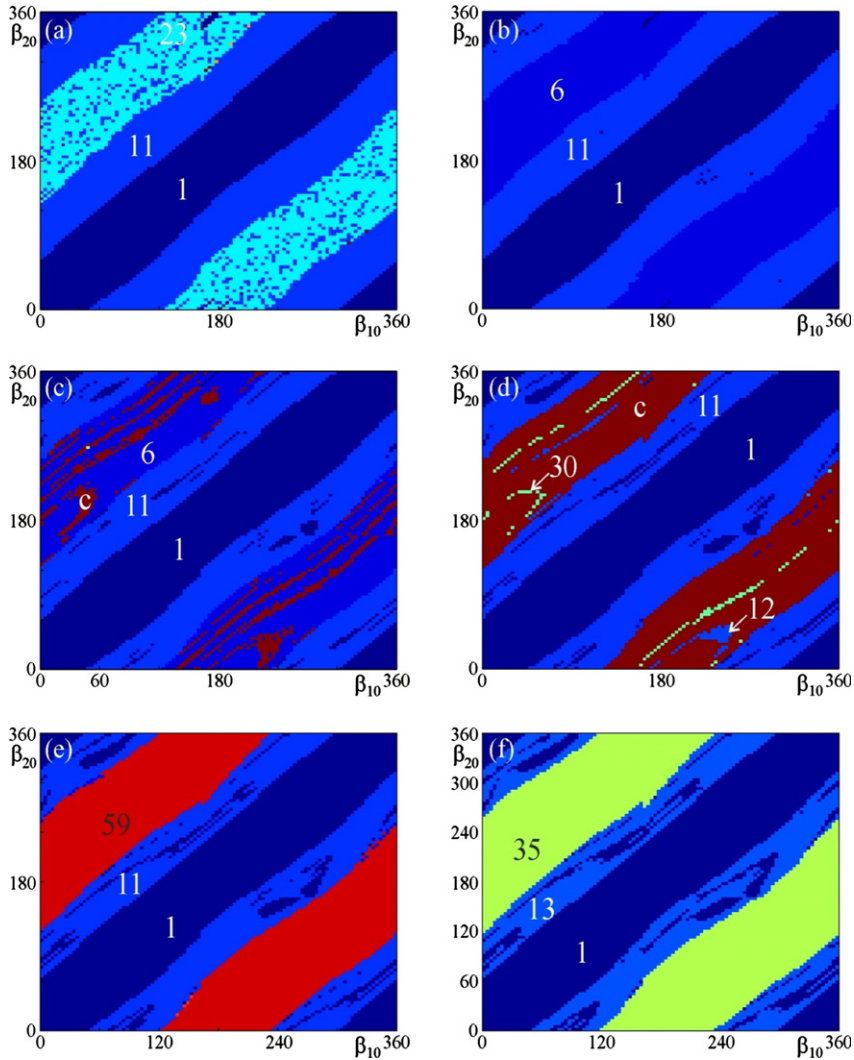


**Fig. 40.** Basins of attraction of different types of synchronous states for  $m_2 = 3.105$ ; the numbers indicate the period of the (LPS), (C) shows chaotic behavior. Parameters:  $\gamma_N = 4.5^\circ$  (a);  $\gamma_N = 4.8^\circ$  (b);  $\gamma_N = 5.0^\circ$  (c);  $\gamma_N = 5.05^\circ$  (d);  $\gamma_N = 5.1^\circ$  (e);  $\gamma_N = 5.2^\circ$  (f). Other parameters are the same as in Fig. 39, initial values:  $x(0) = 0.0$ ,  $\dot{x}(0) = 0.0$ ,  $\varphi_{10} = \Phi \sin \beta_{10}$ ,  $\dot{\varphi}_{10} = \alpha \Phi \cos \beta_{10}$ .

(i) *Energy balance in the state of almost complete synchronization*

In the state of complete synchronization the pendula's displacements fulfill the relation  $\varphi_1(t) = \varphi_2(t)$ , both dampers dissipate the same amount of energy:

$$\begin{aligned}
 W_1^{DAMP} &= \int_0^T c_\varphi \dot{\varphi}_1^2 dt = \int_0^T c_\varphi \dot{\varphi}_2^2 dt = W_2^{DAMP}, \\
 m_2 W_1^{SYN} &= m_2 \int_0^T m_1 \ddot{x} l \cos \varphi_1 \dot{\varphi}_1 dt = m_1 \int_0^T m_2 \ddot{x} l \cos \varphi_2 \dot{\varphi}_2 dt = m_1 W_2^{SYN}, \\
 W_1^{DRIVE} &= W_2^{DRIVE}.
 \end{aligned} \tag{92}$$

After substituting the energy values satisfying Eq. (92) into Eqs. (44), Eqs. (44) are not contradictory equations only in two cases: (i) masses of both pendula are equal ( $m_1 = m_2$ ) and both pendula transmit the same amount of energy to the beam (see Fig. 41(a)), (ii) synchronization energies  $W_{1,2}^{SYN}$  are equal to zero, i.e., both pendula dissipate the whole energy supplied by the escapement mechanism (see Fig. 41(b)).

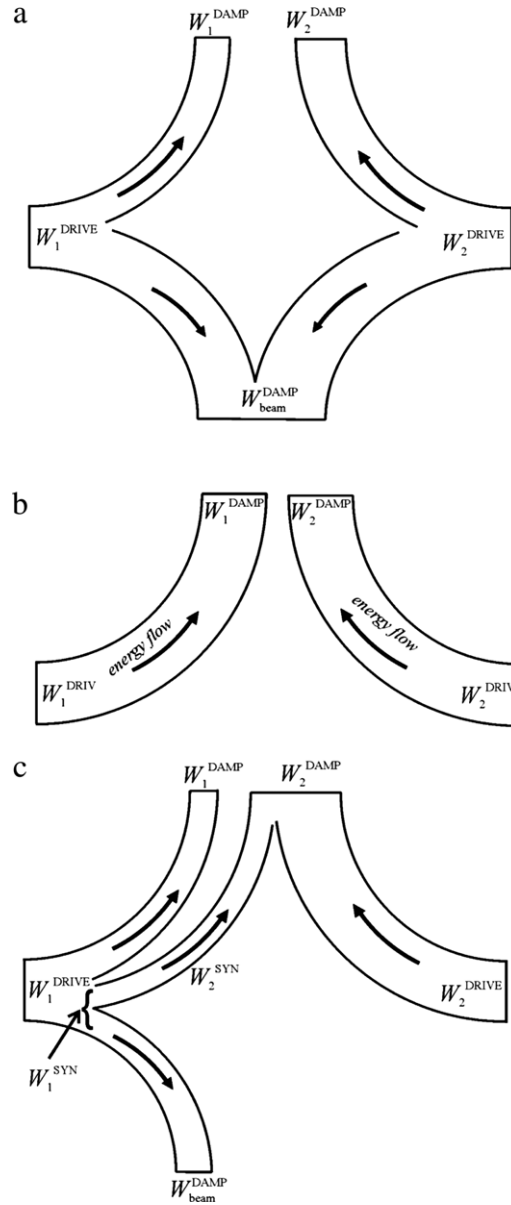


**Fig. 41.** Energy balance schemes: (a) almost complete synchronization – both pendula drive the beam, (b) antiphase synchronization – beam at rest, (c) almost antiphase synchronization – pendulum 1 drives the beam and supplies energy to pendulum 2.

In general case when  $m_1 \neq m_2$  and  $c_x \neq 0.0$ , instead of complete synchronization we observe almost complete synchronizations during which the pendula's displacements are not identical (but close to each other) and one gets the following expressions for the considered energies

$$\begin{aligned}
 W_1^{DAMP} &= \int_0^T c_\varphi \dot{\varphi}_1^2 dt \approx \int_0^T c_\varphi \dot{\varphi}_2^2 dt = W_2^{DAMP}, \\
 W_1^{SYN} &= \int_0^T m_1 \ddot{x} l \cos \varphi_1 \dot{\varphi}_1 dt \approx \int_0^T m_2 \ddot{x} l \cos \varphi_2 \dot{\varphi}_2 dt = W_2^{SYN}
 \end{aligned} \tag{93}$$

which fulfills Eqs. (44). The scheme of the energy balance is similar to the one in Fig. 41(a).

(ii) *Energy balance in the state of almost antiphase synchronization*

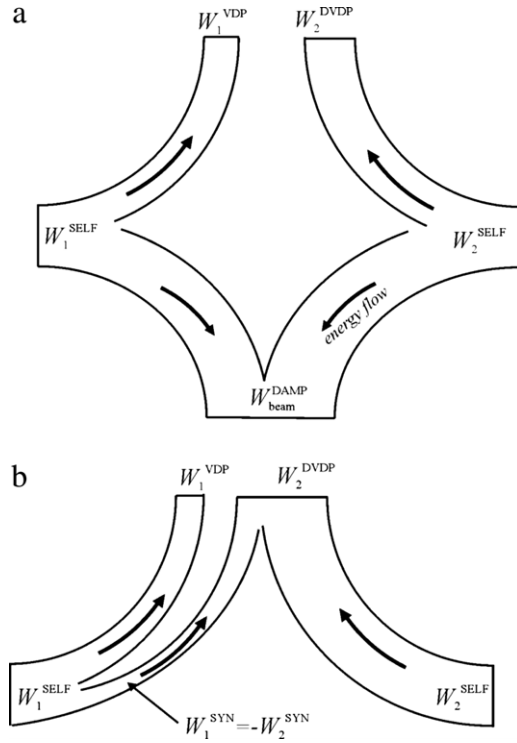


**Fig. 42.** Energy balances of the system (1, 2); (a) almost complete synchronization – both pendula drive the beam, (b) almost antiphase synchronization – pendulum 1 drives pendulum 2 via the beam.

In the state of antiphase synchronization the pendula' displacements fulfill the relation  $\varphi_1(t) = -\varphi_2(t)$  and both dampers dissipate the same amount of energy. The energies transmitted to the beam have opposite signs, i.e.,

$$\begin{aligned}
 W_1^{DAMP} &= \int_0^T c_\varphi \dot{\varphi}_1^2 dt = \int_0^T c_\varphi \dot{\varphi}_2^2 dt = W_2^{DAMP}, \\
 m_2 W_1^{SYN} &= m_2 \int_0^T m_1 \ddot{x} l \cos \varphi_1 \dot{\varphi}_1 dt = -m_1 \int_0^T m_2 \ddot{x} l \cos \varphi_2 \dot{\varphi}_2 dt = -m_1 W_2^{SYN}, \\
 W_1^{DRIVE} &= W_2^{DRIVE}.
 \end{aligned} \tag{94}$$

After substituting the energy values satisfying Eq. (94) into Eqs. (44), Eqs. (44) are not contradictory equations only when the beam acceleration is zero, which implies the zero value of its velocity and acceleration (in the synchronization state of the behavior of the system is periodic). This condition requires a balancing of the forces which act on the pendulum beam, and this in turn requires that the pendula have the same mass. The scheme of the energy balance is similar to the one in Fig. 41(b).

If the pendula' masses are different, instead of antiphase synchronization we observe an almost-antiphase synchronization, during which the oscillations of the pendula have different amplitudes and phase shift between these oscillations is close, but not equal to  $\pi$  ( $180^\circ$ ). Hence

$$\begin{aligned}
 W_1^{DAMP} &\neq W_2^{DAMP}, \\
 W_1^{SYN} &\neq W_2^{SYN}.
 \end{aligned} \tag{95}$$

The energy balance for the case of almost antiphase synchronization is shown in Fig. 41(c). Part of the energy supplied by the escapement mechanism of pendulum 1 (let us assume that it has smaller mass)  $W_1^{DRIVE}$  is dissipated by the damper of this pendulum ( $W_1^{DAMP}$ ) and the rest ( $W_1^{SYN}$ ) is transmitted to the beam. The damper of pendulum 2 dissipates the energy  $W_2^{DRIVE}$  supplied by the escapement mechanism and energy ( $W_2^{SYN}$ ) transmitted from the beam (mathematically this energy is negative). The damper of the beam dissipates the rest of the energy  $W_1^{SYN}$ :  $W_{beam}^{SYN} = W_1^{SYN} - (-W_2^{SYN})$ .

The system consisting of the beam and two self-excited pendula with van der Pol's type of damping can perform four types of synchronization: (i) complete synchronization (possible only for nonrobust case of identical masses of both pendula), i.e., the periodic motion of the system during which the displacements of both pendula are identical ( $\varphi_1(t) = \varphi_2(t)$ ), (ii) almost complete synchronization of the pendula with different masses, in which phase difference between the displacements  $\varphi_1(t)$  and  $\varphi_2(t)$  is small (not larger than a few degrees), (iii) antiphase synchronization (possible only

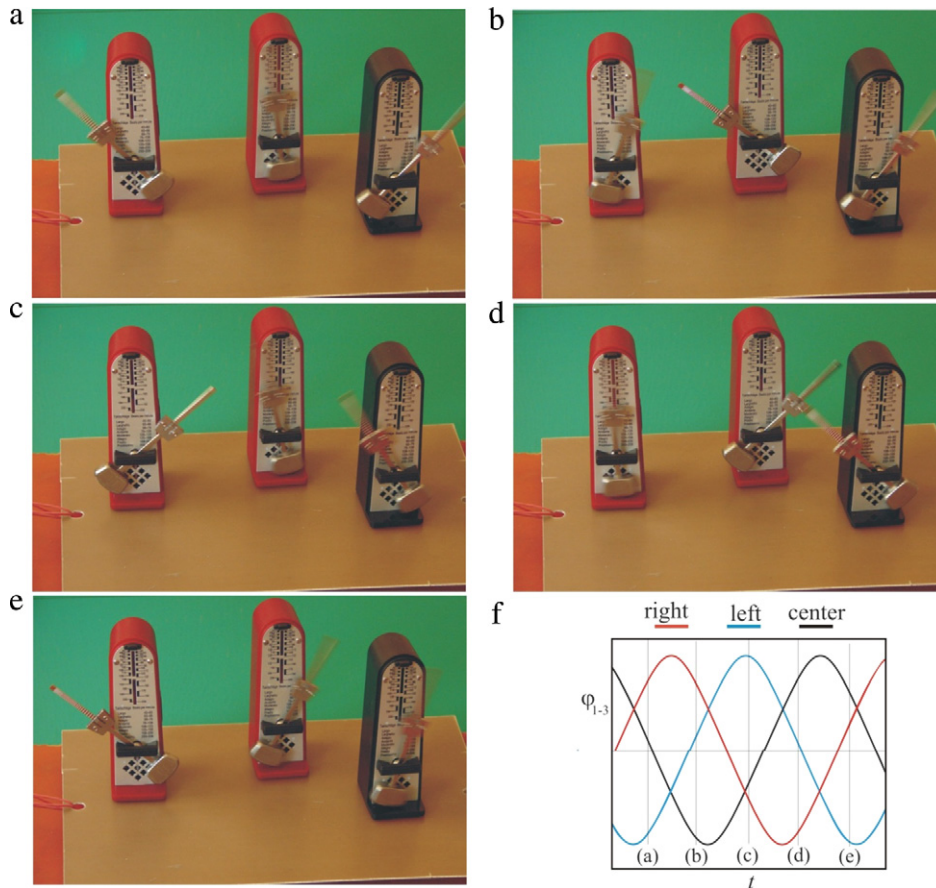


**Fig. 43.** Three metronomes located on the plate which can roll on the base obtain a synchronous state with a phase difference  $\Delta\beta = |\beta_2 - \beta_1| = |\beta_3 - \beta_2| = |\beta_1 - \beta_3| = 2\pi/3$ .

for nonrobust case of identical masses of both pendula), i.e., the periodic motion of the system, during which the phase difference between the displacements  $\varphi_1(t)$  and  $\varphi_2(t)$  is equal to  $\pi$  ( $180^\circ$ ), (iv) almost-antiphase synchronization, during which the phase difference between the displacements  $\varphi_1(t)$  and  $\varphi_2(t)$  is close to  $\pi$  ( $180^\circ$ ) and the amplitude of oscillations of both pendula are different.

The observed behavior of the system (68), (69) can be explained by the energy expressions derived in Section 3.5 and taking into consideration Eq. (90), (91). The examples of the energy flow diagrams are shown in Fig. 42(a, b). In the state (ii) both pendula drive the beam (transferring to it the part of the energy obtained from van der Pol's dampers) as seen in Fig. 40(a). In the case (iv) the pendulum with larger mass and smaller amplitude of oscillations transmits part of its energy to the pendulum lower mass. The beam motion is negligibly small and the pendulum with lower mass reduces the amplitude of vibration of the pendulum with larger mass, acting on the classical model of the dynamic damper.

We identified two reasons for the sudden change of the attractor in system (68), (69); (i) loss of stability of one type of synchronization after which the system trajectory jumps to the coexisting synchronization state, (ii) inability of van der Pol's damper of one of the pendula energy necessary to drive the second pendulum.

We give evidence that two coupled clocks can show chaotic behavior, i.e., uncorrelated motion of the pendula. We show that in the wide range of the system parameters the system exhibits multistability. The basins of attraction of the coexisting various (LPS) and chaotic attractors are small so practically any perturbation or fluctuation of the system parameters can result in the jumps of the system between different attractors. The described phenomena seem to be robust as they exist in the wide range of the system parameters.

## 5. Synchronization of $n$ clocks

### 5.1. Experimental synchronization of metronomes

In our experiments we observed the oscillations of  $n$  metronomes (mass of each one 0.119 (kg)) located on a plate. The plate rests on light polished rolls which can roll on the parallel smooth base and is connected by the spring to the vertical

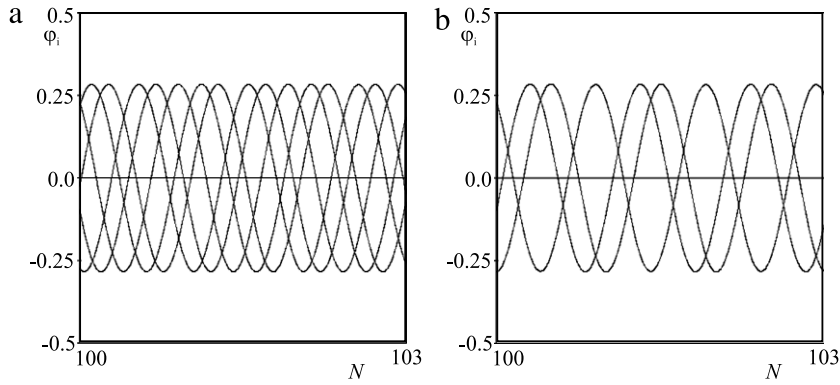


**Fig. 44.** Time series of 11 metronomes located on the plate which can roll on the base;  $N$  indicates a number of periods of oscillations ( $t = 2N\pi/\alpha$ ): (a) five clusters configuration,  $\beta_{II} = 0.475\pi$ ,  $\beta_{III} = 0.791\pi$ , (b) three clusters configuration,  $\beta_{II} = 0.53\pi$ .

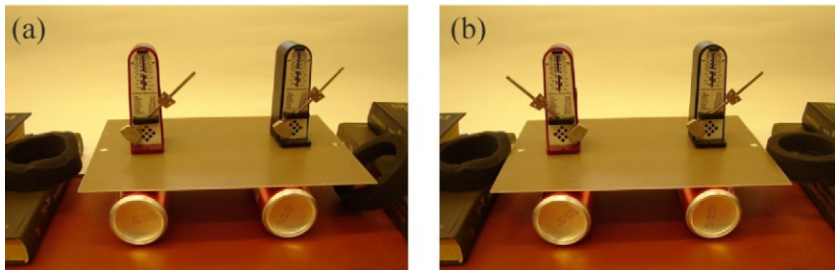


**Fig. 45.** Two metronomes located on the plate which can roll on the base: (a) complete synchronization, (b) antiphase synchronization. Arrows indicate additional masses added to differentiate the total masses of the metronomes' pendula.

base. Metronomes are Wittner's Taktell-Piccolino (Series 890). The frequency of the metronome is adjusted by changing the position of a mass on the metronome's pendulum bob. The metronomes' standard settings range from 40 ticks per minute (largo) to 208 ticks per minute (prestissimo). For the performed measurements the highest standard frequency settings have been used. They corresponds to 104 oscillations per minute as the metronomes tick twice per cycle.

Pendulum metronomes act in the same way as pendulum clocks. The energy is supplied to each metronome by a hand wound spring and their oscillations are controlled by the escapement mechanism described in Section 2.2. The speed camera (Photron APX RS with the film speed at 1500 frames per second) has been used to observe the motion of the metronomes.

In the first case three metronomes have been located on the plate. Fig. 43 shows that the metronomes perform steady state periodic oscillations with a constant phase difference  $\Delta\beta = |\beta_2 - \beta_1| = |\beta_3 - \beta_2| = |\beta_1 - \beta_3| = 2\pi/3$ .

In Fig. 44(a, b) time series of 11 metronomes located on the elastic plate which can roll on the base are shown.  $N$  indicates a number of periods of oscillations, i.e.,  $t = 2N\pi/\alpha$ . Fig. 44(a) presents five cluster symmetrical configuration ( $n_I = 1$ ,  $n_{II} = 4$ ,  $n_{III} = 1$ ,  $n_{IV} = 1$ , and  $n_V = 4$ ), and Fig. 44(b) three cluster symmetrical configuration with respectively  $n_I = 1$ ,  $n_{II} = 5$ , and  $n_{III} = 5$  pendula.

In Fig. 45(a, b) we show the simple experimental confirmation of the stability of both synchronization configurations. Two metronomes located on the elastic plate which can roll on the base obtain complete synchronization (Fig. 45(a)) and antiphase synchronization (Fig. 45(b)). The masses of metronomes' pendula are slightly different as the small masses (indicated by arrows) have been added to one of them. Notice that in the case of antiphase synchronization the plate is not at rest (as in the case of identical pendula), but oscillates with a small amplitude. There is also a small difference in pendula amplitudes.

Typical configurations for the system of three clocks have been also observed in the experiments with metronomes described in Fig. 46(a, b). Three metronomes (with different masses of pendula) located on the plate which can roll on the base can show the symmetrical synchronization with phase shift  $\beta_{II} = \beta_{III} = 120^\circ$  (Fig. 46(a)) and antiphase synchronization of the left metronome with the cluster consisting of the center and right metronomes (Fig. 46(b)). In the second case the mass of the left pendulum is equal to the sum of the masses of the central and right pendula.

Generally, in the case of light base (mass 0.058 (kg)) with smooth surface we observe complete synchronization of all metronomes. In this case the damping in the system is very low and the metronomes ticks destabilize antiphase synchronizations (Pantaleone, 2002). For more damped system (rough surface of heavier base of the mass 2 (kg)) we observe the occurrence of three or five clusters of synchronized metronomes.

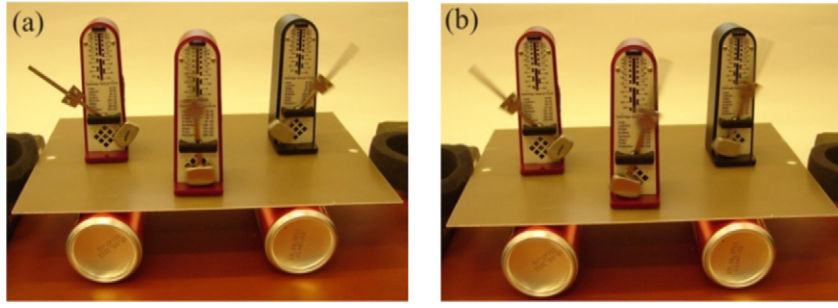


**Fig. 46.** Three metronomes located on the plate which can roll on the base: (a) symmetrical synchronization with phase shift  $\beta_{II} = \beta_{III} = 120^\circ$ , (b) antiphase synchronization of the left metronome with the cluster of the center and right metronomes (the mass of the left pendulum is equal to the sum of the masses of the center and right pendula).

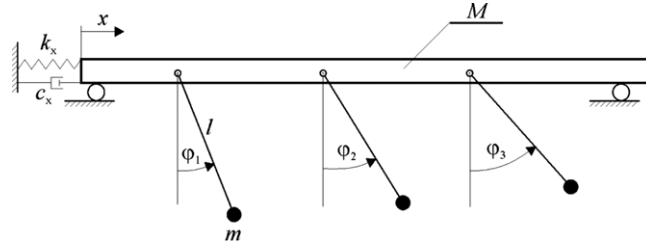


**Fig. 47.** The model of  $n$  pendulum clocks hanging from an elastic horizontal beam.

## 5.2. The model

In the modeling of the dynamics of  $n$  coupled clocks we consider the generalization of the model described in Section 3.4 shown in Fig. 47. The beam of mass  $M$  can move in the horizontal direction  $x$  with the viscous friction given by damping coefficient  $c_x$ . One side of the beam is attached to the base through the spring with stiffness coefficient  $k_x$ . The beam supports  $n$  identical pendulum clocks with pendula of the same length  $l$  and different masses  $m_i (i = 1, 2, \dots, n)$ . The position of the  $i$ -th pendula is given by a variable  $\varphi_i$  and its oscillations are damped by viscous friction described by damping coefficient  $c_{\varphi_i}$  (these dampers are not shown in Fig. 47). The beam is considered as a rigid body so the elastic waves along it are not considered. We describe the phenomena which take place far below the resonances for both longitudinal and transverse oscillations of the beam.

The system equations can be written in the form of Euler–Lagrange equations:

$$m_i l^2 \ddot{\varphi}_i + m_i \dot{x} l \cos \varphi_i + c_{\varphi_i} \dot{\varphi}_i + m_i g l \sin \varphi_i = M_{D_i}, \quad (96)$$

$$\left( M + \sum_{i=1}^n m_i \right) \ddot{x} + \sum_{i=1}^n (m_i l \ddot{\varphi}_i \cos \varphi_i - m_i l \dot{\varphi}_i^2 \sin \varphi_i) + c_x \dot{x} + k_x x = 0. \quad (97)$$

The clock escapement mechanism represented by momentum  $M_{D_i}$  provides the energy needed to compensate the energy dissipation due to the viscous friction  $c_{\varphi_i}$  and to keep the clocks running. This mechanism acts in the way described in Section 2.2, i.e., if  $\varphi_i < \gamma_N$  then  $M_{D_i} = M_{N_i}$  and when  $\varphi_i < 0$  then  $M_{D_i} = 0$ , where  $\gamma_N$  and  $M_{N_i}$  are constant values which characterize the mechanism. For the second stage one has for  $-\gamma_N < \varphi_i < 0$   $M_{D_i} = -M_{N_i}$  and for  $\varphi_i > 0$   $M_{D_i} = 0$ . In the undamped ( $c_{\varphi_i} = 0$ ) and unforced ( $M_{D_i} = 0$ ) case when the beam  $M$  is at rest ( $x = 0$ ) each pendulum oscillates with period  $T$  equal to 1.0 (s) and frequency  $\alpha = 2\pi$  ( $s^{-1}$ ).

After the initial transient the pendula perform the periodic oscillations so the solution of Eq. (96) can be approximately described as:

$$\varphi_i = \Phi_i \sin(\alpha t + \beta_i), \quad (98)$$

where  $\Phi_i$  are constant. Assuming that the pendulum amplitude  $\Phi_i$  are small one can linearize Eq. (97) as follows:

$$\left( M + \sum_{i=1}^n m_i \right) \ddot{x} + c_x \dot{x} + k_x x + \sum_{i=1}^n (m_i l \ddot{\varphi}_i - m_i l \dot{\varphi}_i^2 \varphi_i) = 0, \quad (99)$$

or substituting Eq. (98) into Eq. (99)

$$\left( M + \sum_{i=1}^n m_i \right) \ddot{x} + c_x \dot{x} + k_x x = \sum_{i=1}^n (m_i l \alpha^2 \Phi_i \sin(\alpha t + \beta_i) + m_i l \alpha^2 \Phi_i^3 \cos^2(\alpha t + \beta_i) \sin(\alpha t + \beta_i)). \quad (100)$$

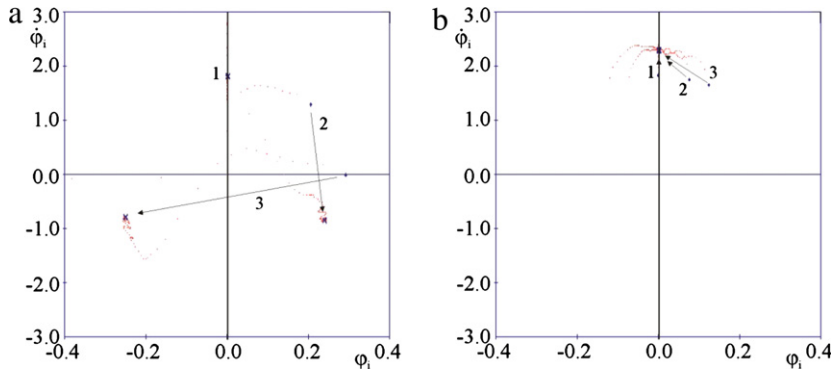


**Fig. 48.** The synchronization configurations for three pendula;  $m = 1$  (kg),  $l = g/4\pi^2$  (m),  $c_\phi = 0.01$  (N s m),  $M = 1$  (kg),  $c_x = 0.1M$  (N s/m),  $k_x = M$  (N/m),  $M_N = 0.075$  (N m),  $\gamma_N = \pi/36$ : (a) (SS) with phase difference  $\Delta\beta = 2\pi/3$ ;  $\beta_{10} = 0$ ,  $\beta_{20} = 2\pi/8$ ,  $\beta_{30} = 2\pi/4$  (b) (CS):  $\beta_{10} = 0$ ,  $\beta_{20} = 2\pi/24$ ,  $\beta_{30} = 2\pi/18$ .

Taking into consideration the relation  $\cos^2 \alpha \sin \alpha = 0.25(\sin \alpha + 3 \sin 3\alpha)$ , and denoting

$$U = M + \sum_{i=1}^n m_i, \quad F_{1i} = m_i \alpha^2 (\Phi_i + 0.25 \Phi_i^3), \quad F_{3i} = 0.75 m_i \alpha^2 \Phi_i^3, \quad (101)$$

we have

$$U \ddot{x} + c_x \dot{x} + k_x x = \sum_{i=1}^n (F_{1i} \sin(\alpha t + \beta_i) + F_{3i} \sin(3\alpha t + 3\beta_i)). \quad (102)$$

Assuming the small value of damping coefficient  $c_x$  Eq. (102) can be rewritten in the following form

$$x = \sum_{i=1}^n (X_{1i} \sin(\alpha t + \beta_i) + X_{3i} \sin(3\alpha t + 3\beta_i)), \quad (103)$$

where  $X_{1i}$ ,  $X_{3i}$  and  $\beta_i$  are constant. Right hand side of Eq. (103) represents the force with which  $n$  pendula act on the beam  $M$ . Eq. (103) allows the determination of the beam acceleration  $\ddot{x}$  and (after integration) of its velocity  $\dot{x}$  and displacement  $x$ . Notice that this force consists only of the first and the third harmonics. Later this property will be essential in the explanation why in the system (96), (97) one observes only configurations consisting of three and five clusters of synchronized pendula.

It should be mentioned here that our theoretical results are based on the approximation of the pendula motion given by Eq. (98). In numerical simulations of Eq. (96), (97) we got:  $\varphi_i = 0.144 \sin(\alpha t + \beta_i) + 0.0033 \sin 3(\alpha t + \beta_i) + 6.75 * 10^{-4} \sin 5(\alpha t + \beta_i) + 3.2 * 10^{-4} \sin 7(\alpha t + \beta_i) + \dots$  which clearly shows that higher harmonics are small and have small (negligible) influence on the system (96), (97) motion.

### 5.3. Numerical simulations

#### 5.3.1. Identical clocks

In our numerical simulations we consider  $m = 1$  (kg),  $l = g/4\pi^2$  (m), and  $c_{\phi_i} = c_\phi = 0.01$  (N s m) so the frequency of pendula's oscillations  $\alpha$  is equal to  $2\pi$ . The stiffness  $k_x$  and damping  $c_x$  coefficients are assumed to be proportional to the beam mass  $M$ . The clock mechanism parameters are assumed to be  $M_N = 0.075$  (N m) and  $\gamma_N = \pi/36$ . We assume that the initial conditions for the pendula are given by the initial value of  $\beta_{i0}$ , i.e.,  $\varphi_{i0} = \Phi \sin \beta_i$  and  $\dot{\varphi}_{i0} = \alpha \Phi \cos \beta_{i0}$ . For the given parameters of the pendula and the clock mechanism  $\Phi = 0.3$ .

##### (a) Three clocks ( $n = 3$ )

In Fig. 48 we plot the position of each pendulum given by Eqs. (96), (97) in the phase space  $\varphi_i, \dot{\varphi}_i$  at the time when the first pendulum is moving through the equilibrium position  $\varphi_1 = 0$  with the positive velocity  $\dot{\varphi}_1 > 0$ . The points indicate the transients leading from the given initial conditions to the final configuration indicated in bold. After the initial transients the pendula perform periodic oscillations (which are visible in Fig. 48 by a single point for each pendulum) with the same amplitude (as the distance of each point to the origin (0, 0) is equal). The oscillations of the pendula differ only by the phase differences  $\beta_i$ .

Fig. 48(a, b) shows two possible configurations for the system (96), (97) with three pendula. In the first configuration (shown in Fig. 48(a)) there is a constant phase difference  $\Delta\beta = |\beta_2 - \beta_1| = |\beta_3 - \beta_2| = |\beta_1 - \beta_3| = 2\pi/3$  between the pendula. We call this configuration symmetrical synchronization (SS). In Fig. 48(b) one observes complete synchronization (CS). Besides these configurations we observed also the desynchronous behavior (DSB) of all pendula. In DSB regime the phase difference between pendula is not constant and is changing chaotically. All the observed steady states are stable as

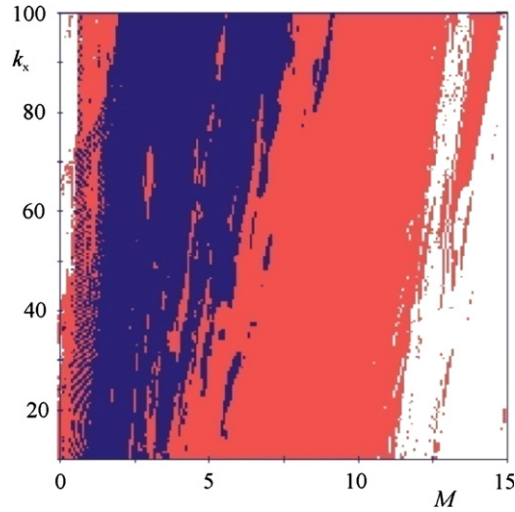


**Fig. 49.** The steady states of Eqs. (96), (97) for different values of parameters  $M$  and  $k_x$ ;  $m = 1$  (kg),  $l = g/4\pi^2$  (m),  $c_\varphi = 0.01$  (N s m),  $c_x = 0.1M$  (N s/m),  $M_N = 0.075$  (N m),  $\gamma_N = \pi/36$ ,  $\beta_{10} = 0$ ,  $\beta_{20} = \pi/8$ ,  $\beta_{30} = \pi/9$ ,  $x_0 = \dot{x}_0 = 0$ . (SS), (CS) and (DSB) are indicated respectively in navy blue, white and red colors. (For interpretation of the references to colour in this figure legend, the reader is referred to the web version of this article.)

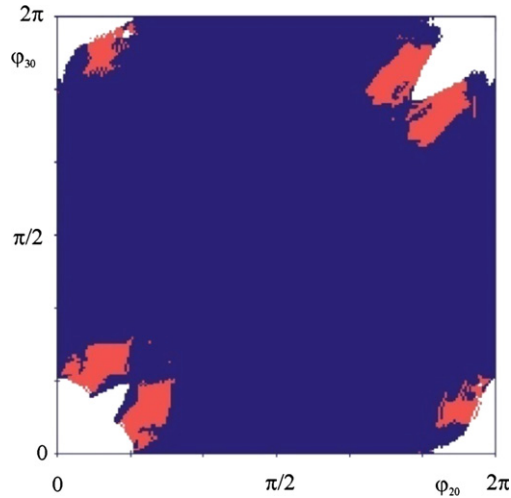


**Fig. 50.** The basins of attraction of the possible steady states of Eqs. (96), (97) in the  $\beta_{20} - \beta_{30}$  plane;  $m = 1$  (kg),  $l = g/4\pi^2$  (m),  $c_\varphi = 0.01$  (N s m),  $M = 1$  (kg),  $c_x = 0.1M$  (N s/m),  $k_x = M$  (N/m),  $M_N = 0.075$  (N m),  $\gamma_N = \pi/36$ ,  $\beta_{10} = 0$ ,  $x_0 = \dot{x}_0 = 0$ . The basins of (SS), (CS) and (DSB) are indicated respectively in navy blue, white and red colors. (For interpretation of the references to colour in this figure legend, the reader is referred to the web version of this article.)

the solution of the variational equation (87) decays. They can be observed in a wide range of the control parameters  $M$  and  $k_x$  as shown in Fig. 49, where (SS), (CS) and (DSB) are indicated respectively in black, white and gray colors. In the calculation shown in Fig. 49 we assumed the following initial conditions  $\beta_{10} = 0$ ,  $\beta_{20} = \pi/8$ ,  $\beta_{30} = \pi/9$ ,  $x_0 = 0$ .

In Fig. 50 we present the basins of attraction of the possible steady states of the system (96), (97) in  $\beta_{20} - \beta_{30}$  plane, where  $\beta_{20}$  and  $\beta_{30}$  represent the initial positions of the second and third pendula. Other initial conditions have been assumed to be equal to zero, i.e.,  $\beta_1 = 0$ ,  $x_0 = \dot{x}_0 = 0$ . The basins of (SS), (CS) and (DSB) are indicated respectively in black, white and gray colors.

(b)  $n$  clocks ( $n > 3$ )

In what follows, we show the examples of typical configurations in the system of more than 3 pendula. Fig. 51(a)–(c) shows three possible configurations for the system (96), (97) with six pendula. The points indicate the transients leading from the given initial conditions to the final configuration indicated in bold. In the first configuration (shown in Fig. 51(a)) there are three clusters (pendula 1,2,3,4 and 5,6) of two synchronized pendula. The phase difference between the pendula in different clusters is equal to  $\Delta\beta = 2\pi/3$ . Three pairs of pendula synchronized in antiphase (the phase difference between pendula in each pair is equal to  $\Delta\beta = \pi$ ) are shown in Fig. 51(b). Pendula 1, 2 and 3 are respectively in antiphase with

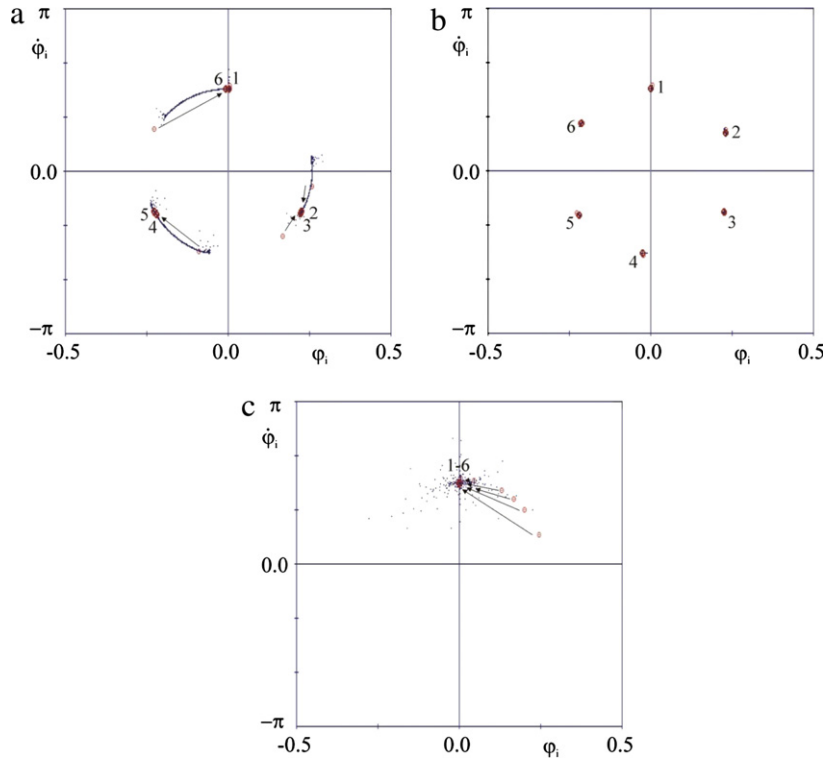


**Fig. 51.** Synchronization configurations for six pendulums;  $m = 1.0$  (kg),  $l = 0.2489$  (m),  $c_\varphi = 0.01$  (N s/m),  $M_N = 0.075$  (N m),  $\gamma_N = \pi/36$ ; (a) symmetrical synchronization of three clusters of two pendula, phase difference between clusters  $M = 14$  (kg),  $c_x = 2.34$  (N s/m),  $k_x = 5.53$  (N/m),  $\Delta\beta = 2\pi/3$ ;  $\beta_{10} = 0.017$ ,  $\beta_{20} = 1.74$ ,  $\beta_{30} = 2.44$ ,  $\beta_{40} = 3.49$ ,  $\beta_{50} = 4.19$ ,  $\beta_{60} = 5.24$ ; (b) three pairs of pendula synchronized in antiphase;  $M = 140$  (kg),  $c_x = 20.0$  (N s/m),  $k_x = 55.3$  (N/m),  $\beta_{10} = 0.017$ ,  $\beta_{20} = 1.06$ ,  $\beta_{30} = 2.09$ ,  $\beta_{40} = 3.23$ ,  $\beta_{50} = 4.19$ ,  $\beta_{60} = 5.305$ ; (c) complete synchronization of six pendula;  $M = 14$  (kg),  $c_x = 2.34$  (N s/m),  $k_x = 5.53$  (N/m),  $\beta_{10} = 0.017$ ,  $\beta_{20} = 0.17$ ,  $\beta_{30} = 0.52$ ,  $\beta_{40} = 0.70$ ,  $\beta_{50} = 0.87$ ,  $\beta_{60} = 1.22$ ;  $x_0 = \dot{x}_0 = 0$ .

pendula 4, 5 and 6. The phase difference between pendula in different pairs depends on the initial conditions. In Fig. 51(c) one observes complete synchronization (CS). For even  $n$  we have not observed (DSB) of all pendula.

In Fig. 52(a)–(d) we plot the position of each of  $n = 11$  pendula in the phase space  $\varphi_i, \dot{\varphi}_i$  at the time when the first pendulum is moving through the equilibrium position  $\varphi_1 = 0$  with the positive velocity  $\alpha\dot{\varphi}_1 > 0$ . Fig. 52(a) shows the configuration of three clusters with respectively  $n_I = 2$ ,  $n_{II} = 4$ , and  $n_{III} = 5$  pendula. The pendula in each cluster are synchronized. Fig. 52(b) shows the configuration with five clusters of respectively  $n_I = 1$ ,  $n_{II} = 3$ ,  $n_{III} = 2$ ,  $n_{IV} = 1$ , and  $n_V = 4$  pendula. In Fig. 52(c) the special case of the symmetrical three clusters configuration with respectively  $n_I = 1$ ,  $n_{II} = 5$ , and  $n_{III} = 5$  pendula is shown. Fig. 52(d) presents the symmetrical configuration of five clusters ( $n_I = 1$ ,  $n_{II} = 4$ ,  $n_{III} = 1$ ,  $n_{IV} = 1$ , and  $n_V = 4$ ).

For all considered odd  $n$  besides the above configurations we have observed; (i) a complete synchronization, (ii) desynchronous behavior of all pendula. For even  $n$  additionally; (iii) the anti-phase synchronization in pairs have been observed. In the considered range of  $n$  we have not observed other stable cluster configuration.

#### (c) Influence of the beam motion on the pendula's oscillations

The synchronization between the pendula can be obtained as a result of the interplay between the period of oscillations of the pendula, the amplitude of the beam oscillations and the phase difference between the motions of the pendula and the beam. In the simplest example of one pendulum hanging from the beam, the beam motion which is in phase (out of phase) with the motion of the pendulum increases (decreases) the period of oscillations of the pendulum. In the case of  $n$  pendula hanging from the beam, the beam motion can temporarily increase or decrease their period of oscillations allowing synchronization. As in the case of two pendula (see Section 4) the energy is transmitted between pendula via the beam. One should notice here that the described mechanism explains why it is impossible to observe the existence of two groups of pendula with unequal number of members which synchronize in anti-phase, i.e., due to the unequal total mass of the pendula in each group the influence of the beam motion on each group cannot be the same.

To give an explanation why only three and five cluster configurations are observed we consider a horizontal displacement of the beam given by Eq. (103). Besides the local minimum for the  $n/2$  pairs of pendula synchronized in anti-phase (for even  $n$ ) the beam displacement  $x(t)$  given by Eq. (103) has local minima in two cases; (i) when the sum of the first harmonic components is equal to zero, (ii) when the sum of the first and the third harmonic components is equal to zero. One can show that the conditions (i) and (ii) guarantee the local minima of energy of the undamped and non-excited system. Neglecting

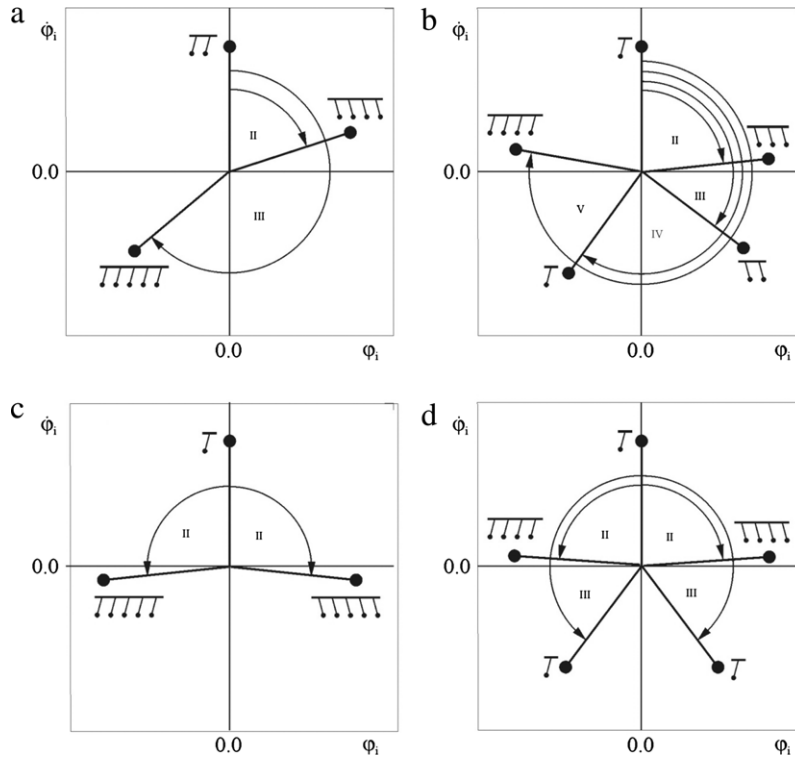


**Fig. 52.** Cluster configurations for  $n = 11$  pendula;  $m = 1$  (kg),  $l = g/4\pi^2$  (m),  $c_\varphi = 0.01$  (N s/m),  $M = 1$  (kg),  $c_x = 0.1$  (N s/m),  $k_x = 1$  (N/m),  $M_N = 0.075$  (N m),  $\gamma_N = \pi/36$ : (a) three cluster configuration;  $n_I = 2$ ,  $n_{II} = 4$ ,  $n_{III} = 5$ , (b) five cluster configuration;  $n_I = 1$ ,  $n_{II} = 3$ ,  $n_{III} = 2$ ,  $n_{IV} = 1$ ,  $n_V = 4$ , (c) symmetrical three cluster configuration;  $n_I = 1$ ,  $n_{II} = 5$ , and  $n_{III} = 5$ , (d) symmetrical five cluster configuration;  $n_I = 1$ ,  $n_{II} = 4$ ,  $n_{III} = 1$ ,  $n_{IV} = 1$ , and  $n_V = 4$ .

damping and excitation in Eqs. (96), (97), i.e., assuming that  $\int_0^T c_\varphi \dot{\varphi}_i^2 dt = \int_0^T M_{Di} \dot{\varphi}_i dt$  and  $c_x = 0$  one can express total energy of the system in the following way:

$$E = E_x + E_p = \frac{m}{2} \sum_{i=1}^n (\dot{x}^2 + l^2 \dot{\varphi}_i^2 + 2\dot{x}\varphi_i l \cos \varphi_i) + \frac{M\dot{x}^2}{2} + mgl \sum_{i=1}^n (1 - \cos \varphi_i) + \frac{kx^2}{2} \quad (104)$$

where  $E_p$  and  $E_x$  represent respectively the energy of  $n$  pendula and the energy of the motion in  $x$  direction. Under the assumption (98) the energy of  $n$  pendula  $E_p$  is the same for all pendula configurations. Eqs. (97) and (103) allows us to write the energy of the motion in the direction  $x$  as follows

$$\begin{aligned} E_x &= \frac{1}{2} (M + nm) \dot{x}^2(t) + \frac{1}{2} k_x x^2(t) \\ &= \frac{1}{2} (M + nm) \left( \alpha X_1 \sum_{i=1}^n \cos(\alpha t + \beta_i) + 3\alpha X_3 \sum_{i=1}^n \cos 3(\alpha t + \beta_i) \right)^2 \\ &\quad + \frac{1}{2} k_x \left( X_1 \sum_{i=1}^n \sin(\alpha t + \beta_i) + X_3 \sum_{i=1}^n \sin 3(\alpha t + \beta_i) \right)^2. \end{aligned} \quad (105)$$

Local minima of Eq. (105) for the cases (i) and (ii) are clearly visible. It is possible to show that the first case occurs for three cluster configuration and the second one for five cluster configuration. The lack of other harmonics components in Eqs. (103) and (105) shows why the configurations with a number of clusters different from 3 or 5 are not observed.

(i) *Three cluster configuration*

Consider three cluster configuration with respectively  $n_I$ ,  $n_{II}$  and  $n_{III}$  ( $n_I \leq n_{II} \leq n_{III}$ ) pendula in the successive cluster. The sum of the first harmonic components in Eq. (105) is equal to zero when the angles  $\beta_{II}$  and  $\beta_{III}$  fulfill the relation:

$$\begin{aligned} n_I + n_{II} \cos \beta_{II} + n_{III} \cos \beta_{III} &= 0, \\ n_{II} \sin \beta_{II} + n_{III} \sin \beta_{III} &= 0. \end{aligned} \quad (106)$$

The solution of Eq. (106) exists when  $n_I + n_{II} > n_{III}$ . In the symmetrical case  $n_{II} = n_{III}$  and  $\beta_{III} = 2\pi - \beta_{II}$  Eq. (106) reduces to

$$\cos \beta_{II} = \frac{-n_I}{2n_{II}} \quad (107)$$

for which the solution exists if  $n_I \leq 2n_{II}$ . Our numerical results show that in the case of three cluster configuration the clocks oscillate with the frequency larger than the frequency of the uncoupled clock. We observed  $\alpha \approx 2\pi + 0.034$ .

#### (ii) Five cluster configuration

Five cluster configuration with respectively  $n_I, n_{II}, n_{III}, n_{IV}$  and  $n_V$  pendula in the successive cluster exists when the sums of the first and the third harmonics components in Eq. (105) are equal to zero. In this case it is possible to show that the angles  $\beta_{II-V}$  fulfill the relation:

$$\begin{aligned} n_I + n_{II} \cos \beta_{II} + n_{III} \cos \beta_{III} + n_{IV} \cos \beta_{IV} + n_V \cos \beta_V &= 0 \\ n_{II} \sin \beta_{II} + n_{III} \sin \beta_{III} + n_{IV} \sin \beta_{IV} + n_V \sin \beta_V &= 0 \\ n_I + n_{II} \cos 3\beta_{II} + n_{III} \cos 3\beta_{III} + n_{IV} \cos 3\beta_{IV} + n_V \cos 3\beta_V &= 0 \\ n_{II} \sin 3\beta_{II} + n_{III} \sin 3\beta_{III} + n_{IV} \sin 3\beta_{IV} + n_V \sin 3\beta_V &= 0. \end{aligned} \quad (108)$$

In the symmetrical cluster configuration  $n_{II} = n_{IV}, n_{II} = n_V, \beta_{II} = 2\pi - \beta_V, \beta_{III} = 2\pi - \beta_V$  Eq. (108) reduce to

$$\begin{aligned} n_I + 2n_{II} \cos \beta_{II} + 2n_{III} \cos \beta_{III} &= 0 \\ n_I + 2n_{II} \cos 3\beta_{II} + 2n_{III} \cos 3\beta_{III} &= 0 \end{aligned} \quad (109)$$

In five cluster configuration the displacement of the beam  $x(t)$  (given by (103)) and energy  $E_x$  (given by Eq. (105)) are equal to zero, i.e., in the linear approximation of system (96), (97) beam is at rest. In the numerical studies of Eqs. (96), (97) we have observed very small oscillations of the beam which are due to the nonlinear terms (omitted in Eq. (103)) and the acting of the escapement mechanism. In the case of five cluster configuration all pendula oscillate with the frequency nearly equal to the frequency of the uncoupled clock. Our numerical results show that  $\alpha \approx 2\pi + 0.0001$ .

### 5.3.2. Nonidentical clocks

In this section we generalize the results of the previous section for the case of  $n$  non-identical pendulum clocks. It has been assumed that the clocks under consideration are accurate, i.e., show exactly the same time, but can differ by the design of the escapement mechanism and the pendulum. Particularly, we consider the pendula with the same period of oscillations and different masses. Our main results shows that the phase synchronization of non-identical clocks is possible only when three or five clusters are created. Contrary to the case of identical clocks this result holds for both even and odd number of clocks. We derive the equations which allow the estimation of the phase differences between the clusters. We argue why other cluster configurations are not possible.

In our numerical simulations Eqs. (96), (97) have been integrated by the Runge–Kutta method. For simplicity we have assumed  $c_x = k_x = 0$ . The initial conditions have been set as follows; (i) for the beam  $x(0) = \dot{x}(0) = 0$ , (ii) for the pendula the initial conditions  $\varphi_1(0), \dot{\varphi}_1(0)$  have been calculated from the assumed initial phase differences  $\beta_{II}$  and  $\beta_{III}$  (in all calculations  $\beta_I = 0$  has been taken) using Eq. (98), i.e.,  $\varphi_1(0) = 0, \dot{\varphi}_1(0) = \alpha\Phi, \varphi_2(0) = \Phi \sin \beta_{II}, \dot{\varphi}_2(0) = \alpha\Phi \cos \beta_{II}, \varphi_3(0) = \Phi \sin(-\beta_{III}), \dot{\varphi}_3(0) = \alpha\Phi \cos \beta_{III}$  (as it will be explained later the angles  $\beta_I = \beta_1 = 0, \beta_{II} = \beta_2, \beta_{III} = -\beta_3$  have been introduced for better description of the symmetrical configurations). To prove the stability of the obtained configurations we have used Eqs. (87).

#### (a) Three clocks ( $n = 3$ )

Generally, in the system with three pendulum clocks one can observe the following synchronization cases; (i) complete synchronization, (ii) phase synchronization with the constant phase shifts between the pendula, i.e.,  $\varphi_1 - \varphi_2 = \text{constant}, \varphi_2 - \varphi_3 = \text{constant}$ . Antiphase synchronization can be observed only as the special case of (ii) and occurs when the sum of the masses of two pendula (1 and 2) is equal to the mass of the third pendulum (3), say  $m_1 + m_2 = m_3$ . In this case the first and the second pendula create a cluster ( $\varphi_1 = \varphi_2$ ) which oscillates in antiphase to the pendulum 3, i.e.,  $\varphi_1 = \varphi_2 = -\varphi_3$ .

Stable configurations of the pendula can be visualized in the following maps. We plot the position of each pendulum given by Eqs. (96), (97) (after decay of the transients) in the phase space  $\varphi_i, \dot{\varphi}_i$  at the time when the first pendulum is moving through the equilibrium position  $\varphi_1 = 0$  with positive velocity  $\dot{\varphi}_1 > 0$ . After the initial transients the pendula perform periodic oscillations, which are visible in such maps by a single point for each pendulum (for better visibility indicated as a black dot). As the pendula oscillate with the same amplitude the distance of each point to the origin (0, 0) is equal. The lines between these points and the origin create the angles which are equal to the angles of the phase differences  $\beta_i$  between the oscillations of the pendula. White circles around the group of pendula indicate that the cluster of the synchronized pendula has been created.

The examples of the synchronized states of the system with three non-identical clocks are shown in Fig. 53(a)–(c). Fig. 53(a) presents the pendula's configuration obtained for beam mass  $M = 10.0$  (kg) and different pendula masses:  $m_1 = 1.0$  (kg),  $m_2 = m_3 = 2.0$  (kg). As  $m_2 = m_3$  and  $\beta_{II} = \beta_{III}$ , one can observe symmetrical phase synchronization. Phase differences  $\beta_{II} = \beta_{III} = 104.5^\circ$  are different from that obtained for the case of identical pendula masses  $m_1 = m_2 =$

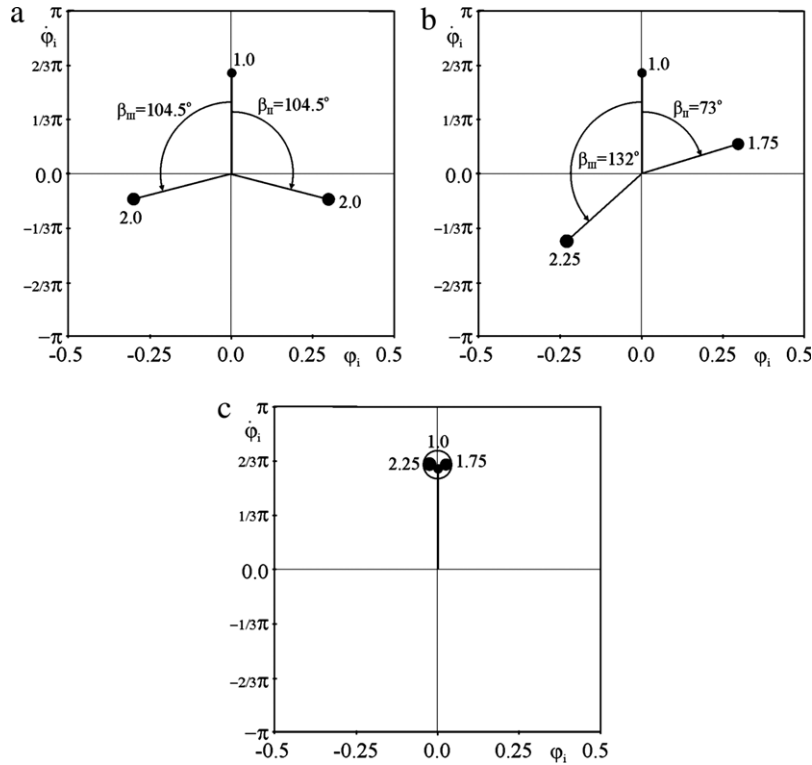


**Fig. 53.** Synchronization configurations for three pendula;  $M = 10.0$ ; (a) symmetrical synchronization of three pendula  $m_1 = 1.0$  (kg),  $m_2 = m_3 = 2.0$  (kg),  $\beta_{10} = 0^\circ$ ,  $\beta_{II0} = 60^\circ$ ,  $\beta_{III0} = 240^\circ$ , (b) unsymmetrical synchronization of three pendula  $m_1 = 1.0$  (kg),  $m_2 = 1.75$  (kg),  $m_3 = 2.25$  (kg),  $\beta_{10} = 0^\circ$ ,  $\beta_{II0} = 60^\circ$ ,  $\beta_{III0} = 240^\circ$ , (c) full synchronization of three pendula  $m_1 = 1.0$  (kg),  $m_2 = 1.75$  (kg),  $m_3 = 2.25$  (kg),  $\beta_{10} = 0^\circ$ ,  $\beta_{II0} = 25^\circ$ ,  $\beta_{III0} = 305^\circ$ .

$m_3 = 1.0$  (kg) (Section 5.3.1) where we observed  $\beta_{II} = \beta_{III} = 120^\circ$ . In Fig. 53(b) we show the results for:  $m_1 = 1.0$  (kg),  $m_2 = 1.75$  (kg),  $m_3 = 2.25$  (kg). Nonsymmetrical phase synchronization with phase differences:  $\beta_{II} = 73^\circ$ ,  $\beta_{III} = 132^\circ$  has been observed. Finally, Fig. 53(c) shows the example of the complete synchronization observed for:  $m_1 = 1.0$  (kg),  $m_2 = 1.75$  (kg),  $m_3 = 2.25$  (kg). Different configurations of the system (96), (97) have been obtained by setting various initial conditions.

Phase differences  $\beta_{II}$  and  $\beta_{III}$  can be approximately estimated on the base of the linear approximation derived in Section 5.2. In the case of three clocks the sum of the forces acting on the beam  $M$  (the right side of Eq. (102)) is equal to zero when:

$$F_{11} \sin \alpha t + F_{12} \sin \alpha t \cos \beta_{II} + F_{12} \cos \alpha t \sin \beta_{II} + F_{13} \sin \alpha t \cos \beta_{III} - F_{13} \cos \alpha t \sin \beta_{III} + F_{31} \sin 3\alpha t + F_{32} \sin 3\alpha t \cos 3\beta_{II} + F_{32} \cos 3\alpha t \sin 3\beta_{II} + F_{33} \sin 3\alpha t \cos 3\beta_{III} - F_{33} \cos 3\alpha t \sin 3\beta_{III} = 0. \quad (110)$$

In Eq. (110) the phase shift of pendulum 1 has been taken as zero (the reference point on the time axis  $t$ ). Additionally, due to the relation  $\beta_{II} = \beta_2$  and  $\beta_{III} = -\beta_3$ , symmetrical configuration of Fig. 53(a) is better visible as  $\beta_{II} = \beta_{III}$ . After some algebraic manipulations one gets:

$$\sin \alpha t (F_{11} + F_{12} \cos \beta_{II} + F_{13} \cos \beta_{III}) + \cos \alpha t (F_{12} \sin \beta_{II} - F_{13} \sin \beta_{III}) + \sin 3\alpha t (F_{31} + F_{32} \cos 3\beta_{II} + F_{33} \cos 3\beta_{III}) + \cos 3\alpha t (F_{32} \sin 3\beta_{II} - F_{33} \sin 3\beta_{III}) = 0. \quad (111)$$

Eq. (111) showing the force acting on the beam  $M$  can be expressed as the sum of the first and third harmonics. Eq. (111) is fulfilled for phase shifts  $\beta_{II}$  and  $\beta_{III}$ , given by

$$\begin{aligned} F_{11} + F_{12} \cos \beta_{II} + F_{13} \cos \beta_{III} &= 0 \\ F_{12} \sin \beta_{II} - F_{13} \sin \beta_{III} &= 0 \\ F_{31} + F_{32} \cos 3\beta_{II} + F_{33} \cos 3\beta_{III} &= 0 \\ F_{32} \sin 3\beta_{II} - F_{33} \sin 3\beta_{III} &= 0. \end{aligned} \quad (112)$$

Eq. (112) have no solution, i.e., for the system with three clocks it is impossible to have both first and third harmonics of the force acting on the beam equal to zero. The stable pendula configuration occurs when the first harmonic is equal to zero, so the phase differences  $\beta_{II}$  and  $\beta_{III}$  can be calculated from the first two equations:

$$\begin{aligned} F_{11} + F_{12} \cos \beta_{II} + F_{13} \cos \beta_{III} &= 0 \\ F_{12} \sin \beta_{II} - F_{13} \sin \beta_{III} &= 0. \end{aligned} \quad (113)$$

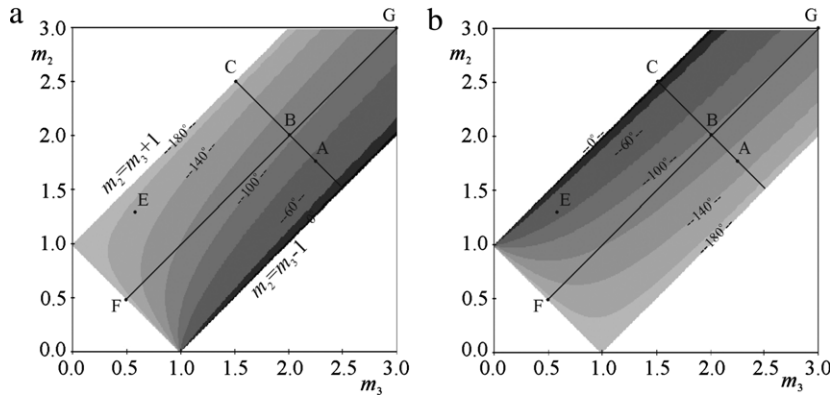


Fig. 54. Phase differences  $\beta_{II}$  and  $\beta_{III}$  versus pendula masses; (a) contour map of  $\beta_{II}$  versus  $m_2$  and  $m_3$ , (b) contour map of  $\beta_{III}$  versus  $m_2$  and  $m_3$ .

Dividing both sides of Eq. (113) by  $F_{11}$  and multiplying by  $m_1$  one gets

$$\begin{aligned} m_1 + m_2 \cos \beta_{II} + m_3 \cos \beta_{III} &= 0, \\ m_2 \sin \beta_{II} - m_3 \sin \beta_{III} &= 0. \end{aligned} \quad (114)$$

To solve Eq. (114) we have been searching for the zero minimum of the following function:

$$H_{13} = (m_1 + m_2 \cos \beta_{II} + m_3 \cos \beta_{III})^2 + (m_2 \sin \beta_{II} - m_3 \sin \beta_{III})^2. \quad (115)$$

The function  $H_{13}$  represents the square of the amplitude of the first harmonic component of the force acting on the beam  $M$ . Notice that the phase differences  $\beta_{II}$  and  $\beta_{III}$  calculated from Eq. (115) do not depend on the models of escapement mechanism and friction.

Our calculations show that for  $m_1 = 1.0$  (kg),  $m_2 = 2.0$  (kg),  $m_3 = 2.0$  (kg) the function  $H_{13}(\beta_{III}, \beta_{II})$  is equal zero for  $\beta_{III} = \beta_{II} = 104.5^\circ$ , i.e., the same values as numerically obtained from the numerical integration of Eqs. (96), (97) (see Fig. 53(a)). For the parameters of Fig. 53(b) ( $m_1 = 1.0$  (kg),  $m_2 = 1.75$  (kg),  $m_3 = 2.25$  (kg)) one gets the same agreement as  $H_{13\min}(\beta_{III}, \beta_{II}) = H_{13}(132^\circ, 73^\circ) = 0$ . The phase synchronization in the system (96), (97) occurs for the phase difference  $\beta_{II}$  and  $\beta_{III}$  given by Eq. (114) when the first harmonic component of the force acting on the beam  $M$  is equal to zero. In this case the beam  $M$  is oscillating with the period three times smaller than the periods of the pendula's oscillations. The motion of the beam influences the oscillations' periods of each pendula in the same way and in the steady state these periods are equal, i.e., the condition for synchronization is fulfilled.

The properties of the solution of Eq. (114) are discussed in Fig. 54(a, b). The contour map showing the values of phase differences  $\beta_{II}$  and  $\beta_{III}$  for  $m_1 = 1.0$  and different masses of the pendula  $m_2$  and  $m_3$  are shown in Fig. 54(a, b). In Fig. 54(a, b) point A ( $m_3 = 2.25$  (kg),  $m_2 = 1.75$  (kg)) represents the configuration of Fig. 53(b) ( $\beta_{II} = 73^\circ$  and  $\beta_{III} = 132^\circ$ ) and point B ( $m_3 = 2.0$  (kg),  $m_2 = 2.0$  (kg) and  $\beta_{II} = \beta_{III} = 104.5^\circ$ ) – this configuration shown in Fig. 54(a). Notice that starting from the symmetrical configuration (point B) due to the simultaneous decrease of value  $m_3$  and increase of value  $m_2$ , phase difference  $\beta_{II}$  tends to  $180^\circ$  and phase difference  $\beta_{III}$  tends to zero. In the limit case – point C – pendula mass  $m_2 = 2.5$  (kg) and  $m_3 = 1.5$  (kg) create a cluster oscillating in the antiphase to the pendulum mass  $m_2 = 2.5$  (kg) (equal to the mass of the created cluster) as can be seen in Fig. 55(b). When mass  $m_2$  is larger than the sum of the masses  $m_1 + m_3$  (white region in Fig. 54(a, b)) Eq. (114) has no solution and instead of phase synchronization, the complete synchronization is observed for all initial conditions. Let us start again with the symmetrical configuration of Fig. 55(a) ( $m_2 = m_3 = 2.0$  (kg)) and decrease the values of  $m_2 = m_3$  and observe the values of phase differences  $\beta_{II} = \beta_{III}$  increase towards  $\pi$  ( $180^\circ$ ). In the limit case (point F) pendula mass  $m_2 = 0.5$  (kg) and  $m_3 = 0.5$  (kg) create a cluster which oscillates in the antiphase with pendulum mass  $m_1 = 1.0$  (kg) as shown in Fig. 55(c). On the other hand, with the increase of the values of  $m_2 = m_3$ , phase differences  $\beta_{II} = \beta_{III}$  decrease (for example to  $98.5^\circ$  for  $m_2 = m_3 = 3.0$  (kg) – point G in Fig. 54(a, b)). In the limit as  $m_2 = m_3$  tends to infinity,  $\beta_{II} = \beta_{III}$  tends to  $90^\circ$  – the corresponding configuration is shown in Fig. 55(d).

One can conclude that the phase synchronization can occur when the mass of the largest pendulum is smaller than the sum of the masses of two other pendula. If  $m_1 > m_2$  and  $m_1 > m_3$  one gets

$$m_1 \leq m_2 + m_3. \quad (116)$$

Relation (116) gives the necessary condition for the phase synchronization in the system with three pendulum clocks.

Notice that the method of the phase shift estimation (Eqs. (110)–(115)) and particularly necessary condition (116), derived for three pendula, can be generalized to any number of pendula synchronized in three clusters. In this case one can rewrite condition (116) in the form:

$$\bar{m}_1 = \bar{m}_2 + \bar{m}_3, \quad (117)$$

where  $\bar{m}_1$ ,  $\bar{m}_2$  and  $\bar{m}_3$  are respectively the sum of pendula's masses in the first, second and third cluster.

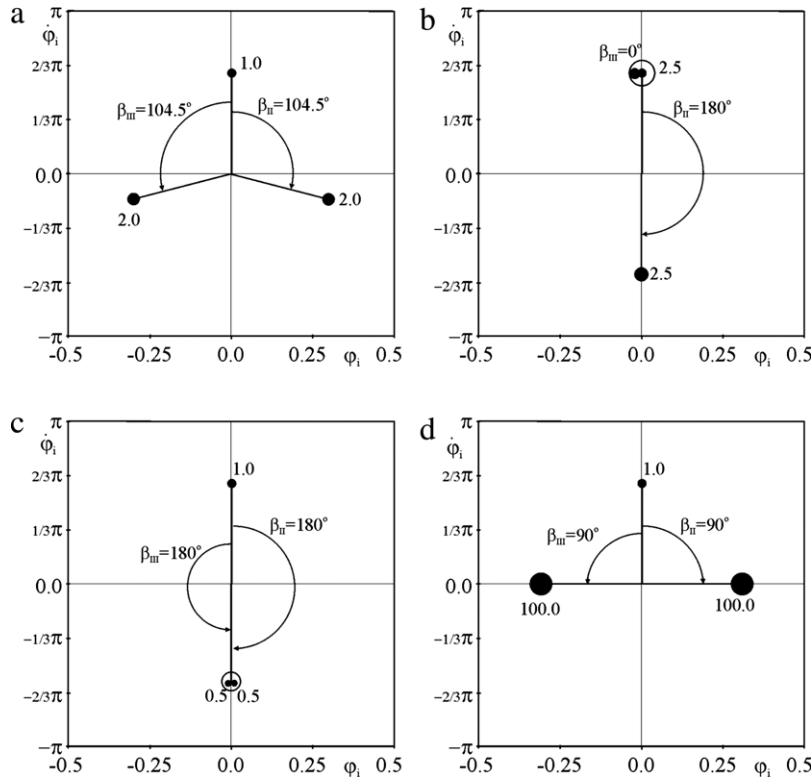


**Fig. 55.** Synchronization configurations of three pendula for various values of  $m_2$  and  $m_3$ : (a)  $m_3 = m_2 = 2.0$  (kg), (b)  $m_3 = 1.5$  (kg),  $m_2 = 2.5$  (kg), (c)  $m_3 = m_2 = 0.5$  (kg), (d)  $m_3 = m_2 = 100.0$  (kg).

#### (b) Four clocks ( $n = 4$ )

In the system with four pendulum clocks one can observe two types of synchronization; (i) the complete synchronization of all pendula (pendula oscillate in antiphase with the oscillations of the beam), (ii) the phase synchronization between a cluster of two synchronized pendula and two other pendula (two clusters with one pendulum in each of them). In the case of phase synchronization different pendula can create the cluster (there are six different possibilities: 1 + 2, 1 + 3, 1 + 4, 2 + 3, 2 + 4, 3 + 4). The necessary condition for the existence of particular configuration (117) states: the mass of the largest cluster (with one or two pendula) has to be smaller than the sum of two other clusters' masses.

Consider a few examples of the phase synchronization for the beam mass  $M = 10.0$  and four pendula mass  $m_1 = 1.0$  (kg),  $m_2 = 1.75$  (kg),  $m_3 = 2.25$  (kg),  $m_4 = 2.0$  (kg). For these parameters the above condition of the existence of cluster (117) is fulfilled by three pairs of pendula: 1 + 2, 1 + 3 and 1 + 4. The corresponding configurations are shown in Fig. 56(a)–(c). The same phase differences as observed in Fig. 56(a)–(c) can be calculated from the function  $H_{13}$  given by Eq. (115). Notice that in this case the cluster has to be considered as a single pendulum with mass equal to the total mass of the pendula in the cluster.

#### (c) Five clocks ( $n = 5$ )

In the system with five pendulum clocks we observed three different types of synchronization: (i) complete synchronization of all pendula, (ii) phase synchronization of three clusters and (iii) phase synchronization of five pendula.

The examples of synchronization configurations for the system with five pendulum clocks are shown in Fig. 57(a)–(d). Fig. 57(a) presents the results obtained for:  $M = 10.0$  (kg),  $m_1 = m_2 = m_3 = 1.0$  (kg),  $m_4 = 0.75$  (kg),  $m_5 = 1.25$  (kg). Observe the phase synchronization with the following phase differences:  $\beta_{II} = 124.5^\circ$ ,  $\beta_{III} = 162^\circ$ ,  $\beta_{IV} = 71^\circ$ ,  $\beta_V = 77^\circ$ . In this configuration the beam  $M$  is in rest. Notice that contrary to the case of identical clocks (Section 5.3.1) the obtained configuration is unsymmetrical. The configuration obtained for the same parameter values but different initial phases is shown in Fig. 57(b). The two clusters with masses:  $(m_1 + m_4) = 1.75$  (kg),  $(m_2 + m_3) = 2.0$  (kg) and pendulum 5 ( $m_5 = 1.25$  (kg)) are phase synchronized. The phase differences are respectively  $\beta_{II} = 142^\circ$  and  $\beta_{III} = 98^\circ$ . Different three clusters' configurations are shown in Fig. 57(c, d). Fig. 57(c) shows the configuration of the clusters which consist respectively of pendula 1 and 3 ( $m_1 + m_3 = 3$  (kg)), pendulum 4 ( $m_4 = 0.75$  (kg)) and pendulum 2 and 5 ( $m_2 + m_5 = 2.25$  (kg)). The phase differences between the clusters are given by  $\beta_{II} = 80^\circ$  and  $\beta_{III} = 161^\circ$ . The configuration of the clusters consisting of pendulum 1 ( $m_1 = 1.0$  (kg)), pendula 2 and 4 ( $m_2 + m_4 = 1.75$  (kg)) and pendula 3 and 5 ( $m_3 + m_5 = 2.25$  (kg)) with phase differences  $\beta_{II} = 72^\circ$  and  $\beta_{III} = 133^\circ$  is shown in Fig. 57(d). The last possible configuration with clusters consisting of pendulum 1 ( $m_1 = 1.0$  (kg)), pendula 2 and 4 ( $m_2 + m_4 = 2.0$  (kg)), pendula 3 and 5 ( $m_3 + m_5 = 2.0$  (kg)) and phase

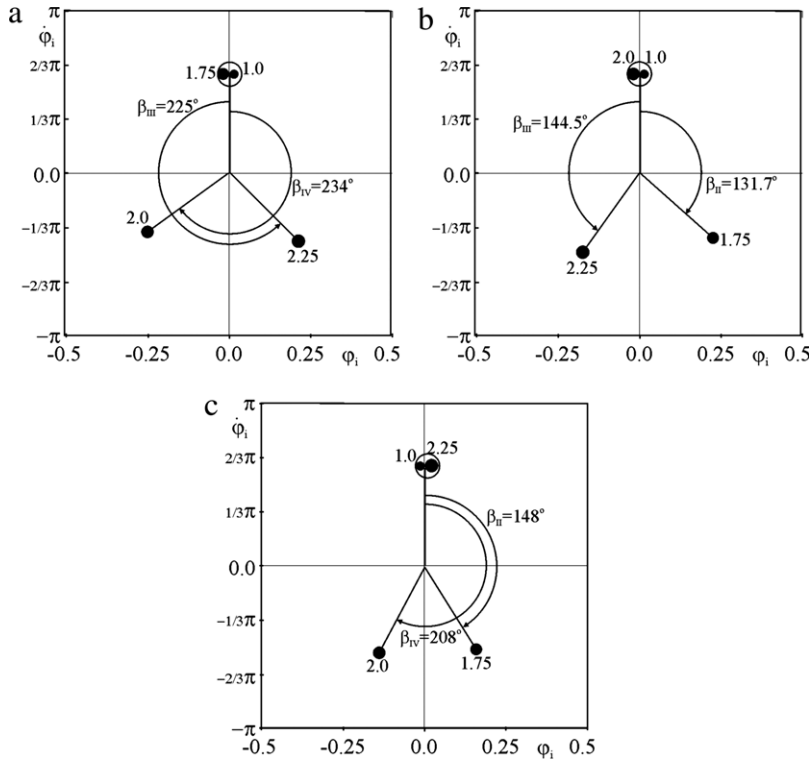


**Fig. 56.** Synchronization configurations for four pendula:  $M = 10.0$  (kg); (a) pendula  $m_1 = 1.0$  (kg),  $m_2 = 1.75$  (kg) form the cluster,  $\beta_{I0} = 0^\circ$ ,  $\beta_{III0} = 73^\circ$ ,  $\beta_{III0} = 130^\circ$ ,  $\beta_{IV0} = 270^\circ$ , (b) pendula  $m_1 = 1.0$  (kg),  $m_4 = 2.0$  (kg) form the cluster,  $\beta_{I0} = 0^\circ$ ,  $\beta_{III0} = 73^\circ$ ,  $\beta_{III0} = 130^\circ$ ,  $\beta_{IV0} = 340^\circ$ , (c) pendula  $m_1 = 1.0$  (kg),  $m_3 = 2.25$  (kg) form the cluster,  $\beta_{I0} = 0^\circ$ ,  $\beta_{III0} = 140^\circ$ ,  $\beta_{III0} = 340^\circ$ ,  $\beta_{IV0} = 220^\circ$ .

differences  $\beta_{II} = 104.5^\circ$  and  $\beta_{III} = 104.5^\circ$  has been already shown in Fig. 53(a). Other three cluster configurations are either equivalent to these presented in Fig. 57(a)–(c) and 3(a) or do not fulfill condition (117). (In this case where  $\bar{m}_1$ ,  $\bar{m}_2$  and  $\bar{m}_3$  indicate the total masses of each of three clusters).

Phase differences  $\beta_{II}$ ,  $\beta_{III}$ ,  $\beta_{IV}$  and  $\beta_V$  can be approximately estimated on the base of the linear approximation derived in Section 5.3.1 in the case of five pendulum clocks the forces acting on the beam  $M$  are equal to zero when:

$$\begin{aligned}
 F_{11} + F_{12} \cos \beta_{II} + F_{13} \cos \beta_{III} + F_{14} \cos \beta_{IV} + F_{15} \cos \beta_V &= 0 \\
 F_{12} \sin \beta_{II} - F_{13} \sin \beta_{III} + F_{14} \sin \beta_{IV} - F_{15} \sin \beta_V &= 0 \\
 F_{31} + F_{32} \cos 3\beta_{II} + F_{33} \cos 3\beta_{III} + F_{34} \cos 3\beta_{IV} + F_{35} \cos 3\beta_V &= 0 \\
 F_{32} \sin 3\beta_{II} - F_{33} \sin 3\beta_{III} + F_{34} \sin 3\beta_{IV} - F_{35} \sin 3\beta_V &= 0.
 \end{aligned} \tag{118}$$

Contrary to the case with three clocks (112) now we have four equations with four unknown phase differences  $\beta_{II}$ ,  $\beta_{III}$ ,  $\beta_{IV}$  and  $\beta_V$  and it is possible to find the solution which fulfills all equations (118). For such values of  $\beta_{II}$ ,  $\beta_{III}$ ,  $\beta_{IV}$  and  $\beta_V$  both the first and the third harmonic of the force acting on the beam  $M$  vanish and the beam is in rest. Dividing the first two of Eq. (118) by  $F_{11}$  and the other two by  $F_{31}$  and multiplying all equations by  $m_1$  one gets:

$$\begin{aligned}
 m_1 + m_2 \cos \beta_{II} + m_3 \cos \beta_{III} + m_4 \cos \beta_{IV} + m_5 \cos \beta_V &= 0 \\
 m_2 \sin \beta_{II} - m_3 \sin \beta_{III} + m_4 \sin \beta_{IV} - m_5 \sin \beta_V &= 0 \\
 m_1 + m_2 \cos 3\beta_{II} + m_3 \cos 3\beta_{III} + m_4 \cos 3\beta_{IV} + m_5 \cos 3\beta_V &= 0 \\
 m_2 \sin 3\beta_{II} - m_3 \sin 3\beta_{III} + m_4 \sin 3\beta_{IV} - m_5 \sin 3\beta_V &= 0.
 \end{aligned} \tag{119}$$

Eq. (119) have been solved by the method of searching for the zero minimum of the functions  $H_{15}$  and  $H_{35}$ :

$$\begin{aligned}
 H_{15} &= (m_1 + m_2 \cos \beta_{II} + m_3 \cos \beta_{III} + m_4 \cos \beta_{IV} + m_5 \cos \beta_V)^2 \\
 &\quad + (m_2 \sin \beta_{II} - m_3 \sin \beta_{III} + m_4 \sin \beta_{IV} - m_5 \sin \beta_V)^2 \\
 H_{35} &= (m_1 + m_2 \cos 3\beta_{II} + m_3 \cos 3\beta_{III} + m_4 \cos 3\beta_{IV} + m_5 \cos 3\beta_V)^2 \\
 &\quad + (m_2 \sin 3\beta_{II} - m_3 \sin 3\beta_{III} + m_4 \sin 3\beta_{IV} - m_5 \sin 3\beta_V)^2.
 \end{aligned} \tag{120}$$

The functions  $H_{15}$  and  $H_{35}$  represent respectively the square of the amplitude of the first and the third harmonic components of the force acting on the beam  $M$ . Notice that the phase differences  $\beta_{II}$ ,  $\beta_{III}$ ,  $\beta_{IV}$  and  $\beta_V$  calculated from Eq. (119) do not depend on the models of the escapement mechanism and friction.

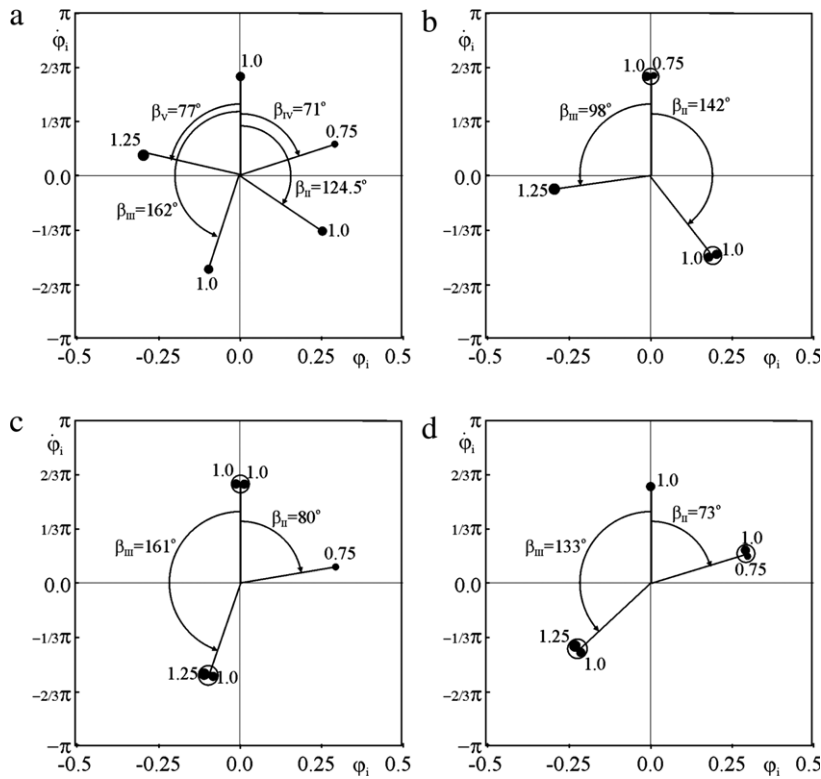


**Fig. 57.** Synchronization configurations of five pendula:  $M = 10.0$  (kg); (a)  $m_1 = m_2 = m_3 = 1.0$  (kg),  $m_4 = 0.75$  (kg),  $m_5 = 1.25$  (kg); (a) configuration of five clusters, (b) configuration of three clusters mass 1.75, 2.0, 1.25 (kg), (c) configuration of three clusters of the following masses 2.0, 0.75, 2.25 (kg), (d) configuration of three clusters of the following masses 1.0, 1.75, 2.25 (kg).

The dependence of the phase differences  $\beta_{II}$ ,  $\beta_{III}$ ,  $\beta_{IV}$  and  $\beta_V$ , i.e., the values for which functions  $H_{15}$  and  $H_{35}$  have zero minimum, on the parameters  $m_1$ ,  $m_2$ ,  $m_3$ ,  $m_4$  and  $m_5$  is partially described in Fig. 58(a)–(d). To reduce the dimensionality and allow the visualization we consider  $m_1 = m_2 = m_3 = 1.0$  (kg) (three identical pendula), and allow  $m_4$  and  $m_5$  to vary in the interval  $[0.0, 1.5]$ . The contour maps of  $\beta_{II}$ ,  $\beta_{III}$ ,  $\beta_{IV}$  and  $\beta_V$  are shown respectively in Fig. 58(a)–(d). The phase differences  $\beta_{II}$  and  $\beta_{III}$  are shown in the interval  $[90^\circ, 180^\circ]$  and  $\beta_{IV}$ ,  $\beta_V$  in the interval  $[0^\circ, 90^\circ]$ . In this a few characteristic points are indicated. Point A ( $m_4 = 0.75$  (kg),  $m_5 = 1.25$  (kg)) represents the phase synchronization of five pendula:  $m_1 = m_2 = m_3 = 1.0$  (kg),  $m_4 = 0.75$  (kg),  $m_5 = 1.25$  (kg), with phase differences given by:  $\beta_{II} = 124.5^\circ$ ,  $\beta_{III} = 162^\circ$ ,  $\beta_{IV} = 71^\circ$ ,  $\beta_V = 77^\circ$  (this configuration is shown in Fig. 57(a)). On the line  $m_4 = m_5$  the symmetrical configurations are located. The symmetrical configuration of five identical clocks is indicated by point B. Point C ( $m_5 = m_4 = 0.75$  (kg)) is characteristic for the configuration for  $m_1 = m_2 = m_3 = 1.0$  (kg) and  $m_4 = m_5 = 0.75$  (kg) with phase differences  $\beta_{II} = \beta_{III} = 145.5^\circ$  and  $\beta_{IV} = \beta_V = 65.5^\circ$ . The configuration of the point D ( $m_5 = m_4 = 0.5$  (kg)) is shown in Fig. 59(a). The phase differences for pendula 2 and 3 ( $m_2 = m_3 = 1.0$  (kg)) are equal to  $\beta_{II} = \beta_{III} = 180^\circ$ , and for pendula 4 and 5  $\beta_{IV} = \beta_V = 0^\circ$ . It is a limit case in which two clusters of two and three pendula, but with the same mass  $m_1 + m_4 + m_5 = m_2 + m_3 = 2.0$  (kg), are in antiphase to each other. Point E represents the system with  $m_5 = m_4 = 0.0$ , i.e., the system with three clocks,  $m_1 = m_2 = m_3 = 1.0$  (kg) and phase differences  $\beta_{II} = \beta_{III} = 120^\circ$ . Point F ( $m_5 = m_4 = 1.5$  (kg)) describes the configuration for  $m_2 = m_3 = 1.0$  (kg),  $m_4 = m_5 = 1.5$  (kg) and phase differences  $\beta_{II} = \beta_{III} = 143^\circ$  and  $\beta_{IV} = \beta_V = 78^\circ$ . Observe that with the further increase of the masses of pendula 4 and 5, i.e., for  $m_5 = m_4 \rightarrow \infty$ , phase differences  $\beta_{IV} = \beta_V \rightarrow 90^\circ$ , so pendula 4 and 5 oscillate in antiphase, and phase differences  $\beta_{II} = \beta_{III} \rightarrow 120^\circ$ . In this case we have the co-existence of two configurations; two large pendula with equal masses  $m_5 = m_4$  oscillate in the antiphase and other pendula with masses  $m_1 = m_2 = m_3 = 1.0$  (kg) are phase synchronized with phase differences  $\beta_{II} = \beta_{III} = 120^\circ$  as shown in Fig. 59(b). Point G is the crossing point of the lines  $m_4 = 1.5 - m_5$  and  $m_4 = m_5 - 1$ . It represents the system with  $m_4 = 0.25$  (kg) and  $m_5 = 1.25$  (kg), in which the phase difference of pendulum 3 ( $m_3 = 1.0$  (kg)) is equal to  $\beta_{III} = 180^\circ$  and this pendulum is in the antiphase to pendulum 1 ( $m_1 = 1$  (kg)). Phase differences of pendula 2 ( $m_2 = 1.0$  (kg)) and 4 ( $m_4 = 0.25$  (kg)) are  $\beta_{II} = \beta_{IV} = 90^\circ$ , which means that these pendula create a cluster which is in antiphase to pendulum 5 ( $m_5 = 1.0$  (kg)) for which  $\beta_V = 90^\circ$ . This is a special case when there are four clusters with antiphase synchronization in pairs – see Fig. 57(c). The symmetrical configuration to the one described in Fig. 59(c) is shown in Fig. 59(d) and represented by point H in Fig. 58(a)–(d).

Similar contour maps can be obtained for different intervals of phase differences  $\beta_{II}$ ,  $\beta_{III}$ ,  $\beta_{IV}$  and  $\beta_V$ . For some values of the parameters  $m_4$  and  $m_5$  there exist more than one phase synchronization configurations of five clusters, i.e.,  $m_4$  and  $m_5$

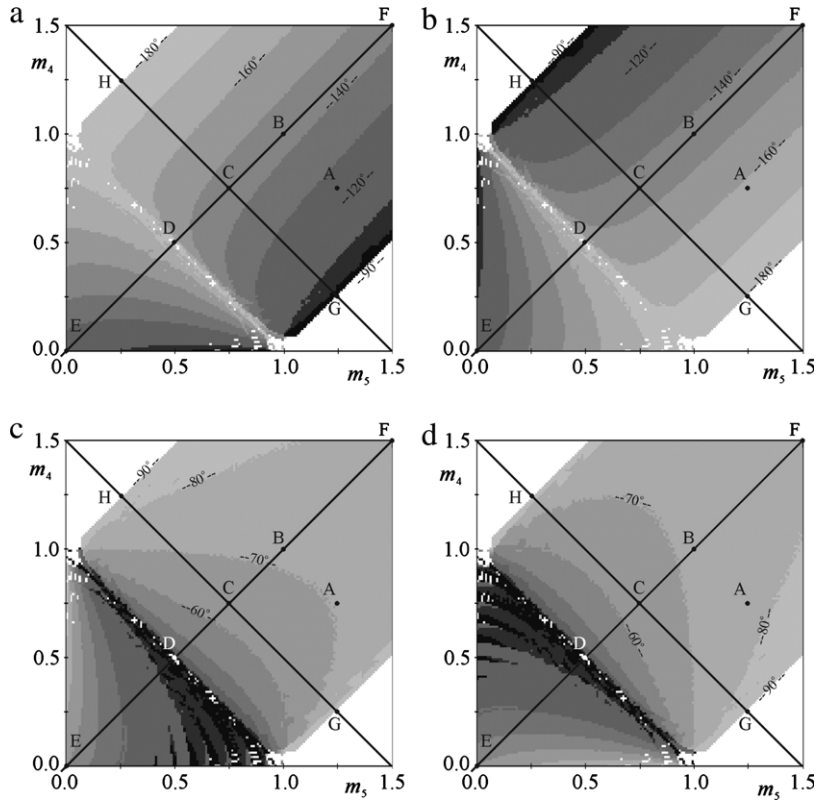


**Fig. 58.** Contour maps of phase differences (a)  $\beta_{II}$ , (b)  $\beta_{III}$ , (c)  $\beta_{IV}$ , (d)  $\beta_V$ , versus pendula masses  $m_4$  and  $m_5$ ;  $m_1 = m_2 = m_3 = 1.0$  (kg).

there exist more than one different set of phase differences  $\beta_{II}$ ,  $\beta_{III}$ ,  $\beta_{IV}$  and  $\beta_V$  for which functions  $H_{15}$  and  $H_{35}$  have zero minima.

The method of the phase shifts estimation derived for five pendula (Eqs. (118)–(120)) can be generalized to any number of pendula synchronized in five clusters. Substituting the total masses of clusters  $\bar{m}_{1-5}$  instead of pendulum masses  $m_{1-5}$  one gets the equations which allow the estimation of the phase shifts between clusters.

#### 5.4. Discussion

It has been shown that besides the complete synchronization of all pendulum clocks and the creation of the pairs of the pendulum clocks synchronized in the anti-phase (for even  $n$ ), the pendula can be grouped either in three or five clusters only. The pendula in the clusters perform complete synchronization and the clusters are in the form of the phase synchronization characterized by a constant phase difference between the pendula given by (106), (108), (114) and (119).

The results of the numerical studies for  $n$  pendulum clocks show either the complete synchronization or the phase synchronization in three or five clusters. To explain why other cluster configurations are not possible go back to the approximation given by Eq. (102). The pendula act on the beam  $M$  with the force which consists only of the first and the third harmonics of the pendula's oscillations frequency  $\alpha$ . Three clusters configuration occurs when the first harmonic of this force is equal to zero and the system tends to five clusters configuration when both harmonics are equal to zero. This result is exactly the same in the cases of identical and nonidentical clocks and is general for the problems of clocks' synchronization. Contrary to the case of identical clocks the clustering in three and five clusters is easily observable for both even and odd numbers of the clocks. For an even number of clocks the creation of the pairs of clocks synchronized in the antiphase is possible only in the special non-robust case of two groups of identical clocks. Due to the assumption (98) and the small swings of the pendula ( $\Phi < 2\pi/36$ ) other harmonics do not exist (or are extremely small). One can expect the appearance of other numbers of clusters, when the pendula's swings are larger and their periodic oscillations will be described by higher harmonic components, but this is not the case of the pendula's clocks.

We studied the systems with up to 100 clocks. It has been found that for larger  $n$  and randomly distributed differences of pendula masses, three clusters configurations are more probable than five clusters configurations. As an example consider the case of 20 clocks shown in Fig. 60. After the initial transient the pendula with randomly distributed masses  $m_i = 1.0 \pm 0.1$  create three clusters with respectively 6, 7 and 7 pendula. Noticed that as described in Section 5.3 the beam is oscillating with a small amplitude.

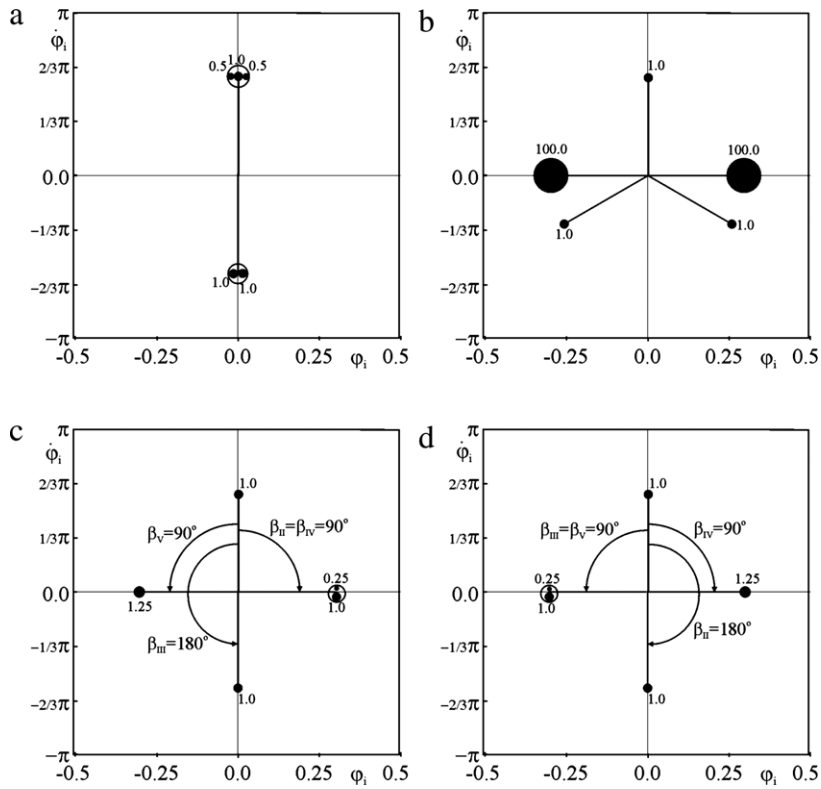


**Fig. 59.** Synchronization configurations of five pendula; (a) antiphase configuration of two clusters of the mass 2.0 (kg) each, (b) coexistence of two heavy pendula in antiphase with the configuration of three pendula mass 1.0 (kg) each, (c) coexistence of two pairs of two clusters in antiphase; (d) mirror image of previous configuration.

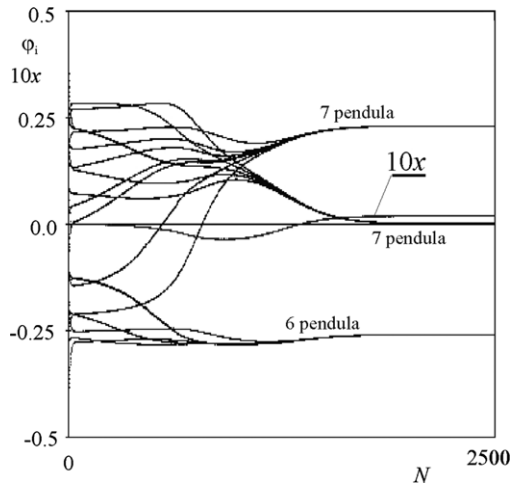


**Fig. 60.** Synchronization of 20 clocks:  $m_i = 1.0$  (kg),  $l_i = 0.2485$  (m),  $M = 10.0$  (kg),  $k_x = 118.4$  (N/m),  $c_x = 24.0$  (N s/m).  $N$  on the parallel axis indicated the number of periods of the pendula oscillations.

### 6. Conclusions

In the considered system of two clocks suspended on the horizontally movable beam we identified the following types of synchronizations: (i) the complete synchronization during which the pendula’s displacements fulfill the relation  $\varphi_1(t) = \varphi_2(t)$  and the phase shift between pendula’s displacements  $\varphi_1(t)$  and  $\varphi_2(t)$  is equal to zero, (ii) the almost complete synchronization during which the pendula’s displacements fulfill the relation  $\varphi_1(t)\varphi_2(t)$  and the phase shift between pendula’s displacements  $\varphi_1(t)$  and  $\varphi_2(t)$  is close to zero, (iii) antiphase synchronization during which the pendula’s displacements fulfill the relation  $\varphi_1(t) = -\varphi_2(t)$  and the phase shift between the pendulum displacements is equal to  $\pi$

(180°), (iv) almost antiphase synchronization during which the phase shift between the pendula's displacements is close to 180°. Additionally, for the pendula with the same lengths there exists the possibility of long period synchronization during which the difference of the pendula's displacements  $\varphi_1 - \varphi_2$  is a periodic function of time and chaotic behavior of the clocks' pendula [45] and the chaotic behavior. The pendula with different lengths can oscillate with different periods and one can observe 1:2, 1:3, 2:3, etc. synchronizations. Note that types (i) and (iii) are possible only for nonrobust case of identical pendulum masses ( $m_1 = m_2$ ). The transfer of the energy from one clock to another through the beam has been identified as the cause of the observed synchronous cases. For cases (ii) and (iv) pendula's energy balance looks differently as can be shown in Fig. 42(a, c).

The continuous model Eqs. (68), (69) in which the escapement mechanism is modeled by van der Pol's type of damping can explain the main features of the system, i.e., the transfer of energy through the beam. The consideration of the discontinuous model (Eq. (27), (28)) gives more accurate results than the studies of the continuous model (68) and (69) [8,37,40] as continuous model cannot take into account the possibility of switch-off of the escapement mechanism when the pendula's oscillations are too small.

In the array of non-identical pendulum clocks hanging from an elastically fixed horizontal beam one can also observe the phenomenon of the synchronization. Besides the complete synchronization of all pendulum clocks, the pendula can be grouped either in three or five clusters only. The pendula in the clusters perform complete synchronization and the clusters are in the form of the phase synchronization characterized by a constant phase difference between the pendula given by Eq. (114) for three pendula and (119) for five pendula. All the pendula's configurations reported in this paper are stable and robust as they exist for the given sets of system (96), (97) parameters which have positive Lebesgue measure. We give evidence that the observed behavior is robust in the phase space and can be observed in real experimental systems. The clustering in three or five clusters is possible for any number of pendulum clock  $n$  if the solution of Eq. (114) or Eq. (119) exists. In the considered range of  $n = 100$  the solution of at least one of these equations exists. It should be mentioned here that it is easier to observe the clustering phenomena for an odd number of pendulum clocks.

In the considered case the clocks' clustering phenomena take place far below the resonances for both longitudinal and transverse oscillations of the beam when the displacements of the beam are very small. We can add that the similar phenomena have been observed in the system of  $n$  pendula hanging from the string in which transversal and longitudinal oscillations of the string are considered [35].

Finally, we briefly discuss the influence of noise on the synchronization of clocks. Noise is inevitably present in experimental and natural systems. Generally noise may influence synchronization in different ways. Usually, it has a degrading effect, e.g. inducing phase slips of phase-locked oscillators or resulting in an intermittent loss of synchronization. On the other hand, when influencing all coupled systems in the same way, noise may play a constructive role in enhancing synchronization (noise-induced synchronization) or, more generally, in inducing more order [99]. Noise has been taken into account in the construction of the pendulum clocks since XVII century. To reduce the effect on the sea motion on the accuracy of the marine clocks, long heavy pendulums have been used. Going back to the Huygens' experiment we can conclude that it would be easier to perform it on the ship and with a stable sea conditions. In this case the sea oscillations influence the oscillations of both clocks' pendula in the same way inducing synchronizations. On the other hand in the case of rough sea synchronization may not be observed at all as the changes of the sea conditions as too often (time necessary to achieve synchronization is longer than intervals between changes of the sea conditions).

To conclude, we can state that the results presented in this review give evidence that Huygens in his famous experiment was unable to observe antiphase synchronization as stated in his letters [5] but we give evidence that he was able to observe an almost antiphase synchronization of two pendulum clocks. In his times the distinction between antiphase and almost antiphase synchronization for the clock with similar masses of the pendula was impossible. At the end, it should be mentioned that the analysis of coupled clocks has much more applications than in mechanics, especially biological clocks and synthetic biology or various other coupled self-sustained oscillators in physiology, engineering (e.g. power grids, rotors operating on the same base) etc.

## Acknowledgments

This work has been supported by the Foundation for Polish Science, Team Programme – Project No TEAM/2010/5/5. PP acknowledges the support from Foundation for Polish Science (the START fellowship).

## References

- [1] W.J.H. Andrewes, Clocks and watches: the leap to precision, in: S. Macey (Ed.), Encyclopedia of Time, Taylor & Francis, London, 1994.
- [2] I.W. Milham, Time and Timekeepers, New York: MacMillan, New York, 1945.
- [3] J.G. Yoder, Unrolling Time: Christiaan Huygens and the Mathematization of Nature, Cambridge University Press, Cambridge, 1990.
- [4] D. Sobel, W.J.H. Andrewes, The Illustrated Longitude, Walker and Co., New York, 1998.
- [5] C. Huygens, Letter to de Sluse, In: Oeuvres Complètes de Christian Huygens (letters; no. 1333 of 24 February 1665, no. 1335 of 26 February 1665, no. 1345 of 6 March 1665), (Societe Hollandaise Des Sciences, Martinus Nijhoff, La Haye, 1893).
- [6] A. Pikovsky, M. Roesenblum, J. Kurths, Synchronization: an Universal Concept in Nonlinear Sciences, Cambridge University Press, Cambridge, 2001.
- [7] I.I. Blekhnman, Synchronization in science and technology, ASME Press, New York, 1988.
- [8] S. Boccaletti, J. Kurths, G. Osipov, D.L. Valladares, C. Zhou, The synchronization of chaotic systems, Phys. Rep. 366 (2002) 1–101.
- [9] S. Boccaletti, Louis M. Pecora, A. Pelaez, Unifying framework for synchronization of coupled dynamical systems, Phys. Rev. E63 (2001) 066219.

- [10] S. Boccaletti, V. Latora, Y. Moreno, M. Chavez, D.-U. Hwang, Complex networks: structure and dynamics, *Phys. Rep.* 424 (2006) 175–308.
- [11] M. Golubitsky, I. Stewart, P.-L. Buono, J.J. Collins, Symmetry in locomotor central pattern generators and animal gaits, *Nature* 401 (1999) 693–695.
- [12] E. Rodriguez, N. George, J.-P. Lachaux, J. Martinerie, B. Renault, F.J. Varela, Perception's shadow: long-distance synchronization of human brain activity, *Nature* 397 (1999) 430–433.
- [13] T.M. Antonsen Jr., R.T. Faghih, M. Girvan, E. Ott, J. Platig, External periodic driving of large systems of globally coupled phase oscillators, *Chaos* 18 (2008) 037112.
- [14] S.H. Strogatz, I. Stewart, Coupled oscillators and biological synchronization, *Scient. Am.* 269 (1993) 102–109.
- [15] I.Z. Kiss, Y. Zhai, J.L. Hudson, Emerging coherence in a population of chemical oscillators, *Science* 296 (2002) 1676–1677.
- [16] Y. Kuramoto, T. Yamada, Pattern formation in oscillatory chemical reactions, *Progr. Theoret. Phys.* 56 (1976) 724–740.
- [17] Y. Kuramoto, *Chemical Oscillations, Waves and Turbulence*, Springer, New York, 1984.
- [18] S.H. Strogatz, *Sync: The Emerging Science of Spontaneous Order*, Penguin Science, London, 2004.
- [19] S. Yamaguchi, H. Isejima, T. Matsuo, R. Okura, K. Yagita, M. Kobayashi, H. Okamura, Synchronization of Cellular Clocks in the Suprachiasmatic Nucleus, *Science* 302 (2003) 1408–1414.
- [20] M.M. Abdulreheem, E. Ott, Low dimensional description of pedestrian-induced oscillation of the Millennium Bridge, *Chaos* 19 (2009) 013129.
- [21] P. Dallard, A.J. Fitzpatrick, A. Flint, S. Le Bourva, A. Low, R.M.R. Smith, M. Willford, The London Millennium Footbridge, *Struct. Eng.* 79 (2001) 17–33.
- [22] P. Dallard, A.J. Fitzpatrick, A. Flint, A. Low, R.M.R. Smith, M. Willford, M. Roche, London Millennium Bridge: Pedestrian-Induced Lateral Vibration, *J. Bridge Eng.* 6 (2001) 412–417.
- [23] B. Eckhardt, E. Ott, S.H. Strogatz, D. Abrams, A. Mcrobie, Modeling walker synchronization on the Millennium Bridge, *Phys. Rev. E* 75 (2007) 021110.
- [24] S. Nakamura, Model for Lateral Excitation of Footbridges by Synchronous Walking, *J. Struct. Eng.* 130 (2004) 32–37.
- [25] D.E. Newland, Vibration of the London Millennium Bridge: cause and cure, *Int. J. Acoust. Vibr.* 8 (1) (2003) 9–14.
- [26] E. Ott, T.M. Antonsen, Low dimensional behavior of large systems of globally coupled oscillators, *Chaos* 18 (2008) 037113.
- [27] C. Huygens, *Horologio Oscillatorium*, Apud F. Muquet, Parisii, 1673, English translation: Christiaan Huygens's the pendulum clock or geometrical demonstrations concerning the motion of pendula as applied to clocks, Iowa State University Press, Ames, 1986.
- [28] C. Huygens, *Christiaan Huygens' The Pendulum Clock or Geometrical Demonstrations Concerning the Motion of Pendula as Applied to Clocks*, Translated by R.J. Blackwell, The Iowa State University Press, Ames, Iowa, 1988.
- [29] T. Birch, The history of The Royal Society of London for improving of natural knowledge, in which the most considerable of those papers communicated to the Society, which have hitherto not been published, are inserted in their proper order, as a supplement to the Philosophical Transactions, vol. 2, Johnson, London, 1756, (Reprint 1968).
- [30] G.H. Baillie, C. Clutton, C.A. Ilbert, *Britten's Old Clocks and Watches and their Makers*, Bonanza Books, New York, 1956.
- [31] F.J. Britten, *The Watch and Clockmaker's Handbook*, W. Kent & Co., London, 1881 (2-nd edition E.F. & N. Spon, London, 1896).
- [32] F.J. Britten, Britten's old clocks and watches and their makers; a historical and descriptive account of the different styles of clocks and watches of the past in England and abroad containing a list of nearly fourteen thousand makers, Methuen, London, 1973.
- [33] M. Bennet, M.F. Schatz, H. Rockwood, K. Wiesenfeld, Huygens's clocks, *Proc. R. Soc. London A* 458 (2002) 563–579.
- [34] A.Yu. Pogromsky, V.N. Belykh, H. Nijmeijer, Controlled synchronization of pendula, in: *Proceedings of the 42nd IEEE Conference on Design and Control* (2003), Maui, Hawaii, pp. 4381–4385.
- [35] A.Yu. Kanunnikov, R.E. Lamper, Synchronization of pendulum clocks suspended on an elastic beam, *J. Appl. Mech. Theor. Phys.* 44 (2003) 748–752.
- [36] M. Senator, Synchronization of two coupled escapement-driven pendulum clocks, *Journal Sound Vibration* 291 (2006) 566–603.
- [37] R. Dilao, Antiphase and in-phase synchronization of nonlinear oscillators: the Huygens's clocks system, *Chaos* 19 (2009) 023118.
- [38] M. Kumon, R. Washizaki, J. Sato, R.K.I. Mizumoto, Z. Iwai, Controlled synchronization of two 1-DOF coupled oscillators, in: *Proceedings of the 15th IFAC World Congress*, Barcelona, 2002.
- [39] A.L. Fradkov, B. Andrievsky, Synchronization and phase relations in the motion of two pendulum system, *Int. J. Non-linear Mech.* 42 (2007) 895–901.
- [40] J. Pantaleone, Synchronization of metronomes, *Am. J. Phys.* 70 (2002) 992–1000.
- [41] H. Ulrichs, M. Mann, U. Parlitz, Synchronization and chaotic dynamics of coupled mechanical metronomes, *Chaos* 19 (2009) 043120.
- [42] K. Czolczynski, P. Perlikowski, A. Stefanski, T. Kapitaniak, Clustering of Huygens' Clocks, *Progr. Theoret. Phys.* 122 (2009) 1027–1033.
- [43] K. Czolczynski, P. Perlikowski, A. Stefanski, T. Kapitaniak, Clustering and synchronization of Huygens' clocks, *Physica A* 388 (2009) 5013–5023.
- [44] K. Czolczynski, P. Perlikowski, A. Stefanski, T. Kapitaniak, Huygens' odd sympathy experiment revisited, *Internat. J. Bifur. Chaos* 21 (2011) 2047–2056.
- [45] K. Czolczynski, P. Perlikowski, A. Stefanski, T. Kapitaniak, Why two clocks synchronize: energy balance of the synchronized clocks, *Chaos* 21 (2011) 023129.
- [46] K. Czolczynski, P. Perlikowski, A. Stefanski, T. Kapitaniak, Clustering of non-identical clocks, *Progr. Theoret. Phys.* 125 (2011) 1–18.
- [47] A.V. Roup, D.S. Bernstein, S.G. Nersesov, W.S. Haddad, V. Chellaboina, Limit cycle analysis of the verge and foliot clock escapement using impulsive differential equations and Poincare maps, *Int. J. Control* 76 (2003) 1685–1698.
- [48] A.L. Rawlings, *The Science of Clocks and Watches*, Pitman, New York, 1944.
- [49] A.M. Lepschy, G.A. Mian, U. Viaro, Feedback control in ancient water and mechanical clocks, *IEEE Trans. Educ.* 35 (1993) 3–10.
- [50] A. Andronov, A. Witt, S. Khaikin, *Theory of Oscillations*, Pergamon, Oxford, 1966.
- [51] F.C. Moon, Chaotic clocks: a paradigm for the evolution of noise in machines, in: G. Rega (Ed.), *IUTAM Symposium Chaotic Dynamics and Control of Systems and Processes in Mechanics*, Kluwer-Springer, New York, 2005, pp. 3–16.
- [52] J. Gimpel, *The Medieval Machine: the Industrial Revolution of the Middle Ages*, Penguin Books, New York, 1976.
- [53] J. Burke, *Connections*, Little and Brown, Boston, 1978.
- [54] W.A. Heiskanen, F.A. Vening meinesz, *The Earth and its Gravity Field*, McGraw-Hill, London, 1958.
- [55] C. Audoin, G. Bernard, S. Lyle, *The Measurement of Time: Time, Frequency, and the Atomic Clock*, Cambridge University Press, Cambridge, 2001.
- [56] E.B. Denison (a.k.a. Lord Grimthorpe), *A Rudimentary Treatise on Clocks and Watches and Bells*, Virtue and Co., London, 1868. Reprinted as *Clocks and Time: Clock and watch Escapements*, 2001.
- [57] D. Glasgow, *Watch and Clock Making*, Cassel & Co., London, 1885.
- [58] M. Headrick, Origin and evolution of the anchor clock escapement, *Control Systems Magazine* 22 (2) (2002) 53–68.
- [59] F.C. Moon, Franz Reuleaux; contributions to 19th century kinematics and theory of machines, *Appl. Mech. Rev.* 56 (2003) 261–285.
- [60] F.C. Moon, P.D. Stiefel, Coexisting chaotic and periodic dynamics in clock escapements, *Phil. Trans. R. Soc. A* 364 (2006) 2539–2563.
- [61] Z. Martinek, J. Rehor, *Mechanische uhren*, Verlag Technik, Berlin, 1996.
- [62] L. Penman, *Practical Clock Escapements*, Clockworks Press Int., Shingle Springs, 1998.
- [63] H.L. Nelthropp, *A Treatise on Watchwork, Past and Present*, E. & F.N. Spon, London, 1873.
- [64] C.M. Cipolla, *Clocks and Culture, 1300 to 1700*, W.W. Norton & Co., New York, 2004.
- [65] M. Lewis, Theoretical hydraulics, automata, and water clocks, in: O. Wikander (Ed.), *Handbook of Ancient Water Technology, Technology and Change in History*, 2, Brill, Leiden, 2000.
- [66] L. White Jr., *Medieval Technology and Social Change*, Oxford University Press, Oxford, 1966.
- [67] J. Needham, Science and civilization in China: Vol. 4, *Physics and Physical Technology, Part 2, Mechanical Engineering*, Caves Books Ltd., Taipei, 1986.
- [68] R. Duchesne, Asia first? *J. Historical Soc.* 6 (2006) 69–91.
- [69] K. Ajram, *Miracle of Islamic Science*, Knowledge House Publisher, Vernon Hills, 1992.
- [70] J.D. North, *God's Clockmaker: Richard of Wallingford and the Invention of Time*, Hambleton, London, 2005.
- [71] D.S. Landes, *Revolution in Time: Clocks and the Making of the Modern World*, Harvard University Press, Cambridge, 1983.
- [72] W.J. Gazely, *Clock and Watch Escapements*, Heywood, London, 1956.
- [73] J.M. Bloxam, On the mathematical theory and practical defects of clock escapements, with a description of a new escapement; and some observations for astronomical and scientific purposes, *Memoirs R. Astron. Soc.* XXII (1854) 103–150.

- [74] F. Bruton, *The Longcase Clock*, F.A. Praeger, New York, 1968.
- [75] E. Bruton, *The History of Clocks and Watches*, Orbis Publication, London, 1979.
- [76] T. Jones, *Splitting the Second: The Story of Atomic Time*, CRC Press, Boston, 2000.
- [77] F. Reuleaux, *The Constructor*, H.H. Supplee, Philadelphia, 1893.
- [78] G.B. Airy, On the disturbances of pendula and balances and the theory of escapements, *Trans. Camb. Phil. Soc.* III (1826) 105–128. Part I (1830), Plate 2.
- [79] P. Berge, Y. Pomeau, C. Vidal, *Order within Chaos*, Herman, Paris, 1984.
- [80] M. Kesteven, On the mathematical theory of clocks, *Am. J. Phys.* 46 (125–129) (1978) 125–129.
- [81] H.K. Khalil, *Nonlinear Systems*, Prentice Hall, New York, 1996.
- [82] O. Mayr, *The Origins of Feedback Control*, MIT Press, Cambridge, 1970.
- [83] D.S. Bernstein, *Escapements, governors, ailerons, gyros, and amplifiers: feedback control and the history of technology*, Michigan State University Report, 2000.
- [84] D.S. Bernstein, Feedback control: an invisible thread in the history of technology, *Control Systems Magazine* 22 (2002) 53–68.
- [85] F.C. Moon, *Chaotic and Fractal Dynamics*, Wiley, New York, 1992.
- [86] F.C. Moon, M.A. Johnson, W.T. Holmes, Controlling chaos in a two well oscillator, *Int. J. Bifur. Chaos* 6 (1996) 337–347.
- [87] F.C. Moon, A.J. Reddy, W.T. Holmes, Experiments in control and anti-control of chaos in a dry friction oscillator, *J. Vibration & Control* 9 (2003) 387–397.
- [88] H. Kauderer, *Nichtlineare Mechanik*, Academia Verlag, Berlin, 1958.
- [89] D.D. Bainov, P.S. Simeonov, *Systems with Impulse Effect: Stability, Theory and Applications*, Ellis Horwood Ltd., London, 1989.
- [90] V. Lakshmikantham, D.D. Bainov, P.S. Simeonov, *Theory of impulsive differential equations*, World Scientific, Singapore, 1989.
- [91] N. Minorski, On synchronization, in: *Proceedings of the International Symposium on Nonlinear Oscillations*, Publishing House of the Academy of Science of USSR, Kiev, 1961.
- [92] P. Liao, R.A. York, A new phase-shifterless beam-scanning technique using arrays of coupled oscillators, *IEEE Trans. Microw. Theory Tech.* 41 (1993) 1810–1815.
- [93] K. Czolczynski, T. Kapitaniak, P. Perlikowski, A. Stefanski, Periodization of Duffing oscillators suspended on elastic structure: Mechanical explanation, *Chaos Solitons Fractals* 32 (2007) 920–926.
- [94] K. Czolczynski, P. Perlikowski, A. Stefanski, T. Kapitaniak, Synchronization of self-excited oscillators suspended on elastic structure, *Chaos Solitons Fractals* 32 (937–943) (2007) 937–943.
- [95] K. Czolczynski, A. Stefanski, P. Perlikowski, T. Kapitaniak, Multistability and chaotic beating of Duffing oscillators suspended on the elastic structure, *J. Sound Vib.* 322 (2008) 513–523.
- [96] T.M. Roberts, Synchronized pedestrian excitation of foot bridges. *Proc. ICE, Bridge Engng* 156 (2003) 155–160.
- [97] S.H. Strogatz, D.M. Abrams, A. McRobie, B. Eckhardt, E. Ott, *Nature* 438 (2005) 43–44.
- [98] D.C. Michaels, Mechanisms of sinoatrial pacemaker synchronization: a new hypothesis, *Circ. Res.* 61 (1987) 704–709.
- [99] G.V. Osipov, J. Kurths, C. Zhou, *Synchronization in Oscillatory Networks*, Springer, Berlin, 2007.
- [100] E.M. Izhikevich, F.C. Hoppensteadt, Slowly coupled oscillators: phase dynamics and synchronization, *SIAM J. Appl. Math.* 63 (2003) 1935–1953.
- [101] D.J. Korteweg, *Les horloges sympathiques de Huygens*, *Archives Neerlandaises*, ser. II, tome XI, Martinus Nijhoff, The Hague, 1906, pp. 273–295.
- [102] G. Dohrn-van Rossum, *History of the Hour: Clocks and Modern Temporal Orders*, Univ. of Chicago Press, Chicago, 1996.
- [103] V.S. Anishchenko, V. Astakhov, A. Neiman, T. Vadivasova, L. Schimansky-Geier, *Nonlinear Dynamics of Chaotic and Stochastic Systems*, Springer, Berlin, 2007.
- [104] T. Kapitaniak, A. Stefanski, Using chaos synchronization to estimate the largest Lyapunov exponent of nonsmooth systems, *Discrete Dyn. Nat. Soc.* 4 (2003) 207–215.
- [105] A. Stefanski, T. Kapitaniak, Estimation of the dominant Lyapunov exponent of non-smooth systems on the basis of maps synchronization, *Chaos Solitons Fractals* 15 (2003) 233–244.